creative commons
COMMONS DEED

저작자표시-비영리-변경금지 2.0 대한민국

이용자는 아래의 조건을 따르는 경우에 한하여 자유롭게

- 이 저작물을 복제, 배포, 전송, 전시, 공연 및 방송할 수 있습니다.

다음과 같은 조건을 따라야 합니다:

저작자표시. 귀하는 원저작자를 표시하여야 합니다.

비영리. 귀하는 이 저작물을 영리 목적으로 이용할 수 없습니다.

변경금지. 귀하는 이 저작물을 개작, 변형 또는 가공할 수 없습니다.

- 귀하는, 이 저작물의 재이용이나 배포의 경우, 이 저작물에 적용된 이용허락조건을 명확하게 나타내어야 합니다.
- 저작권자로부터 별도의 허가를 받으면 이러한 조건들은 적용되지 않습니다.

저작권법에 따른 이용자의 권리는 위의 내용에 의하여 영향을 받지 않습니다.

이것은 이용허락규약(Legal Code)을 이해하기 쉽게 요약한 것입니다.

Disclaimer

dCollection

Ph.D. DISSERTATION

Characterizations of p-Type Tin Monoxide Thin Films Deposited by a Co-sputtering Process

by

Seung Jun Lee

February 2018

DEPARTMENT OF MATERIALS SCIENCE AND ENGINEERING

COLLEGE OF ENGINEERING

SEOUL NATIONAL UNIVERSITY

Characterizations of p-Type Tin Monoxide Thin Films Deposited by a Co-sputtering Process

Advisor : Prof. Cheol Seong Hwang

by

Seung Jun Lee

A thesis submitted to the Graduate Faculty of Seoul National University in partial fulfillment of the requirements for the Degree of Doctor of Philosophy

Department of Materials Science and Engineering

February 2018

Approved

by

Chairman of Advisory Committee : Hyeong Joon Kim

Vice-chairman of Advisory Committee : Cheol Seong Hwang

Advisory Committee : Seungwu Han

Advisory Committee : Jae Kyeong Jeong

Advisory Committee : Jeong Hwan Kim

Abstract

SnO thin films were prepared by co-sputtering deposition technique with SnO and Sn targets under different Sn target power ($P_{Sn\ DC}$). The growth films annealed at a low temperature of 180 °C in the air afterward. The properties of as-deposited and annealed films systematically studied using various techniques for their application to p-type thin film transistor. Grazing-angle incident X-ray diffraction (GIXRD) pattern analysis showed that the as-deposited films showed a metallic Sn phase, while the annealed films indicated SnO phase irrespective of $P_{Sn\ DC}$, which could be of p-type nature. The phase transition at annealed films observed at 40 W of $P_{Sn\ DC}$ from polycrystalline p-type SnO to a composite film containing both metallic Sn and p-type SnO phases with increasing the $P_{Sn\ DC}$. Field-emission scanning electron microscopy (FE-SEM) images showed the discernible ellipsoidal grains along the *c*-axis direction at the as-deposited film and the irregular protrusions with the tiny and indistinct hemispherical swellings at the surface of the annealed film with increasing the $P_{Sn\ DC}$. High-resolution transmission electron microscopy (HRTEM) images showed the metallic Sn phase at the as-deposited film, and the SnO phase in the protruded region and the metallic Sn phase in the uniform bulk region at the annealed film, which were a coincidence with the GIXRD results.

The SnO phase had tetragonal structure and the lattice parameters *a* and *c* were extracted from the GIXRD results of the annealed films. It found that the unit cell volume (a^2c) decreased with increasing the $P_{Sn\ DC}$. The SnO density and the Sn layer density of the films showed the increasing tendency with increasing the $P_{Sn\ DC}$. The residual stress tendency of the as-deposited films shows that the tensile to compressive stress characteristics change as the $P_{Sn\ DC}$ increases. The residual stress of the annealed films indicated all compressive properties irrespective of $P_{Sn\ DC}$ and its tendency was a similar trend of the lattice parameter *c* with increasing the $P_{Sn\ DC}$. X-ray photoelectron spectroscopy (XPS) results of the annealed films exhibited that the composition ratio of Sn atoms (Sn/O) increased with increasing the $P_{Sn\ DC}$, indicating the phases of changing from SnO to Sn-rich SnO.

Hall measurement results showed p-type semiconducting behavior at 0 W ≤ $P_{Sn\ DC}$ ≤ 40 W, but metallic behavior at 45 W ≤ $P_{Sn\ DC}$ ≤ 70 W which could be ascribed to the dominant role of metallic Sn. The maximum Hall mobility of 8.8 $cm^2/V{\cdot}s$ obtained at 40 W of $P_{Sn\ DC}$, which originated from the well-controlled amount of metallic Sn in SnO structure, leading the increasing Hall mobility. The Hall measurements at various annealing and measurement temperatures performed for two samples with specific $P_{Sn\ DC}$ conditions at 0 W representing the SnO phase as a reference and 40 W representing the Sn-rich SnO phase. The Sn-rich SnO sample showed the higher mobility, which indicated that the hole carrier conduction mechanisms and the microstructures of two samples could be different. This result is promising

for fabricating high-performance p-type oxide thin film transistor.

Keywords: p-type SnO, Sn-rich SnO, co-sputtering, SnO lattice parameters, Residual stress, Hall measurements

Student Number: 2013-30765

Seung Jun Lee

Table of Contents

List of Figures

List of Tables

List of Abbreviations

TFT	Thin film transistor
VBM	Valence band maximum
CBM	Conduction band minimum
RF	Radio frequency
DC	Direct current
$P_{Sn\ DC}$	Sn target DC power
$P_{SnO\ RF}$	SnO target RF power
MWA	Microwave annealing
GIXRD	Grazing-angle incident X-ray diffraction
FE-SEM	Field-emission scanning electron microscopy
HRTEM	High-resolution transmission electron microscopy
EDS	Energy dispersive spectroscopy
FFT	Fast-Fourier transformation
STEM	Scanning transmission electron microscopy
AFM	Atomic force microscopy
XRR	X-ray reflectivity
XRF	X-ray fluorescent spectroscopy
XPS	X-ray photoelectron spectroscopy
AES	Auger electron spectroscopy
V_{Sn}	Sn vacancy
O_i	O interstitial
Sn_i	Sn interstitial
V_O	O vacancy

1. Introduction

1.1. Overview

Up to now, the metal oxides as an exciting functional material have been researched widely both fundamental understanding and technological development for a new area of transparent and flexible electronics such as touch display panels, optical coatings, solid-state sensors, smart window, solar cells, active matrix (AM) flat panel displays [1-3]. The electrical properties of oxide materials exhibit the wide range of characteristics from insulating to semiconducting and conducting with high optical transparency in the visible light region. Therefore, the metal oxide materials have made an impressive progress, particularly in display applications as the active layers in thin film transistors (TFTs) in a relatively short time, challenging silicon not only in conventional applications but for the next generation of electronics. In general, most metal oxide materials such as zinc oxide (ZnO), indium gallium zinc oxide (IGZO), and indium zinc oxide (IZO) are typically exhibited n-type semiconducting behaviors which have been mainly demonstrates to show high electrical performance for TFTs with low temperature process, in comparison to the current industrial standard hydrogenated amorphous silicon (a-Si:H) TFTs [4-6].

Since the p-type oxide semiconductor materials with high enough reliability as well as electrical performances have not been reported yet, it has received

less attention than the well-studied n-type oxide semiconductor materials. However, many of the electronic applications in the modern era are limited by the lack of the availability of high-performance p-type oxide semiconductor along with the n-type ones, because it is required architectures such as p-n junctions and complementary metal oxide semiconductor (CMOS) types for more energy efficient devices [7]. Thereby, the research on the p-type oxide materials has been recognized to be very important and valuable by many researchers. To make p-type oxide semiconductors for better quality, the use of hybridized orbitals between O 2*p* and appropriate orbitals of neighboring metal cation have been proposed to obtain high hole mobility in a p-type oxide semiconductor [8]. The research of few oxide materials has been published and shows the possibilities for p-channel device applications. As a simple binary compound, there is a cuprous oxide (Cu_2O) [9, 10], tin monoxide (SnO) [11, 12], and nickel oxide (NiO) [13, 14] which have been used as an active layer of p-type oxide TFTs. Among few p-type oxide materials, SnO has received a great deal of attention because of Sn 5*s* nature at the valence band maximum (VBM). Generally, the VBM in oxides of typical materials is mainly composed of localized and anisotropic O 2*p* orbitals, which severely limits hole transport [15]. The spherical Sn 5*s* orbitals in SnO have nearly equal energy level with O 2*p* orbitals, and they hybridize and delocalize the O 2*p* orbitals which might result in a more effective hole transport path and expect

higher hole mobility [16]. Moreover, compared to those reported papers mentioned above, p-type SnO TFTs indicate relatively better electrical properties than other p-type oxide TFTs.

The p-type SnO has been fabricated using various deposition techniques including the conventional sputtering process. In addion, the deposition techniques are depending on different source types which can be broadly divided into four types as follows: (1) the radio frequency (RF), direct current (DC), and ion-beam reactive sputtering deposition techniques using pure Sn sources with O gas [17-19], (2) the RF magnetron sputtering, pulsed laser deposition, and vacuum thermal evaporation techniques using SnO sources [20-22], (3) the RF magnetron sputtering and electron-beam (E-beam) evaporation techniques using pure SnO_2 sources with reactive gas at a higher temperature for decomposition of SnO_2 to SnO phases [23, 24], and (4) the aqueous solution process and atomic layer deposition techniques using precursors including Sn [25, 26]. These fabricated p-type SnO films exhibit the similarities which indicate only polycrystalline structure and lower electrical properties than the n-type oxide semiconductor cases. Among them, the notable results can be found that Caraveo-Frescas *et al*. reported that the presence of small amounts of Sn in the p-type SnO matrix enhances the hole mobility which is a higher value than other reported values by the research groups above [18]. In addition, further increasing of Sn atoms causes carrier scattering and reduces the hole mobility in the p-

type SnO film, which means that the carefully controlled amount of additional metal Sn atoms in p-type SnO structure is an important factor.

In this article, we have prepared the p-type SnO thin films by a co-sputtering technique with pure SnO and Sn targets, and the characteristics of the co-sputtered SnO thin films were comprehensively investigated. Unlike the previously established experimental approach, to control the Sn amounts in the co-sputtered thin film as well as the obtaining p-type SnO phase, the different DC power of the metallic Sn target was applied while the RF power of the SnO target was fixed. Because it is anticipated that the co-sputtering method has an advantage to more sensitively and directly modulate the amount of Sn in the SnO structure than the other reactive deposition techniques under different oxygen or hydrogen partial pressures, substrate or annealing temperatures [18, 23, 27, 28]. Moreover, this Sn-rich condition by the co-sputtering process would be expected to prevent phase transformation from p-type SnO to n-type SnO_2. The aim of this study is to discuss how the properties of co-sputtered SnO thin films change, as close to the Sn-rich conditions. Emphasis was given to the effect of the presence of Sn amounts in the p-type SnO structure for the improved electrical property.

2. Literature

2.1. Oxide semiconductor for transparent display

Transparent electronics is today one of the most advanced topics for a wide range of device applications. Figure 2.1 shows a similar increase in the overall display market growth and the transparent display market growth [29]. It means that the future of transparent electronics seems very promising, since from the display market forecast by Displaybank, which can be seen the importance and marketability of transparent displays in Fig. 2.1. A driving force for enabling transparent electronic devices is the oxide semiconductor, which has the key components including wide bandgap and transparent properties. Table 2.1 represents a summary and comparison of some of the most important device properties for the different available technologies: oxide semiconductors, amorphous Si, low-temperature polycrystalline Si and organic semiconductors [30]. It shows that the oxide-based materials have excellent electrical characteristics compared to the conventional Si-based materials. Moreover, Figure 2.2 shows that the required mobility will be even higher for displays with higher resolution, a faster frame rate and a larger panel size [31]. For this reason, the researches on oxide semiconductors and TFTs have been inevitable in the display area. A study of these oxide TFTs is as follows. Figure 2.3 exhibits the evolution of publishes papers between 2001 and 2010 only related to n-type oxide-

based TFTs, and the bar chart is divided into three main categories function of the semiconductor channel layers [30]. It means that it is difficult to implement p-type oxide semiconductors relative to n-type semiconductors. Therefore, it is necessary to examine the characteristics of the respective n-type and p-type oxide semiconductors to find the reasons above.

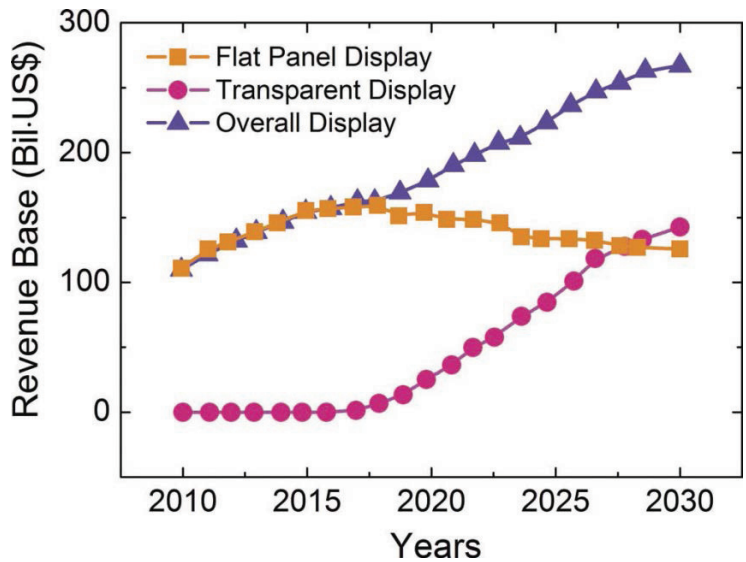

Figure 2.1. Transparent display technology evolution and global display market [29].

Table 2.1. Comparison between oxide semiconductor TFTs and the other available technologies [30].

TFT properties	**Oxide semiconductors**	**Amorphous Si**	**Low-T poly-Si**	**Organic semiconductors**
Carrier mobility [$cm^2 V^{-1}S^{-1}$]	1 to 100	1 max	50 to 100	0.1 - 10
Switching [V $dec.^{-1}$]	0.1 to 0.6	0.4 to 0.6	0.2 to 0.3	0.1 - 1.0
Leakage current [A]	10^{-13}	~ 10^{-12}	~ 10^{-12}	~ 10^{-12}
Manufacturing cost	Low	Low	High	Low
Long term TFT reliability	High (forecast)	Low	High	Low in air
Yield	High	High	Medium	High
Process temp. [℃]	RT to 350	~ 250	< 500	RT

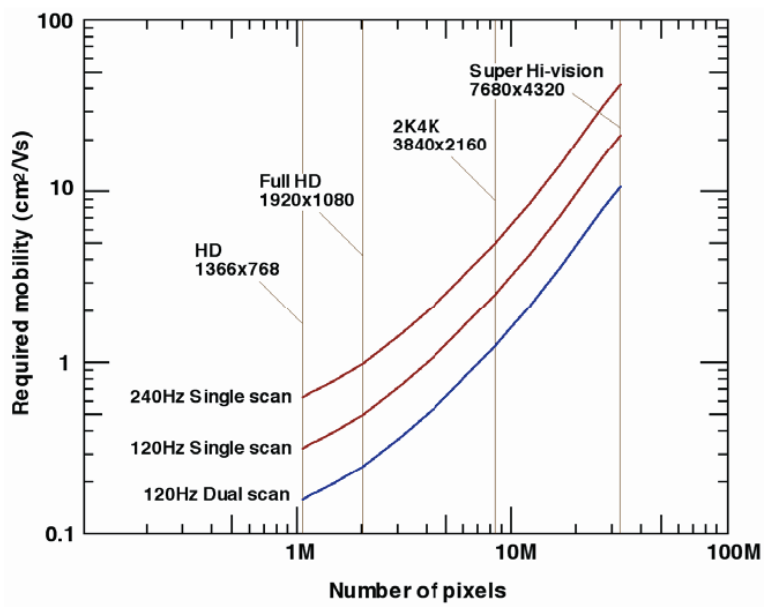

Figure 2.2. Graphical summary of required carrier mobility for future displays [31].

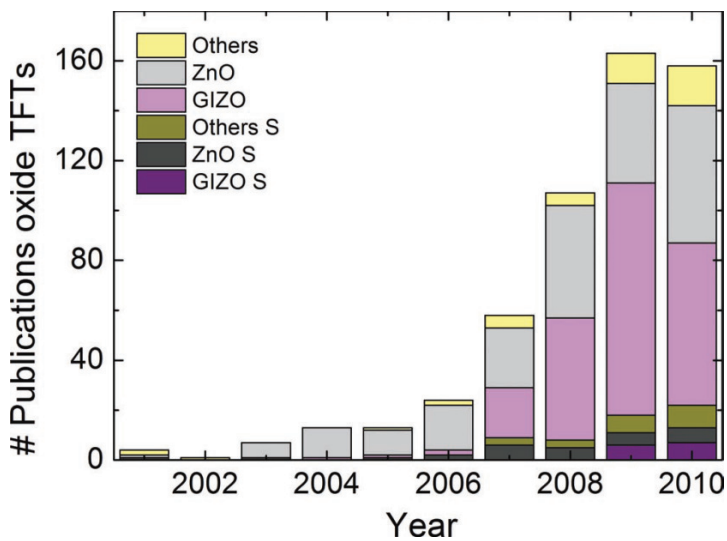

Figure 2.3. A number of oxide TFTs related papers published per year. In the legend S means “solution processed” only dealing with GIZO TFTs [30].

First, in the case of n-type oxide semiconductors, Figure 2.4(a) shows the schematic energy diagrams of n-type oxide semiconductors. Most of the conduction band minimums (CBMs) are composed of isotropic metal cation *s* orbital, which is totally overlapping compared to the Si case as shown in Fig. 2.5 [5]. In addition, since the effective mass of electrons is small, it can be expected that it contributed to better mobility. Due to this isotropic shape, the bonding angle between metal cation and oxygen anion can be broadened to form a unique electron transport path. Therefore, it is possible to obtain excellent carrier transfer even in the amorphous state, and a typical example is an a-IGZO material in Fig. 2.5, which had firstly reported by the Hosono group. On the contrary, in the case of the p-type oxide semiconductor, most of the VBMs are composed of 2*p* orbital of anisotropic oxygen anion, which localized as shown in Fig. 2.4(b). In addition, the effective mass of holes is large, and most oxide semiconductor materials require large energy for hole products and require low energy for hole killers [15, 32_bipolar]. For this reason, it is difficult to form p-type oxide semiconductors, and even if fabricated, it shows the low hole concentration and low hole mobility. In order to solve this problem, many researchers have been investigated to form a hybridized orbital between the oxygen 2*p* and metal cation orbitals which are appropriately overlapped for obtaining p-type characteristics and improve performance.

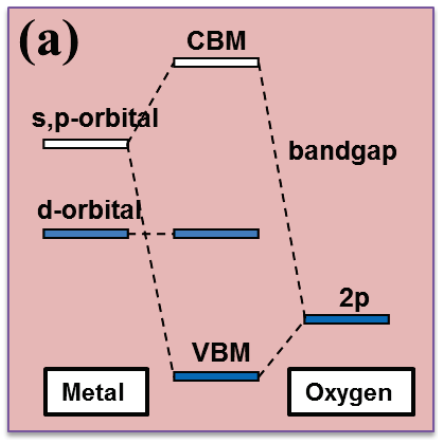

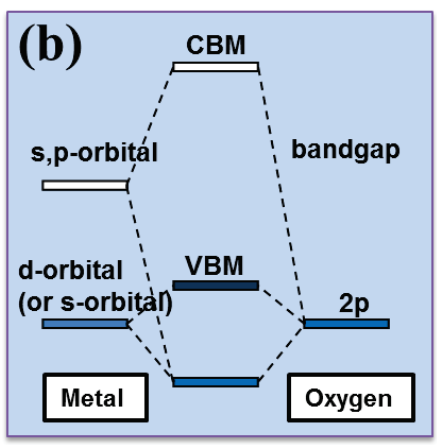

Figure 2.4. Schematic energy diagrams of (a) n-type and (b) p-type oxide semiconductors.

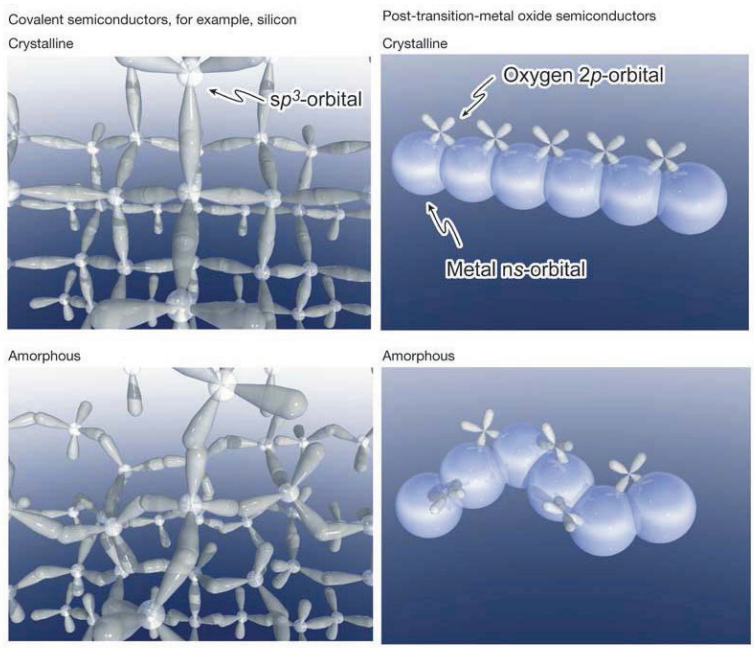

Figure 2.5. Schematic orbital structure of the conduction-band minimum in Si and in an ionic oxide semiconductor [5].

2.2. p-Type candidate oxide materials

The proposed hybridized orbital methods for the implementation of p-type oxide semiconductors already have been studied through the combination using several materials as follows. Some authors proposed that the use of hybridized orbitals between O 2*p* and Cu 3*d* produces a p-type oxide semiconductor and discovered p-type transparent oxide semiconductors, in which the schematic energy diagram and atomic structure of Cu_2O were illustrated in Fig. 2.6 [33]. Similar electronic structures are also found in Ag_2O [34]. Although both materials exhibit p-type characteristics, Cu_2O TFTs are not well operated due to low switching behavior, and Ag_2O shows the metallic conduction properties due to a high carrier concentration of the film, which is not applicable to a channel of a TFT. Another approach is to employ pseudo-closed ns^2 orbitals to form such hybridized orbitals. There are PbO [35], BiCu*Ch* (*Ch* = S, Se, Te) [36], and SnO [37]. Such electronic structures are found in oxides of heavy metal cations, such as Pb^{2+} ($6s^2$), Bi^{3+} ($6s^2$), and Sn^{2+} ($5s^2$) because these are stable in ns^2 ($n \leq 5$) pseudo-closed shell electronic configurations in these crystals [15, 16]. PbO is reported to be an n-type semiconductor, while the Bi 6*s* orbitals are very deep compared to the VBMs even if it is a p-type semiconductor. Finally, SnO is considered to be the most likely candidate for p-type oxide semiconductors due to its Sn 5*s* nature at the VBM, which was illustrated the energy diagram as shown in Fig. 2.7 [37]. In other words, it is possible to form a hybridized orbital with

localized anisotropic O 2*p* and isotropic 5*s* orbitals [7, 15]. It is also simple oxide which can be lead to more effective hole transport path and relatively higher hole mobility due to the overlapping portion [16, 20]. This is a very similar part of the carrier transport mechanism of the a-IGZO material, which can be expected to work on amorphous SnO TFTs.

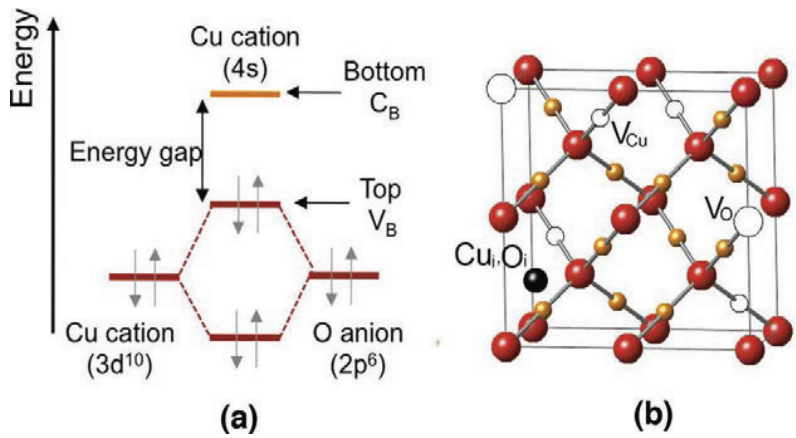

Figure 2.6. (a) The chemical bond between an oxide ion and a cation that has a closed-shell electronic configuration, and (b) representation of the more important defects in Cu_2O [33].

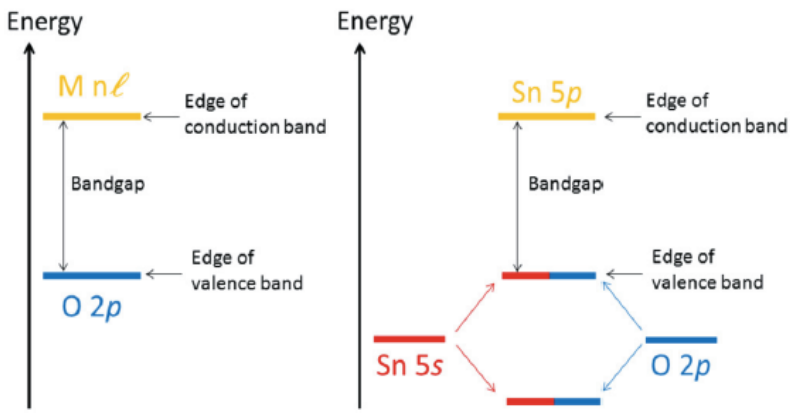

Figure 2.7. Schematic diagram of the energy levels for a typical metal oxide (left) and for SnO (right). For the typical metal oxide, the VB is dominated by the O 2*p* orbitals and the CB by the cation states (e.g., Sn 5*s* for SnO_2). For SnO, the energy proximity of the Sn 5*s* and O 2*p* states results in equal contributions to the VB edge [37].

The p-type conductivity characteristics of SnO are as follows. Togo *et al*. reported the demonstration of tin oxide based on the first-principle calculation which is summarized as follows: (1) The V_{Sn} (Sn vacancy) and O_i (O interstitial) act as acceptor-like defects for p-type conductivity under O-rich conditions, while Sn_i (Sn interstitial) and V_O (O vacancy) act as donor-like defects for n-type conductivity under Sn-rich conditions. (2) The origin of p-type conductivity in SnO is mainly attributed to V_{Sn} and O_i, that when fully ionized. (3) The O_i is hardly ionized and so it can not expect to contribute to the generation of holes. (4) The V_{Sn} is the dominant defect served as a source of hole carriers for the p-type conductivity [38_Togo]. Moreover, the demonstration of tin oxide based on the first-principle calculation that Sn 5*s* and O 2*p* are mainly composed near VBM as shown in Fig. 2.8. Due to the hybridized orbitals, the Sn 5*s* orbital could further reduce the localization by O 2*p* orbital, which could be expected to improve hole mobility. As mentioned above, the p-type conductivity of SnO is explained by the V_{Sn}, which can be more easily understood from the E. Fortunato group. The quasi-chemical stoichiometric reaction of SnO is as follows [39_Fortunato]: (1) $SnO \leftrightarrow Sn^{2+} + 2V_{sn}^{-} + ½O_2$, or (2) $SnO \leftrightarrow Sn^{2+} + V_{sn}^{2-} + ½O_2$, or (3) $SnO \leftrightarrow Sn^{2+} + V_{sn}^{-} + O_i^{2-} + ½O_2 + V_o^{+}$, giving rise to the formation of two holes, without or with the formation of an ionized V_O, and the ionized O_i is relatively not well formed. From these chemical reactions and the first principle calculations of SnO, it defines that the p-type

conductivity of SnO is due to V_{Sn}.

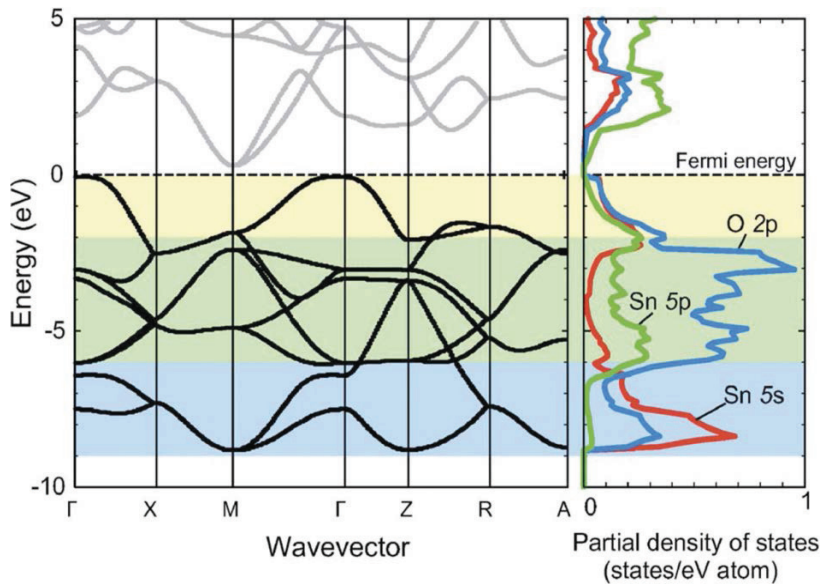

Figure 2.8. Band structure left and projected density of states (PDOS) right of the unit cell of the SnO perfect crystal. The energy of the highest occupied band at the Γ point is set to 0 eV. The highest occupied state is located between the Γ and *M* points. The lowest unoccupied state is given at the *M* point. The background of the band structure and PDOS figures denotes three characteristic energy regions in the valence band [38].

2.3. Metastable p-type SnO

According to the Sn-O phase diagram at atmospheric pressure, the most common oxides of Sn are p-type SnO and n-type SnO_2 at RT [40_Batzil] as shown in Fig. 2.9. Among them, the p-type SnO is known as the thermodynamically unstable structure at ambient conditions which can be easily converted into stable n-type SnO_2 by mechanical pressure at high or thermal treatment at moderate temperature [32_Bipolar, 41_Giefers, 42_W. H. Doh]. As p-type SnO is a metastable phase, it is likely to either be reduced to a zero valence state (metallic Sn) or be oxidized to a higher valence state (n-type SnO_2), even in the absence of external oxygen [7_Z. Wang]. Moreover, it found that the deposited film often shows multi-phases including metallic Sn and/or SnO_2, rather than pure SnO [43_J. Zhang]. Consequently, for obtaining the p-type conductivity of SnO, which can only be existed in a narrow window of grown conditions, the thermodynamic conditions such as oxygen partial pressures and applied temperatures should be very sensitively controlled [20_Yabuta]. Some of the facts are partially consistent with our experimental results that both the p-type pure SnO and multi-phase SnO with metallic Sn are not only obtained under specific process conditions such as very lower deposition pressure and limited temperatures for annealing but also can be intendedly fabricated by controlling the sputtering power.

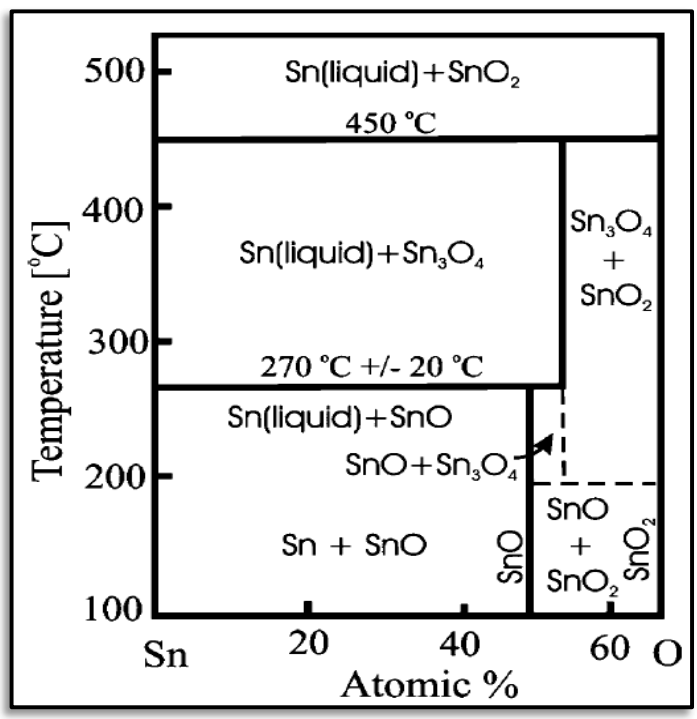

Figure 2.9. The Sn-O phase diagram.

The phase transformation from p-type SnO to n-type SnO_2 is dependent on many factors such as the film preparation method and conditions, the post thermal treatment method, atmosphere, duration, and temperature, respectively [44_Liang_optical]. Among them, the theoretical and experimental studies have intensively focused on the temperature effect on the phase transformation by various research groups [41_Giefers, 45_Geurts, 46_Moreno_1992, 47_Pei]. Generally, the phase transformation conditions, except for the doping effects, can be categorized as (1) oxidation and (2) decomposition reaction, which are classified by whether the temperature is high or low. First, SnO is known to be oxidized into SnO_2 when annealed at around 300 °C in the air by an internal displacement of O, followed by an incorporation of external O [44_Liang_optical, 48_Allen_2011]. The first oxidation effects were observed after heating at 200 °C and total conversion to SnO_2 was achieve at 650 °C [45_Geurts]. Second, SnO can be decomposed to SnO_2 with the expulsion of Sn atoms at high processing temperature even in the absence of oxygen [41_Giefers, 57_Pei]. It is also called the disproportionation reaction. M. S. Moreno *et al*. reported that the disproportionation reaction begins slowly at temperatures above 300 °C and displays its fastest rate between 400 and 500 °C, which the disproportionation reaction seems to be faster than the oxidation reaction [46_Moreno_1992, 49_Moreno_2001]. This result mentioned above can be visualized as a diagram in Fig. 2.10. Figure 2.10 shows the schematic

diagram of phase transformation from SnO to SnO_2 via the oxidation and the disproportionation reaction. The curve indicates the Gibbs free energy. All information in Fig. 2.10, which is theoretically and experimentally obtained by other research groups mentioned above, is graphically organized [49_Moreno_2001, 50_A. G. Sabnis, 51_M. Kanayama].

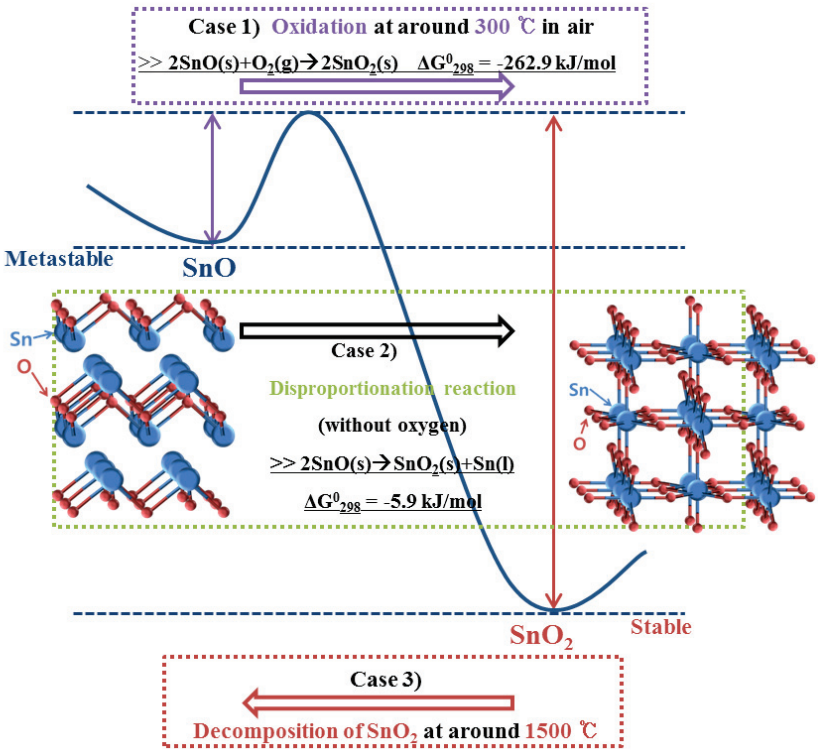

Figure 2.10. The schematic diagram of phase transformation from SnO to SnO_2 via the oxidation and the disproportionation reaction. The curve indicates the Gibbs free energy.

2.4. Research trend of p-type SnO

Research on the trend of SnO as a simple binary material and its TFTs has been studying until 2008, starting with SnO TFT fabricated by pulsed laser deposition (PLD) method in 2008 by H. Hosono Group. However, except for the result published by H. N. Alshareef group in 2013, it can be seen that the electrical characteristics of the TFTs are considerably lower than those of the n-type TFTs. Moreover, in the case of SnO TFTs, all of them showed characteristics only in polycrystalline phase, and these results are still lacking compared to n-type oxide materials. The research trend of p-type SnO is summarized in Table 2.2.

Table 2.2. The research trend of p-type SnO.

Recent studies (SCI) of p-type SnO thin film fabrication							
Year	**Deposition method**	**Target (source, solution)**	**Substrate**	**Temp._subs. (℃)**	**Post-annealing (℃, ambient, time)**	**Features (gas etc.)**	**Reference (Red: TFTs)**
2008	reactive evaporation	pure Sn (powder)	SiO_2/Si	100	100, air, 1hr	p-type SnO_2 / inverter	Appl. Phys. Lett. 92, 122113-1
	reactive evaporation	pure Sn (powder)	SiO_2/Si	100	100, air, 1hr	p-type SnO_2 / inverter with In_2O_3	Appl. Phys. Lett. 92, 232103
	PLD	(single-phase) SnO	(001) YSZ	575	200, vacuum, 5min for TFT	epitaxial / RTA	Appl. Phys. Lett. 93, 032113
2009	PLD	(single-phase) SnO	(001) YSZ	575	200, vacuum, 5min for TFT	epitaxial / RTA	Phys. Status Solidi A 206(9), 2187
2010	E-beam evaporation	(high purity) SnO_2 ceramic	SiO_2/Si, Al_2O_3	RT, 350, 600	-	SnO_2 with Y_2O_3 or Sb_2O_3	Appl. Phys. Lett. 96, 042113-1
	Vacuum Thermal Evaporation	SnO powder	Eagle XG glass, SiO_2/Si	RT	300	Air stability with Resistance of SnO	Jap. J. Appl. Phys. 49, 2010
	VTD (vapor transport process)	Sn (metal pallets, 4N)	Si	230	-	branched nanostructure / single crystalline	Mater. Lett. 64, 1120
	E-beam evaporation	(high purity) SnO_2	SiO_2/Si, quartz	RT	300-500, Ar, 10min / 600, vacuum, 30min	RTA in Ar /	J. Electrochem. Soc. 157(6), H598
	E-beam evaporation	(high purity) SnO_2	quartz	250	600, vacuum, 30min	SnO_x	ACS Appl. Mater. Interf. 2(6), 1060
	RF reactive sputtering	Sn	glass	RT	200, air	SnOx (x<2)	Appl. Phys. Lett. 97, 052105
	RF magnetron sputtering	SnO	SiO_2/Si	RT	300, 400, N_2, O_2, air, 2hr	SiO_x capping layer effect	Appl. Phys. Lett. 97, 072111-1

2011	PLD	(single-phase) SnO	(001) YSZ	550	-	Sb(<10%) + SnO powder / bipolar conduction	ECS Solid State Lett. 14(1), H13
	RF magnetron sputtering	SnO (3N target, powder)	quartz	60-220	-	I(101)/I(110) relation	Appl. Phys. Express, 4(7), 071101
	PLD	SnO	SiO_2/Si	RT	250, air, 30min for TFT	ambipolar / Dual Gate TFT	Adv. Mater. 23, 3431
	RF reactive magnetron sputtering	5N Sn target	borosilicate	100	-	O_2 / N_2 doped SnO	Curr. Appl. Phys. 11, S139
	solution process	$SnCl_2 \cdot 2H_2O$, NaOH	-	RT	-	sub-mm-sized singe crystal	Cryst. Eng. Comm. 13, 5677
2012	RF reactive magnetron sputtering	5N Sn target	borosilicate	300	-	O_2 / N_2 doped SnO	ECS Solid State Lett. 1(2), P29
	solution process	$SnCl_2 \cdot 2H_2O$, NH_4OH	glass, SiO_2/Si	RT	200-600, N_2(92%)+H_2(8%), 2hr	-	J. Mater. Chem. 22, 4607
	E-beam evaporation	(well sintered) SnO_2	SiO_2/Si	RT	400, Ar, 10min	RTA / ambipolar / inverter	Appl. Phys. Lett. 100, 263502
	E-beam evaporation	(well sintered) SnO_2	SiO_2/Si	RT	350, vacuum, 3hr	Y-doped SnO	J. Phys. D: Appl. Phys. 45, 085101
	RF reactive magnetron sputtering	high purity 4N SnO_2	c-plane Al_2O_3	600	-	Phase seperation	JACS, 95 [1], 324
	RF reactive magnetron sputtering	4N Sn target	quartz	RT	200, air, 2hr	SnO_x / O_2 / conductivity dilemma area	ACS Appl. Mater. Interf. 4, 5673
	E-beam evaporation	SnO_2	SiO_2/Si	RT	400, Ar	-	-
	solution process	$SnCl_2 \cdot 2H_2O$, NaOH, PVP*	-	90	-	SnO nanosheets	Langmuir 28, 10597
	RF magnetron sputtering	5N Sn target	borosilicate	300	400, Ar, 1hr	O_2 / N_2 doped SnO	Mater. Sci. Eng. B 177, 1470
2013	RF reactive magnetron sputtering	5N Sn target	glass	RT	100-400, vacuum, 3hr	SnO+ZnO p-n hetero-junction	Mater. Sci. Eng. B, 178, 816
	DC reactive sputtering	Sn	polyimide / glass	RT	180, air, 30min	Record mobility / phase engineeging	ACS Nano, 7(6), 5160
	RF magnetron sputtering	3N SnO ceramic target	E2K glass / SiO_2/Si for TFT	RT	200-400, vacuum, 1hr	effect of Ti, Ni and Mo S/D electrodes for TFT	Jpn. J. Appl. Phys. 52, 05DC07
	RF reactive magnetron sputtering	5N Sn target	borosilicate	100	-	O2 / N_2 doped SnO / Effect of RF power	Mater. Sci. Semi. Proc., 16, 1679

2014	RF magnetron sputtering	Sn/SnO_2 mixed target	E2K glass / SiO_2/Si	RT	500, N_2 or vacuum, 1hr	Sn/SnO_2 mixed target	Thin Solid Films 555, 57
	RF magnetron sputtering	3N SnO target	quartz	60-220	-	T_{sub} effect, optical analysis	Thin Solid Films 555, 148
	RF reactive magnetron sputtering	(~5N) Sn ??	eagle 2000 glass	RT	250, air, 1hr	(positive)Gate-bias stress stability	IEEE EDL 35(1), 90
	RF reactive magnetron sputtering	Sn target	SiO_2/Si	90	230, air, 1hr	-	Semicond. Sci. Technol. 29, 045001
	RF magnetron sputtering	4N SnO_2 target	E2K glass	RT	300, vacuum, 1hr	RTA / H_2 doped SnO / phase engineeging	ACS Appl. Mater. Interf. 6, 13724
	PLD	3N SnO ceramic target	Silica-glass	275-500	300-500, vacuum, 1hr	epitaxial / In-situ, ex-situ annealing	ECS J. Solid State Sci. and Technol. 3(9), Q3040
	DC reactive sputtering	Sn	glass	RT	RT	Electroforming-free RRAM	Appl. Phys. Lett. 104, 152104
			Al_2O_3/ Si		210, air, 30min	CMOS using single step deposition with SnO	Scientific reports 4: 4672
			polyimide / glass		200, air, 30min	Polymer ferroelectric field-effect memory with record hole mobility	Scientific reports 4: 5243
	RF reactive magnetron sputtering	5N Sn target	ITO glass / borosilicate	100	300, N_2, 1hr	Homo-junction with p-SnO and n-SnO_2	ECS Solid State Lett. 3(8), P94
	Vacuum Thermal Evaporation	SnO powder	Eagle XG glass, SiO_2/Si	RT	300	p-channel amorphous SnO TFTs	J. Disp. Tech. 10(4)
	RF reactive magnetron sputtering	(~5N) Sn ??	Eagle XG glass	RT	225, air, 30min	CMOS with n-ZnO and p-SnO TFTs	IEEE EDL 35(12), 1263
	RF reactive magnetron sputtering	Sn target	SiO_2/Si	RT	200, vacuum, 100s	Long-Term Durabiility and Bias Stress Stability, using a Su-8 passivation layer	IEEE EDL 35(12), 1260
	RF reactive magnetron sputtering	4N Sn target	SiO_2/Si	RT	200, air, 1hr	ambipolar / conductivity dilemma area	ECS J. Solid State Sci. and Technol. 3(9), Q3091
	DC reactive sputtering	4N Sn target	glass	RT	160, air, 30min	SnO nanowire pattern with E beam lithography (the best mobility obtained)	Appl. Phys. Lett. 103, 222103
	ALD	$Sn(dmamp)_2$ precursor (Patent) and H_2O	SiO_2/Si	90-210	-	the 1st ALD p-type SnO	Chem. Mater. 26, 6088

2015	RF magnetron sputtering	SnO_2:Sb(5at.%) target	SiO_2/Si	RT, 100-400	-	p-SnO: semiconductor / n-SnO_2: conductor	Mater. Lett. 139, 39
	DC reactive sputtering	Sn target	glass	RT	200, air, 30min	Hybrid dual gate ferroelctric memory	Org. Elec., 16, 9
	E-beam evaporation	(high purity) SnO_2	glass, SiO_2/Si, quartz	RT	400, Ar, 10min	Effect of Al_2O_3 capping layer and their Thichness	J. Mater. Chem. C
	RF reactive magnetron sputtering	Sn target	SiO_2/Si	RT	250, vacuum, 100s	Environment-dependent bias stress stability	IEEE EDL 36(5), 466
	PLD	(high purity) Sn target	(001) YSZ	200	-	Selective fabrication n-, p-type SnO without doping	Phys. Syayus. Solidi. RRL, 1-5, 201510016
	Reactive (RF) ion-beam sputtering	(3") Sn target	c-plane sapphire	100-600	-	SnO_{2-x} in the entire compositon range (x = 0 to 1) & Raman	Phys. Syayus. Solidi. RRL, 1-5, 201510058
	RF reactive magnetron sputtering	Sn/SnO_2 mixed target	Hf_2O/SiO_2/Si // SiO_2/Si	RT	300, vacuum, 1hr	p-type SnO TFT using Sn/SnO_2 mixed target with Ar and H_2 gas	Thin Solid Films 585, 50
	DC reactive sputtering	4N Sn target	SiO_2/Si	RT	(200, air, 30min) = ?	Resistive Switching Memory comprising p-type SnO bilayers	Adv. Electron. Mater. 1, 1400035
	RF reactive magnetron sputtering	~5N Sn target	Eagle XG glass	RT	225 - 265, air, RTA	Effect of RTA temperatures of SnO_x	Appl. Surf. Scie. 327, 358

3. Characterizations p-Type Tin Monoxide Thin Films Deposited by Co-sputtering

3.1. Experimental

A heavily doped p-type silicon (p^{++} Si) wafer was used as the substrate. P-type SnO thin films by co-sputtering technique with a pure SnO (SnO; 99.99 %, 3 inch diameter, Toshima) and a metallic tin (Sn) targets (99.99 %, 4 inch diameter, Thifine) were prepared on the substrate by conventional RF magnetron and DC magnetron sputtering systems, under a working pressure of about 1.5×10^{-3} Torr (0.2 Pa). The sputtering was done at room temperature (RT) in only pure argon (Ar) gas used at 20 sccm. Before deposition, the main chamber was evacuated to a background pressure of 1.0×10^{-7} Torr (1.3×10^{-5} Pa). To control the Sn amount, DC powers of the Sn target ($P_{Sn\ DC}$) varied from 0 to 70 W while the RF power of the SnO target ($P_{SnO\ RF}$) was fixed at 80 W. The deposition rates were ranged from 0.73 to 2.63 Å/s. Co-sputtered SnO thin films were then post-annealed at 180 °C in air for 25 min using a microwave annealing (MWA, 2.45 GHz) equipment to crystallize the SnO film layers (SUX-02, Unicera). Figures 3.1 show the schematic diagrams of the co-sputtering system and microwave annealing chamber, respectively. The thickness of all SnO thin films in this work was kept at an approximate value of 30 nm.

The crystal structures and crystallinity of the films were investigated using

grazing-angle incident X-ray diffraction (GIXRD, PANalytical X'pert Pro) with an incidence angle of 0.5° using Cu K_α X-ray radiation. The surface morphology of the films was imaged by field-emission scanning electron microscopy (FE-SEM, SU9000, Hitachi). Cross-sectional images of the film were acquired using high-resolution transmission electron microscopy (HRTEM, JEM-2100F, JEOL). The TEM samples were fabricated by mechanical grinding down to ~1 μm thickness and final thinning by mild ion milling, which involves minimal adverse effect from the sample fabrication process. The film morphologies were examined by the atomic force mic roscopy (AFM, JEOL, JSPM-5200). The film thickness, deposition rate, and film density were evaluated by means of X-ray reflectivity (XRR, X'pert Pro, PANalytical) measurements. X-ray fluorescent spectroscopy (XRF, Quant'X, Thermo SCIENTIFIC) was used to estimate the layer density of SnO films which show the metallic Sn content in this film. The Si substrate curvature was monitored with a Multi-beam optical sensor (MOS) wafer curvature system (kSA-MOS, K-Space Associates, Inc.) to obtain the physical properties of the films by measuring the residual stress. To investigate the chemical binding state of the annealed films, X-ray photoelectron spectroscopy (XPS, AXIS-HSi, KRATOS) was employed using monochromatic Al K_α source. The depth profiling of the films was carried out using Auger electron spectroscopy (AES, PHI-700, ULVAC-PHI). Carrier concentration, Hall mobility, and resistivity were extracted from Hall

measurements (HMS-3000, Ecopia) in a Greek-cross patterned, 100 nm thick, co-sputtered SnO thin films on the silica glass (Eagle XG) substrate, and were obtained at RT in a magnetic field of 5500 G with the Van der Pauw configuration. A 60 nm sputtered Au electrode was used for the Hall measurements.

Most of the films were deposited on p-type Si wafer with a thickness of 600 μm, which has a native oxide (~1 nm thickness), except for the films for the electrical measurements and stress measurements. For the stress measurement using the wafer curvature method, the thinner Si wafer (100 μm thickness) and thicker films (100 nm thickness) were necessary to induce sufficient curvature to measure. To completely exclude the possible contribution from the Si substrate during the measurements of the electrical properties, 100nm-thick films were grown on silica glass under the identical conditions. The stress levels of the films grown on the silica glass could not be measured due to the too small curvature of the samples (owing to the high thickness (700 μm) and stiffness of the Eagle XG glass), but the similar structural analysis results of the films indicated that the different types of substrate did not critically influence the growth characteristics and phase-evolution during the post-deposition annealing. The thicker films (100 nm) were necessary because the 30nm-thick films showed too high resistivity to acquire reliable Hall coefficients.

The bottom-gate and top contact type SnO TFTs fabrication were

performed by a conventional photolithography technique, where a p^{++} Si wafer was used as a substrate and a gate electrode. A 35-nm thick thermally grown SiO_2 was employed as a gate insulator, and a 13.5 nm-thick SnO thin film was deposited onto the SiO_2/Si substrate by the co-sputtering method. SnO active channel area was isolated by a wet chemical etch in diluted hydrofluoric (HF) solution, and then, 60 nm-thick sputtered Au source and drain (S/D) electrodes were defined by a lift-off process. The channel length and width of the device were 5 μm and 20 μm, respectively. The fabricated TFTs were subjected to post-annealing at 160 °C in air ambient for 25 min, using a MWA equipment to improve contact properties between a SnO channel and S/D electrodes. The electrical properties were measured using a semiconductor parameter analyzer (HP4155A, Hewlett-Packard) at room temperature in a dark box.

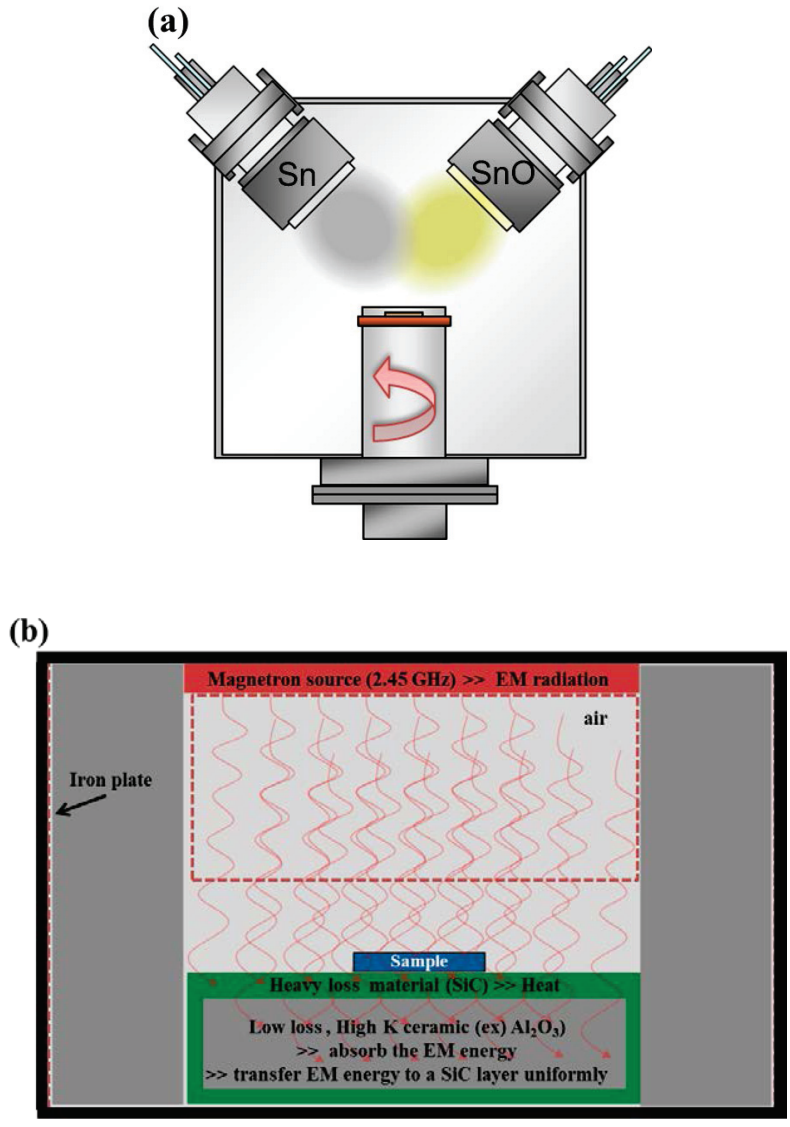

Figure 3.1. The schematic diagrams of (a) co-sputtering with SnO and Sn targets and (b) microwave annealing equipment.

3.2. Structural properties

Figure 3.2(a) illustrates the GIXRD patterns of the 30 nm-thick as-deposited thin films by co-sputtering in the $P_{Sn\ DC}$ range from 0 to 70 W at a deposition pressure of 1.5 mTorr. The scanning range (2θ) is between 10° and 70°. In case of $P_{Sn\ DC}$ = 0 W means that the single SnO RF magnetron sputtering was adapted at fixed 80 W without any Sn DC power applied. Between 0 and 10 W of $P_{Sn\ DC}$ ranges, no diffraction peaks appeared as a nano-crystalline or amorphous structure. As increasing the $P_{Sn\ DC}$ up to 70 W, diffraction peaks observed and these intensities were gradually increased. The GIXRD patterns of as-deposited films indicated all metallic Sn diffraction peaks, irrespective of $P_{Sn\ DC}$ ranging from 20 to 70 W. These diffraction peaks could be assigned to the (200) at 2θ of 30.6°, (101) at 32°, (220) at 43.9°, (211) at 44.9°, and (301) at 55.3° planes of the metallic Sn phases (JCPDS card no.04-0673). This result showed that the sputtered Sn atoms from the two targets are a dominant factor in the deposited films.

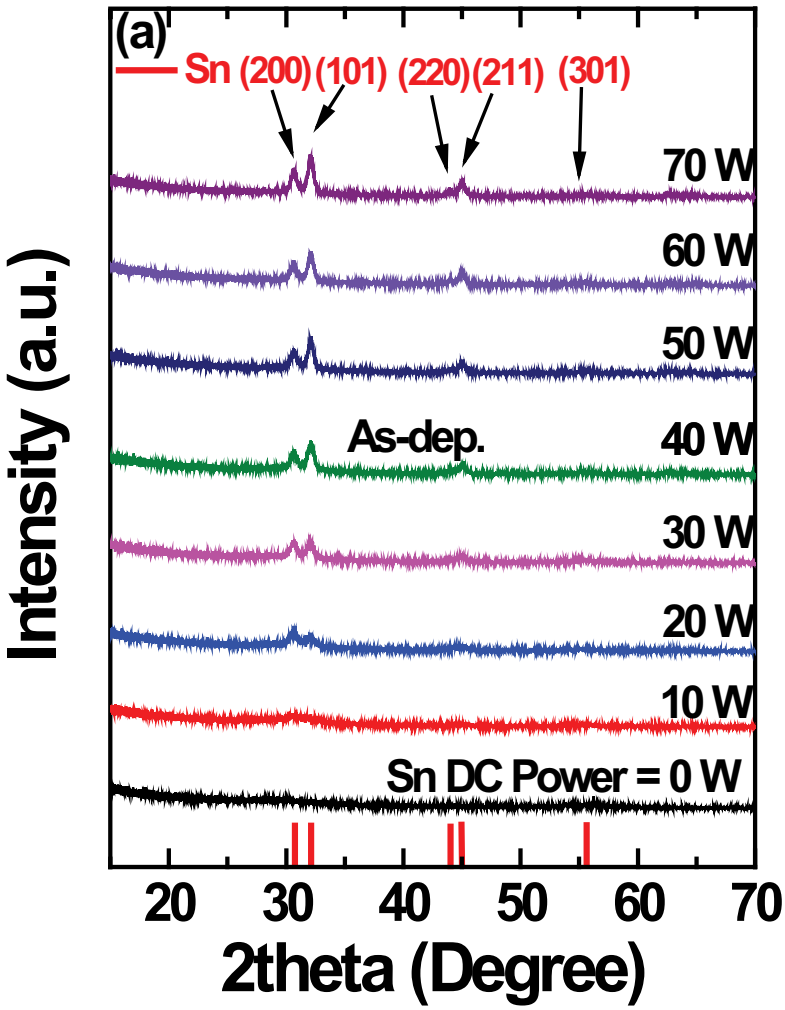

Figure 3.2. (a) GIXRD patterns showing phase formation of 30 nm-thick as-deposited thin films dependence on the $P_{Sn\ DC}$ with the fixed $P_{SnO\ RF}$ at 80 W at a deposition pressure of 1.5 mTorr.

Figure 3.2(b) illustrates the GIXRD patterns of the films annealed at 180 °C. It revealed that all GIXRD pattern results were polycrystalline p-type SnO structure, except for extra peaks at the red-colored A and B points in the $P_{Sn\ DC}$ ranging from 30 to 70 W. It also indicated that the intensity of the diffraction peaks was markedly affected by the $P_{Sn\ DC}$. From the Fig. 3.2(a) and (b) results, the p-type SnO phase could only be obtained through the annealing process. The randomly oriented two-sharp peaks at 2θ of 29.8° and at 33.3°, and four small broad peaks at 47.8°, at 50.8°, at 57.4°, and at 62.1° could be attributed to the (101), (110), (200), (112), (211), and (202) phases of SnO, respectively (JCPDS card no.06-0395). These peak-broadenings are owing to the poor crystallinity. Moreover, we can see that the intensity of (110) at 2θ of 29.8° diffraction peak increased and the intensity of (101) at 33.3° diffraction peak inversely decreased, and the 2θ positions of the two main sharp peaks were slightly shifted with increasing the $P_{Sn\ DC}$. This can be deduced from the fact that the changes of physical properties in the annealed films occurred depending on the $P_{Sn\ DC}$.

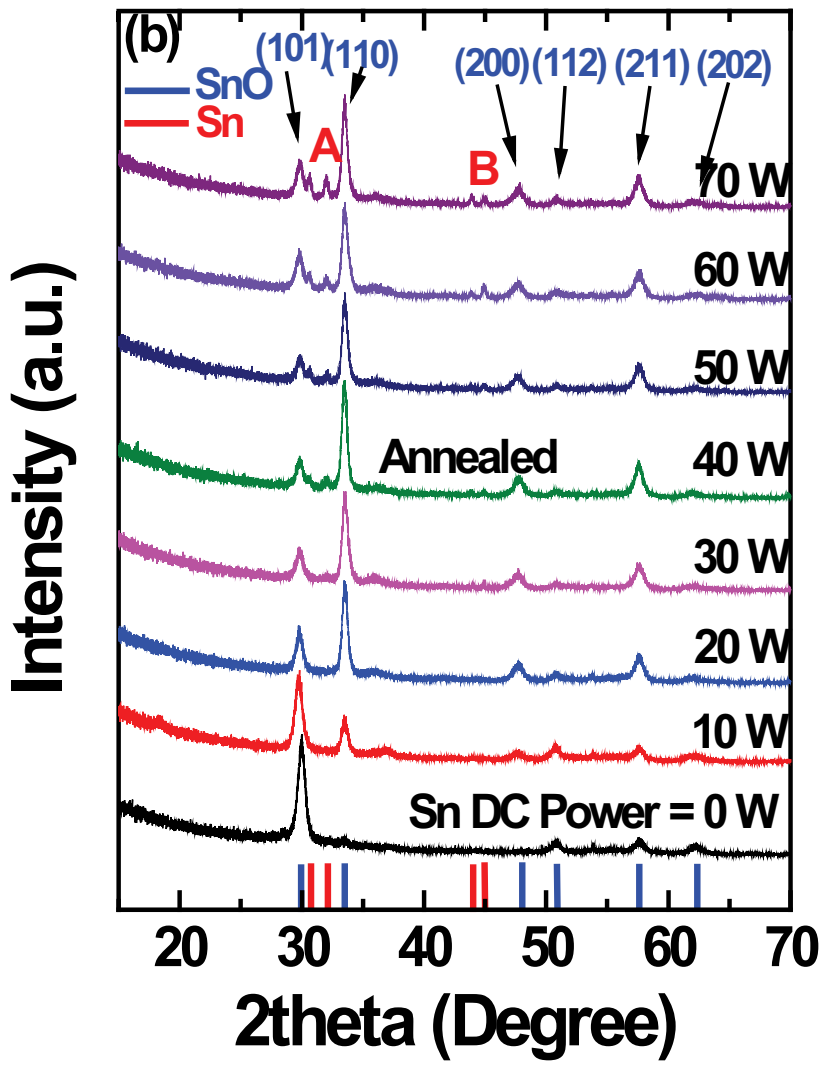

Figure 3.2. (b) GIXRD patterns showing phase formation of 30 nm-thick annealed films at 180 °C dependence on the $P_{Sn\ DC}$ with the fixed $P_{SnO\ RF}$ at 80 W at a deposition pressure of 1.5 mTorr.

The GIXRD patterns of the co-sputtered thin films at 40 W ≤ $P_{Sn\ DC}$ ≤ 70 W showed each two-weak peaks at the red-colored A and B point at the scanning range 30.2° ≤ 2θ ≤ 32.7° and 43° ≤ 2θ ≤ 46° in Fig. 3.2(b). Figure 3.2(c) is the zoom at the A, B points in a narrower 2θ range to clarify how the diffraction intensity increases as a function of $P_{Sn\ DC}$. These weak diffraction peaks indicate the presence of metallic Sn in the SnO phase that could be assigned to the (200), (101), (220), and (211) planes of metallic Sn, respectively. As indicated in Fig. 3.2(b), the GIXRD patterns showed the dependence of phase formation on the different $P_{Sn\ DC}$ which can be divided into two regions. The single-sputtered and co-sputtered SnO thin films at 0 W ≤ $P_{Sn\ DC}$ ≤ 30 W showed polycrystalline SnO phase, while co-sputtered SnO thin films at 40 W ≤ $P_{Sn\ DC}$ ≤ 70 W comprise metallic Sn and SnO phases as the Sn-rich SnO crystal structure, and no other phase formed. All of the Sn atoms at 0 W ≤ $P_{Sn\ DC}$ ≤ 30 W could be oxidized to forming SnO crystal structure by heat treatment process. However, the influence of Sn atoms in the deposited films over 40 W of $P_{Sn\ DC}$ is increased, and all of the Sn atoms seemed to have not been oxidized. This result indicates that the amount of extra Sn atoms by co-sputtering process should be sensitively engineered to control the phase formation between pure SnO and Sn-rich SnO by adjusting $P_{Sn\ DC}$ in Fig. 3.2(b).

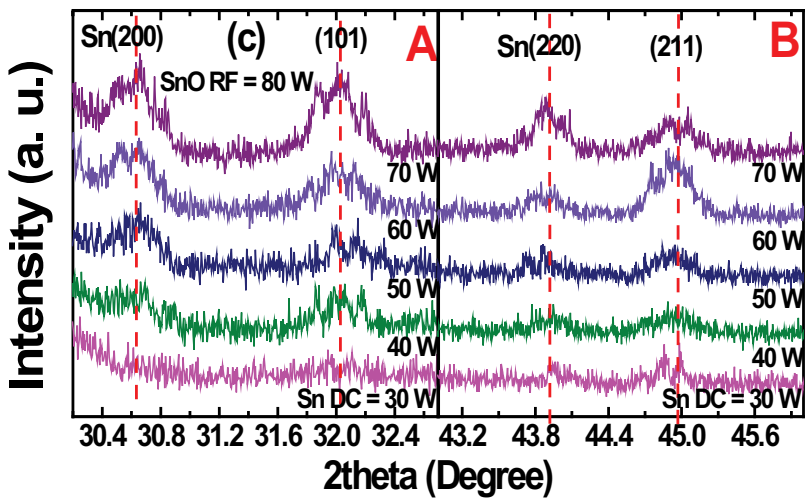

Figure 3.2. (c) The zoom at the red-colored A and B points in GIXRD patterns in Fig. 3.2(b) showing the presence of Sn in SnO thin films increases as the $P_{Sn\ DC}$ increases.

In addition, to confirm the phase characteristics of SnO according to the thickness of the deposited film, the GIXRD measurement performed from 10 to 150 nm of the annealed film. The $P_{Sn\ DC}$ was fixed at 40 W based on the same deposition pressure to investigate the growth of the metallic Sn phase in the SnO phase. No peak was detected in the 10 nm-thick film as the amorphous phase, while each SnO peak and metallic Sn peak started to appear at the 15 nm and 30 nm-thick films. As the film thickness increases up to 150 nm, the intensities of SnO diffraction peaks, as well as the metallic Sn diffraction peaks increased, and the number of SnO and metallic Sn diffraction peaks also increased. Note that the changes in the metallic Sn diffraction peaks with respect to the film thickness clearly confirmed in Fig. 3.2(d). This result means that the portion of metallic Sn in the annealed film increases and the as-deposited film starts to oxidize from the film surface. We can clearly confirm the change from the SnO phase to the Sn-rich SnO phase where metallic Sn phase coexists, which is similar to the result of Fig. 3.2(c). Although the film thickness with the metallic Sn content in the annealed film was increased, the film properties dominated by metallic Sn phase as shown in Fig. 3.2(a) were not found. It can be expected that the number of O atoms, which bonded with the increasing Sn atoms, is also increased. From the GIXRD results in Fig. 3.2, both p-type SnO and Sn-rich SnO phases confirmed, and it has been shown more intuitively that the amount of Sn added to SnO can be sensitively controlled through the co-

sputtering, unlike the Sn DC reactive sputtering method using O gas.

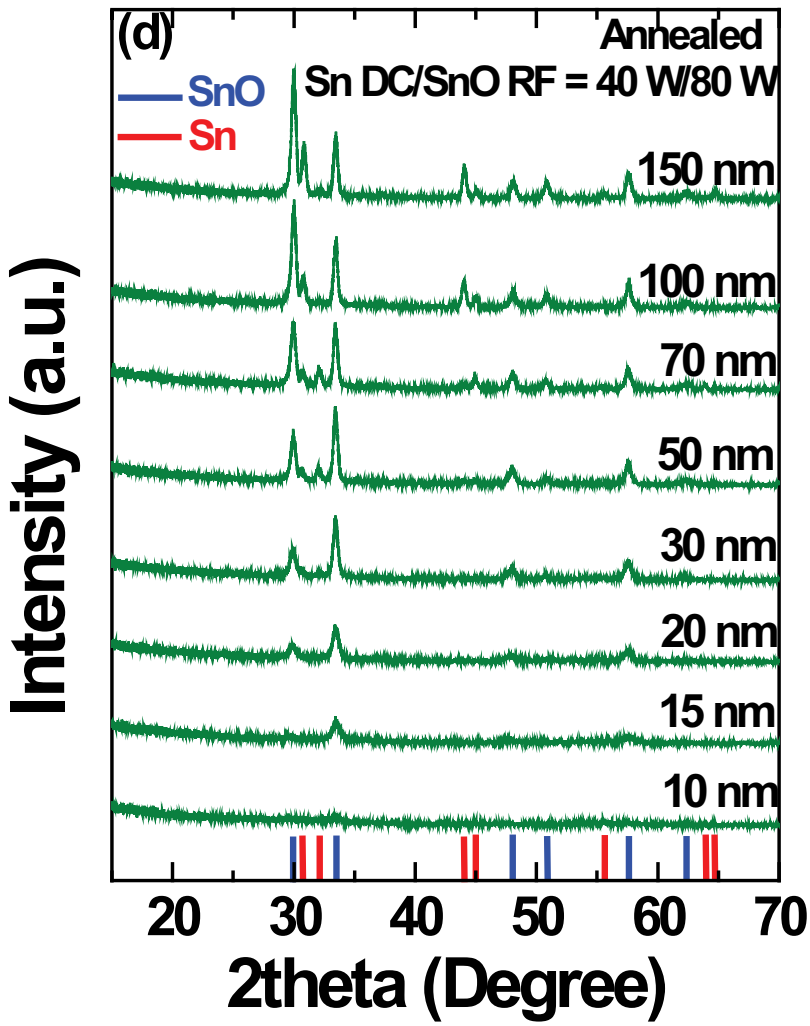

Figure 3.2. (d) GIXRD patterns of annealed films at 40 W of the $P_{Sn\ DC}$ with the fixed $P_{SnO\ RF}$ at 80 W dependence on the film thickness. No pronounced peaks were observed.

The GIXRD patterns of ~100nm-thick films at the as-deposited state and after the PDA at 180 ^{o}C were acquired as shown in Fig. 3.2(e) to confirm that the evolutions of phases during the film growth and heat treatment on the Si and glass substrates are identical. While the peak intensities and their relative ratios are different from the thinner films (~30 nm), the almost identical patterns of the films on Si and glass substrates for the given conditions indicated that the two substrates did not have a substantial influence on the phase evolution.

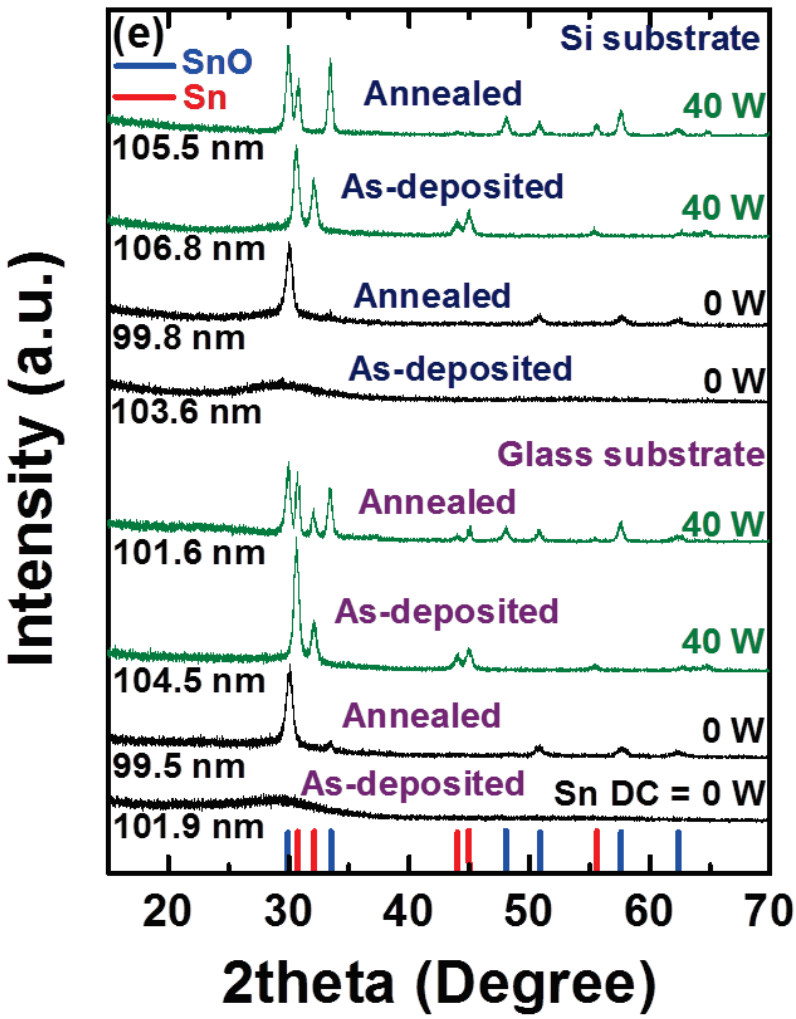

Figure 3.2. (e) GIXRD patterns showing phase formation of 100 nm-thick films on the bare glass and bare Si substrates according to the $P_{Sn\ DC}$ with the fixed $P_{SnO\ RF}$ at 80 W at a deposition pressure of 1.5 mTorr. The estimated film thickness from the XRR fitting for each sample is included in the each left side.

To find the causes of the change in the two main sharp diffraction peaks, we have investigated the peak-positions and intensities of the SnO (101) and (110) from the GIXRD results in Fig. 3.2(b). Figure 3.3(a) illustrates peak-positions of the intensities of the SnO (101) and (110) diffraction peaks observed in Fig. 3.2(b) as a function of the $P_{Sn\ DC}$, and it shows a large difference. The peak-position of SnO (101) shows a shift of less than about 0.05°, which was marked a diagonal-red-line region, but the case of SnO (101) shows a large peak-position shift of about 0.25° which was marked a diagonal-black-line region as shown in Fig. 3.3(a). In contrast to the SnO (110) case, it can be inferred that the SnO (101) peak is disturbed by some external influence in growing. Therefore, it is necessary to deduce why SnO (101) only has a greater influence on the peak-position shifting. Figure 3.3(b) shows the noticeable differences in the intensities of the SnO (101) and (110) diffraction peaks observed as a function of the $P_{Sn\ DC}$. When the co-sputtering started at 10 W of $P_{Sn\ DC}$, the SnO (110) peak first appears in Fig. 3.2(b) and rapidly increased up to 40 W of $P_{Sn\ DC}$, while the SnO (101) peak relatively decreased as $P_{Sn\ DC}$ increased above 50 W. The difference in intensities of the XRD peaks can have many origins such as grain size, lattice defects or parameters information, and preferential crystallite orientation [18]. Among them, we have investigated average grain sizes to explain the tendency of changing intensities for two main SnO (101) and (110) diffraction peaks.

Figure 3.3(c) and (d) show the full width at half maximum (FWHM) and

the average grain sizes of (101) and (110) diffraction peaks. The average grain size of GIXRD patterns calculated by Eq. (1) for the co-sputtered SnO thin films annealed at 180 °C at different $P_{Sn\ DC}$. The average grain size of co-sputtered SnO thin films can be calculated by the Scherrer's formula as follows [25]:

$$\boldsymbol{\alpha = \frac{0.9\lambda}{\beta cos\theta}} \quad (1)$$

where α is the grain size in the co-sputtered SnO thin films, λ denotes the wavelength of Cu Kα (λ=1.5405 Å), β is FWHM of diffraction peaks that solely corresponds to the crystallite size with the instrumental broadening excluded, and θ is the GIXRD peak position, respectively. As indicated in Fig. 3.3(c) and (d), the FWHMs of both SnO (110) and (101) diffraction peaks are inversely proportional to the each tendency of average grain size according to increasing $P_{Sn\ DC}$ by Eq. (1), which can be related to the quality of crystallinity in polycrystalline co-sputtered SnO thin films. The extracted average grain sizes both SnO (101) and (110) diffraction peaks are almost similar ranged about 11-16 nm for all $P_{Sn\ DC}$ ranges irrespective of the crystal planes, and each maximum grain size is obtained at 20 W and at 40 W of $P_{Sn\ DC}$. However, since the degree of change of both SnO (101) and (110) grain sizes were too small, the meaning of the result in Fig. 3.3(d) seemed to be negligible. Note that the intensities of SnO (110) diffraction peaks at 0 and 5 W of $P_{Sn\ DC}$ were too small, and FWHMs could not be extracted.

As shown in Fig. 3.3(b) and (d), the average grain size of SnO (110) diffraction peak is proportional to the intensity of SnO (110) with increasing $P_{Sn\ DC}$. Because the intensity of SnO (110) diffraction peak is increased(decreased) as the FWHM of SnO (110) is decreased(increased) which is directly affected by the average grain size. However, it is difficult to directly define the relationship between the intensity and grain size of SnO (101) according to the $P_{Sn\ DC}$ due to the irregularity of FWHM trend. In the initial $P_{Sn\ DC}$ region, it can be inferred that the SnO (101) was received a disturbance on the growth as a large shift amount of the peak-position. As considered in Fig. 3.2(b) and Fig. 3.3, it can be inferred that the SnO thin films are denser, and the increasing Sn ratio causes the changes in co-sputtered SnO thin film properties, which seem to be directly related to the Sn-rich condition with increasing $P_{Sn\ DC}$. Therefore, it is necessary to investigate the result of the peak-position shift of both SnO (101) and (110), including the reason why the SnO (110) peak-position shift had less effective as compared to the SnO (101) case as shown in Fig. 3.3(a). This different tendency of the intensities and peak-position sifting both SnO (101) and (110) diffraction peaks as a function of the $P_{Sn\ DC}$ will be more discussed on later.

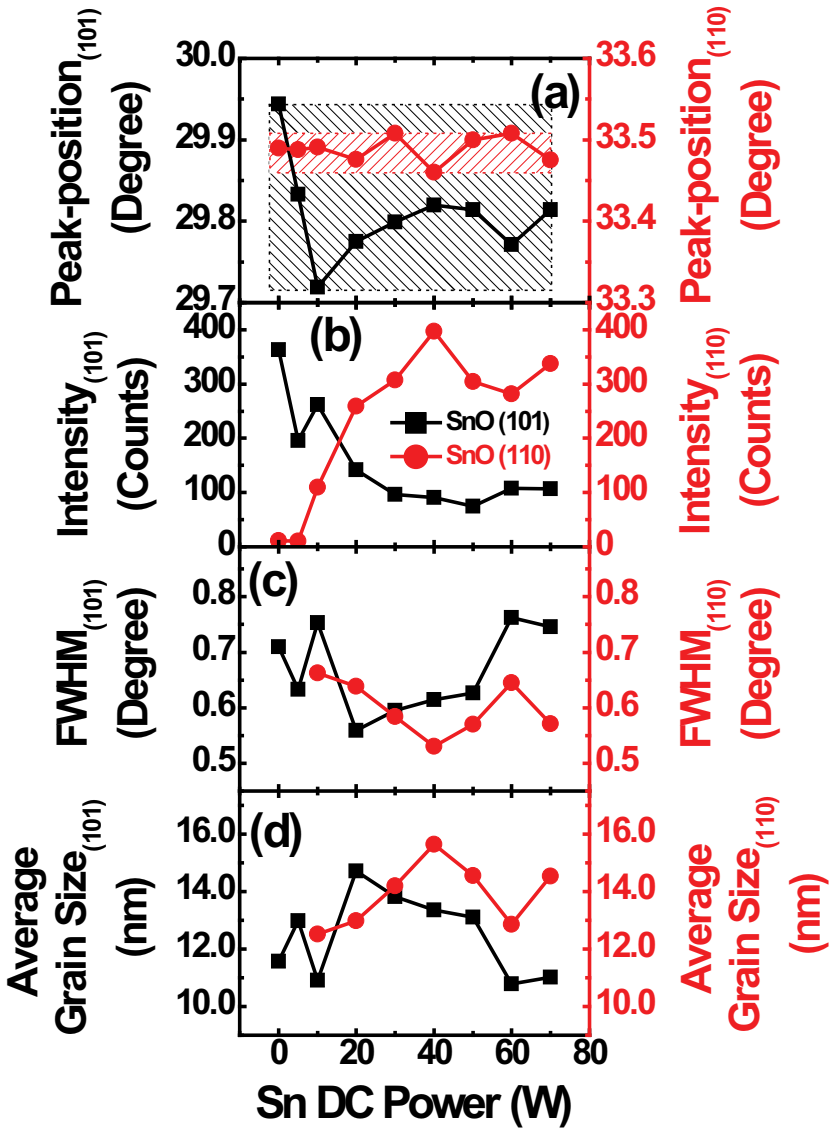

Figure 3.3. Plots of (a) peak-positions and (b) intensities, (c) FWHMs, and (d) average grain sizes of SnO (101) and (110) diffraction peaks with different $P_{Sn\ DC}$ with the fixed $P_{SnO\ RF}$ at 80 W. All results were obtained from GIXRD patterns as shown in Fig. 3.2(b).

3.3. FE-SEM, HRTEM, and AFM analyses

The additional FE-SEM analysis was carried out to investigate the morphologies of the co-sputtered thin films. Figure 3.4 show FE-SEM images which a cross-sectional view of the 30 nm-thick as-deposited thin films on a bare Si substrate with tilted at 200K magnification under the different $P_{Sn\ DC}$ at (a) 0 W, (b) 5 W, (c) 10 W, (d) 20 W, (e) 30 W, and (f) 40 W. The films in the ranging from 0 to 10 W in Fig. 3.4(a)-(c) showed very smooth and featureless morphologies. While starting from 20 W of $P_{Sn\ DC}$, the discernible nanorod-like or ellipsoidal grains with several tens of nanometers along the *c*-axis direction in Fig. 3.4(d)-(f) appeared with brighter than the FE-SEM images in Fig. 3.4(a)-(c). These tiny nanoscale grains indicate that it was randomly intermixed with the majority Sn and minority O atoms inside the film, which is consistent with the fact that the weaker metallic Sn diffraction peaks were appeared to appear from 20 W of $P_{Sn\ DC}$ in the GIXRD analysis in Fig. 3.2(a).

As growing the ellipsoidal grains in perpendicular to the Si substrate with increasing the $P_{Sn\ DC}$, it can be found that the size of hemispherical small swellings by the grains on the surface of the film was also slightly increased, contributing to the tiny increase in roughness of the film surface in Fig. 3.4(d)-(f). This result seemed to be originated that Sn atoms were relatively more deposited than O atoms on the films with increasing the $P_{Sn\ DC}$, as the most dominant factor for the growth of the ellipsoidal grains. Moreover, the

increasing intensities of the diffraction peaks of the metallic Sn phases in Fig. 3.2(a) showed the dependence on the growing ellipsoidal grains by increasing the $P_{Sn\ DC}$ in Fig. 3.4(d)-(f). It can be expected that the ellipsoidal grains are the seed of forming the metallic Sn structure.

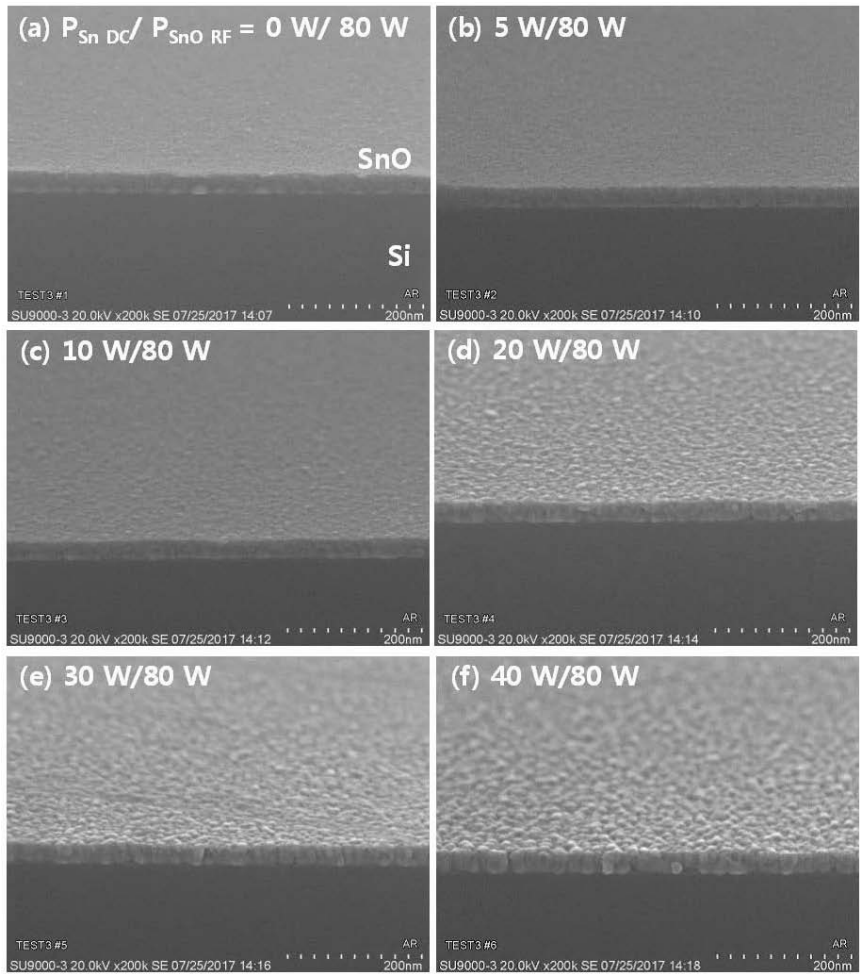

Figure 3.4. FE-SEM images of the 30 nm-thick as-deposited thin films on a bare Si substrate under the different $P_{Sn\ DC}$ at (a) 0 W, (b) 5 W, (c) 10 W, (d) 20 W, (e) 30 W, and (f) 40 W with the fixed $P_{SnO\ RF}$ at 80 W.

Figure 3.5 show FE-SEM images which a cross-sectional view of the 30 nm-thick co-sputtered SnO thin films annealed at 180 °C on a bare Si substrate with the same conditions under the different $P_{Sn\ DC}$ at (a) 0 W, (b) 5 W, (c) 10 W, (d) 20 W, (e) 30 W, and (f) 40 W, respectively. The FE-SEM image at 0 W of $P_{Sn\ DC}$ in Fig. 3.5(a) showed featureless and smooth morphology which was coincident with the result in Fig. 3(a) irrespective the heat treatment. Comparing GIXRD results between before and after heat treatment at 0 W of $P_{Sn\ DC}$, no peak was observed in the as-deposited film in Fig. 3.2(a), while one SnO (101) peak showed in the annealed film in Fig. 3.2(b) despite the smooth surface of the film in Fig. 3.5(a). It seemed to be originated from the only heat treatment. As starting the co-sputtering at 5 W of $P_{Sn\ DC}$, the irregular protrusions, which were not observed in Fig. 3.4, are formed on the surface of the annealed films, and then the protrusions in size and number are increased, which diameters with discernible ranging from about 10 to 160 nm, as the $P_{Sn\ DC}$ increases in Fig. 3.5(b)-(f). When compared with the GIXRD results in Fig. 3.2(b), it can be expected that all SnO and metallic Sn diffraction peaks are related to appearance. As the parts of cutting the irregular protrusion inside the annealed films closely observe in Fig. 3.5(c)-(f), it can be found that the interior of the protrusions, which were the brighter surface and covered on the grey-colored grains, are composed of the densely filled grains in the vertically grown on the Si substrate.

Moreover, the bottom region of partial protrusions showed a crumb shape, not the distinct columnar grains, as if the Sn metal had slightly melted as shown in Fig. 3.5(e) and (f). It can be inferred that the metallic Sn, which was not oxidized, was pushed up to the surface of the film and then it also oxidized, as the metallic Sn contents were excessively contained in the deposited film with increasing the $P_{Sn\ DC}$. This can be found from the cutting protrusions on the film surfaces in Fig. 3.5(e) and (f). As a result, it can be considered that the metallic Sn components detected from the GIXRD results in Fig. 3.2(b) can be existed not only in the protrusions but also in the portion forming the film under the protrusions. As a part of the as-deposited film, which initially existed flatly, oxidized and caused the volume expansion after the heat treatment, the surrounding Sn atoms had highly affected by compressive stress. These Sn components having a relatively low melting point would be softened by the heat treatment and be precipitated on the film surface. Therefore, the metallic Sn states can be possibly formed the area under the precipitated protrusions, due to the atmospheric O prevented from penetrating further into the area during the heat treatment.

This whitening surface of protrusions, which is brighter than the grey-colored surroundings of the films also can be found in Fig. 3.4(d)-(f). Although the brighter surface sizes of swellings in Fig. 3.4(d)-(f) were very small, it was defined the metallic Sn phases from the GIXRD results in Fig. 3.2(a). From this result, it can be expected that the irregular protrusions

including the whitening surface in Fig. 3.5(b)-(f) are composed of the mostly SnO with the small portion of metallic Sn structures which were precipitated from the ellipsoidal grains with coalescences during the heat treatment in Fig. 3.4(d)-(f). However, to define what chemical and structural information of the protrusions have, a TEM analysis should be concerned, which will be discussed on later. While the surface size of the protrusion at 20 W of $P_{Sn\ DC}$ was too small to detect the metallic Sn component in the GIXRD, the metallic Sn diffraction peaks at 40 W of $P_{Sn\ DC}$ appeared in Fig. 3.2(b) and (c), which seemed to be concerned the proportionally increased protrusion with increasing $P_{Sn\ DC}$. To solve the questions related to the protrusions, it is necessary to confirm where the metallic Sn exists in the annealed film. All the roughness at annealed films in the $P_{Sn\ DC}$ ranging from 6.25 to 40 W in Fig. 3.5(b)-(d) increased more than those at as-deposited films in Fig. 3.4(b)-(d), which was due to the irregular protrusions formed.

From the $P_{Sn\ DC}$ at 20 W, the tiny and indistinct hemispherical swellings on the surface of the films appeared and uniformly distributed apart from the irregular protrusions. As increasing the $P_{Sn\ DC}$, these swellings has grown more clearly and increased proportionally in number in Fig. 3.5(c)-(f). These swellings at annealed films are larger in size than those shown in Fig. 3.4(d)-(f), but the number is relatively decreased. It can be inferred that the ellipsoidal grains identified in Fig. 3.4(d)-(f) coalesced with each other, and Sn and O atoms were rearranged during the annealing process. Therefore,

the majority contributed to form protrusions, while the minority contributed to form swellings on the surface of the films in Fig. 3.5(d)-(f). It also can be expected that these swellings act as seeds in forming the protrusions by nucleating themselves and the growth of protrusions on the films was due to the increase of amount Sn atoms.

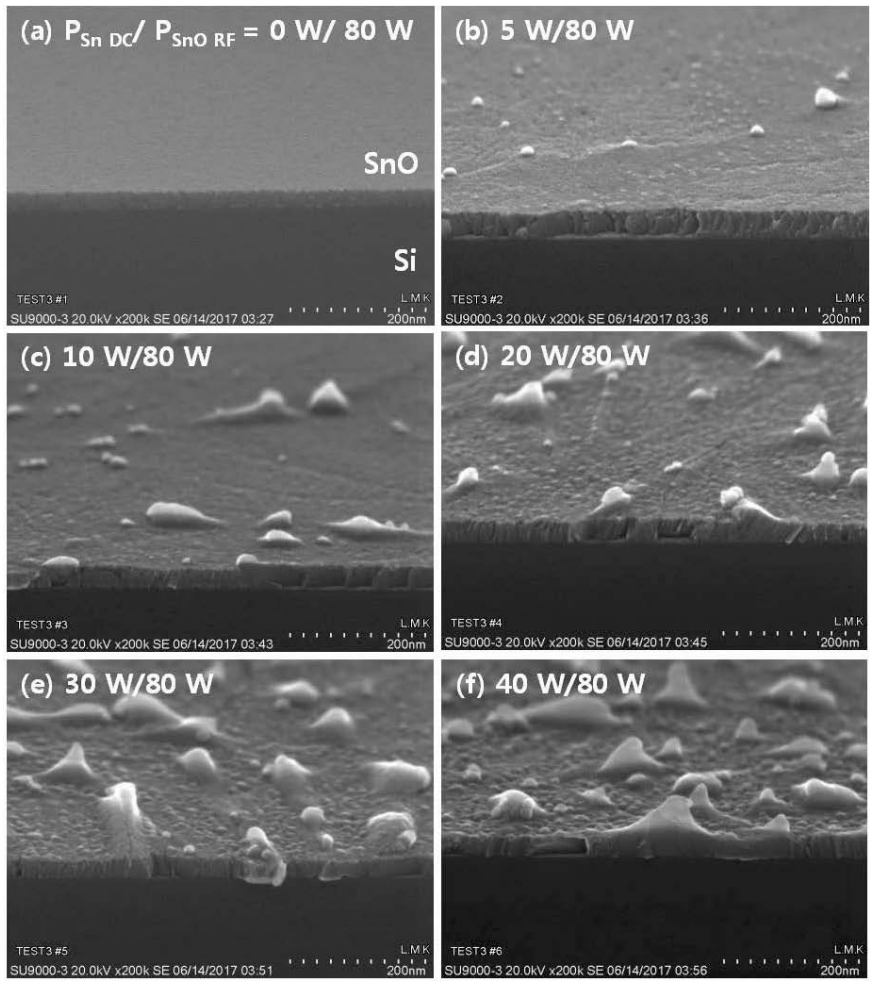

Figure 3.5. FE-SEM images of the 30 nm-thick annealed films at 180 °C on a bare Si substrate under the different $P_{Sn\ DC}$ at (a) 0 W, (b) 5 W, (c) 10 W, (d) 20 W, (e) 30 W, and (f) 40 W with the fixed $P_{SnO\ RF}$ at 80 W.

Figure 3.6(a) and (b) shows the cross-sectional HRTEM image on 20 nm scale of the as-deposited and annealed films, respectively, with the Sn DC power of 40 W in order to define whether the surface part of the whitening protrusions is metallic Sn or SnO phase as shown in Fig. 3.5(f). The as-deposited film shows mostly crystallized polycrystalline microstructure with columnar shape grains, which was corroborated by the GIXRD results in Fig. 3.2(a) and FE-SEM images in Fig.3.4(f). There are remaining amorphous-like regions between the grains, suggesting incomplete crystallization of the entire film. Careful examination of the lattice fringes and fast-Fourier transformation (FFT) shows the presence of crystallized metallic Sn inclusions (JCPDS card no.04-0673) corresponding to the yellow square and its FFT image in Fig. 3.6(c) and (d), which was a coincidence with the GIXRD results in Fig. 3.2(a).

As can be seen the HRTEM image at the annealed case in Fig. 3.6(b), the two regions are shown as upper irregular protruded and lower uniform bulk regions in the film. The amorphous-like regions almost disappear suggesting the enhanced crystallization to the SnO phase after the heat treatment. The large protruded region on the film surface was identified as the crystallized SnO (JCPDS card no.06-0395), as can be understood from the enlarged HRTEM and FFT images in Fig. 3.6(e) and (f), which corresponds to the red squared region in Fig. 3.6(b), which was also coincidence with the GIXRD results in Fig. 3.2(b). The careful examination of the bulk region of the film

revealed that a small portion of the metallic Sn was remained, as indicated by the yellow squared region and its FFT image in Fig. 3.6(g) and (h). Moreover, the tetragonal SnO phase appeared in all the remaining regions except for the yellow square region of the uniform bulk bottom region in Fig. 3.6(b).

In a summary, in the case of the protruded region at the annealed film, excessively deposited Sn rose above the surface of the film through the heat treatment process, and it formed irregular protrusions and reacted with O, and then oxidized to form the SnO phase. Although the SnO also formed in the uniform bulk region of the film during the heat treatment, these SnO protrusions interfere with the O penetration into the uniform region at the bottom of the film surface, and a part of the uniform region still may be possible to maintain the metallic Sn phase as shown in Fig. 3.6(b). Moreover, the probability of finding such region was quite a low suggesting that these regions are isolated, so may not induce metallic electrical conduction through the film.

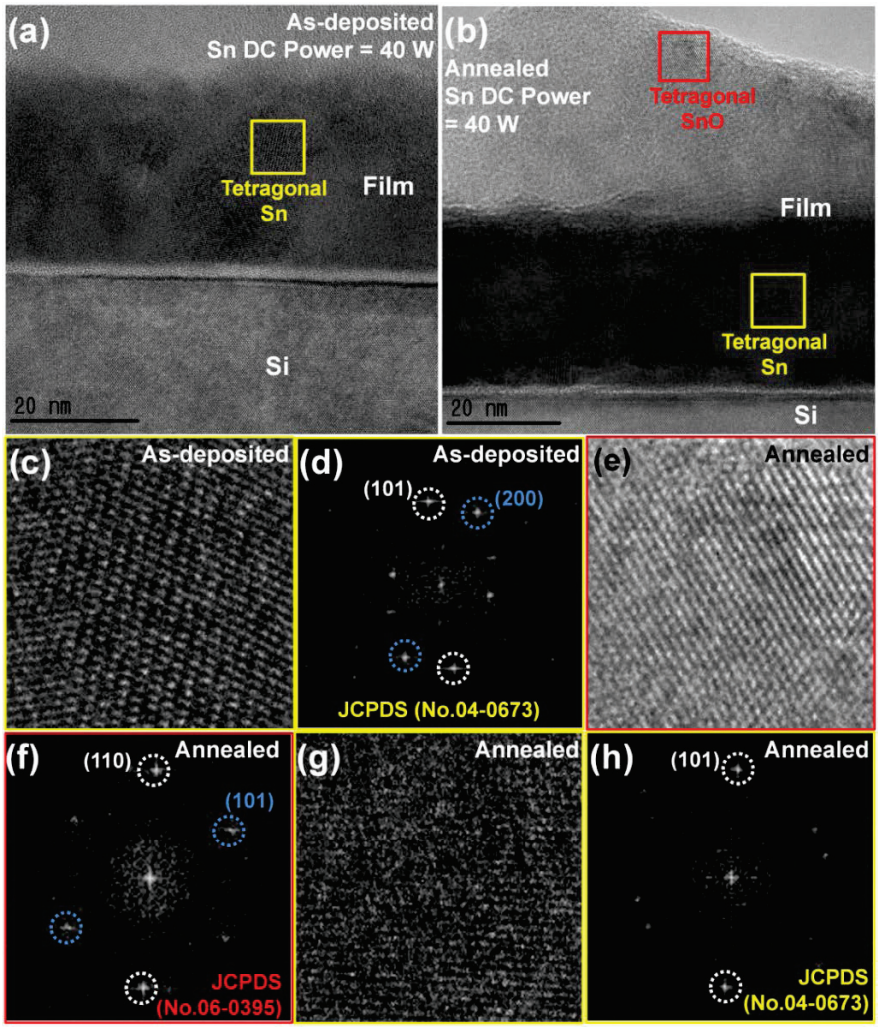

Figure 3.6. HRTEM images of the 30 nm-thick (a) as-deposited and (b) annealed films at 180 °C on a bare Si substrate under the $P_{Sn\ DC}$ at 40 W with the fixed $P_{SnO\ RF}$ at 80 W. (c) The enlarged image and (d) the fast Fourier transform pattern corresponding to the yellow square regions at the as-deposited film in HRTEM images. (e), (g) The enlarged images and (f), (h) the fast Fourier transform patterns corresponding to each red and yellow square region at the annealed film in HRTEM images.

Figures 3.7(a) and (b) show the low magnification of the annular dark field image achieved in the scanning TEM mode (STEM), which also used to acquire the elemental mapping results using energy dispersive spectroscopy (EDS) of the two films in Fig. 3.6(a) and (b). While the as-deposited film did not show any notable features in Fig. 3.7(a), the image of the film at annealed state in Fig. 3.7(b) clearly indicates the presence of surface protrusions (indicated by white arrows). The EDS mapping results of Sn and O of the annealed film from the area enclosed by the white rectangle in Fig. 3.7(b), shown in Fig. 3.7(c) and (d), respectively, to find the metallic Sn aggregates of the protruded and uniform bulk region. It clearly indicated that these protrusions are mostly composed of Sn and O, suggesting that these are SnO. Due to the limited spatial resolution and thick thickness of the TEM specimen, it was not possible to discern the metallic Sn phase from the bulk region of the film. However, the HRTEM image revealed that there are remaining Sn inclusions within the film even after the heat treatment.

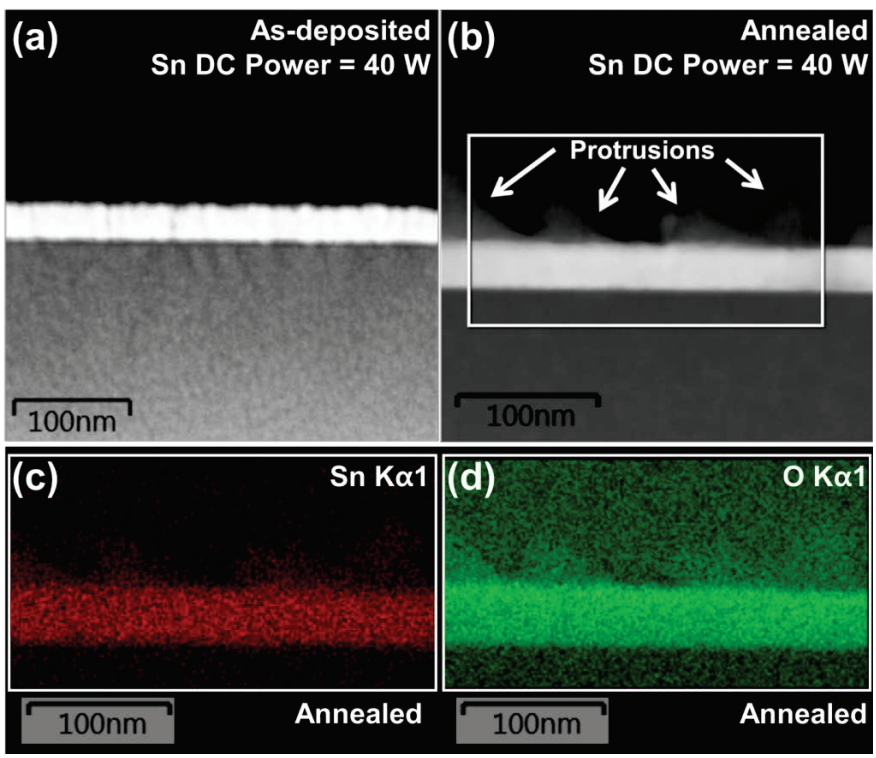

Figure 3.7. STEM-EDS analyses showing electron images of the 30 nm-thick (a) as-deposited and (b) annealed films at 180 °C on a bare Si substrate under the $P_{Sn\ DC}$ at 40 W with the fixed $P_{SnO\ RF}$ at 80 W with (c) Sn, (d) O elemental mappings of the annealed film.

The morphological evolution of the 30nm-thick films grown on the Si and glass substrates under the conditions of 0W and 40 W $P_{Sn\ DC}$s, respectively, were compared using topographic AFM images as shown in Figure 3.8. They also indicate that the different types of the substrate do not have a significant impact on the film morphology. In addion, The roughness tendency of these result were also coincident with the FE-SEM results.

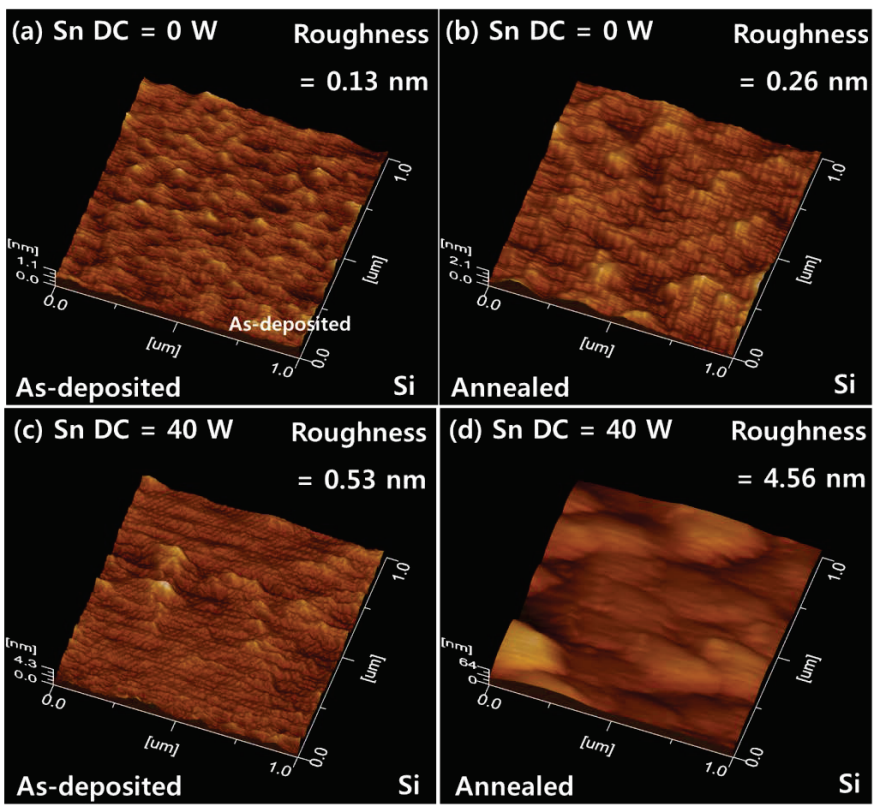

Figure 3.8. AFM topographic images of the 30 nm-thick films on the Si substrate under the $P_{Sn\ DC}$ at 0 W at (a) as-deposited and (b) annealed states, and the $P_{Sn\ DC}$ at 40 W at (c) as-deposited and (d) annealed states with the fixed $P_{SnO\ RF}$ at 80 W.

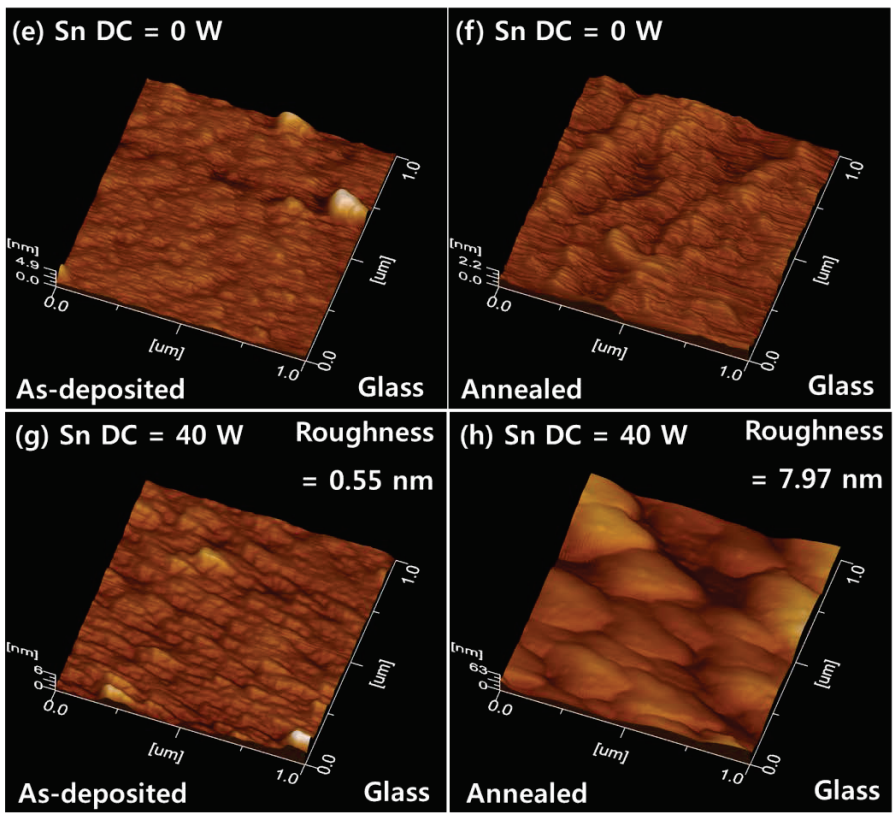

Figure 3.8. AFM topographic images of the 30 nm-thick films on the glass substrate under the $P_{Sn\ DC}$ at 0 W at (e) as-deposited and (f) annealed states, and the $P_{Sn\ DC}$ at 40 W at (g) as-deposited and (h) annealed states with the fixed $P_{SnO\ RF}$ at 80 W.

3.4. Lattice parameters of the co-sputtered SnO

As discussed previously in Fig. 3.2(b) and Fig. 3.3(a), there are slight shifts in the two-strong SnO diffraction peaks related to (110) and (101) planes, regardless of $P_{Sn\ DC}$. We believe that the diffraction peak shifting of SnO (101) and (110) planes are an indication of the strain-related intensity difference, or changing the lattice constants between neighboring Sn and/or O atom distances in the co-sputtered SnO thin films. Therefore, we have investigated the lattice parameters (*a* and *c*) of co-sputtered SnO thin films annealed at 180 °C at different $P_{Sn\ DC}$ to find another cause of the intensity difference. From the peak-position-angles, the lattice spacing *d* between two crystallographic planes can be determined from Bragg's law as follows [52]:

$$\lambda = 2dsin\theta \quad (2)$$

In the case of the tetragonal structure of SnO, the relationship between lattice spacing and lattice parameters is expressed as [53]:

$$\frac{1}{d^2} = \frac{h^2+k^2}{a^2} + \frac{l^2}{c^2} \quad (3)$$

where *h*, *k,* and *l* are the Miller indices of the reflection plane. Thus, using Eq. (3) combined with SnO (101) and (110) planes, the lattice parameters *a* and *c* were derived as follows:

$$a = \sqrt{2d^2} \quad (4)$$

$$c = \sqrt{\frac{a^2d^2}{a^2-d^2}} \quad (5)$$

Figure 3.9 shows lattice parameters *a*, *c*, lattice volume ($V = a \times b \times c$; $a =$

b), and tetragonality (*c*/*a*) as a function of $P_{Sn\ DC}$, which were obtained from the SnO (101) and (110) diffraction angles in Fig. 3.3(a). The derived values of *a* and *c* were ranged from 3.778 to 3.784 Å and ranged from 4.848 to 4.945 Å as a function of $P_{Sn\ DC}$ in Fig. 3.9(a) and (b), also lattice volume and tetragoniality in Fig. 3.9(c) and (d) are extracted in the value ranging from 69.30 to 70.68 $Å^3$ and 1.282 to 1.308, respectively. The average values are about *a* = 3.780 Å, *c* = 4.905 Å, *V* = 70.12 $Å^3$, and *c*/*a* = 1.297 which is incidentally coincident with the 50 W of $P_{Sn\ DC}$ condition. This result is similar with those experimentally determined via the GIXRD patterns of deposited SnO films which were published previously (*a* = 3.802 Å and *c* = 4.836 Å (JCPDS card no.06-0395); *a* = 3.805 Å and *c* = 4.848 Å [54]; *a* = 3.796 Å and *c* = 4.816 Å [55]; *a* = 3.803 Å and *c* = 4.838 Å [56]). Theoretical studies have also reported comparable values: *a* = 3.885 Å and *c* = 4.983 Å [38]; *a* = 3.801 Å and *c* = 4.835 Å [57]; *a* = 3.797 Å and *c* = 4.651 Å [58]. Note that the lattice parameters of literature p-type SnO are referred which is marked with an orange-colored dashed line on the Fig. 3.9 [57].

As shown in Fig. 3.9(a), the lattice parameter *an* of the films is smaller than the value of literature p-type SnO at all $P_{Sn\ DC}$ ranges, and there is not shown in noticeable tendency. It can be considered the contraction of the *a*-axis length which originated from the compressive strain in the *ab* plane of the films. However, it shows a constant lattice parameter *an* irrespective of the $P_{Sn\ DC}$, it seems to be due only to the process environment of the present

sputtering.

When the $P_{Sn\ DC}$ increases from 0 to 10 W, the lattice parameter *c* of the films was significantly increased about 0.1 Å and then it was slightly decreased about 0.05 Å with increasing the $P_{Sn\ DC}$ up to 70 W, which showed the abnormal tendency in Fig. 3.9(b). The lattice volume at 0 W of $P_{Sn\ DC}$ is smaller than the value of literature p-type SnO, as the lattice parameters *a* and *c* are small and similar to one. It means that V_{Sn} (Sn vacancy) seemed to be considerably contained in the film, leading that the lattice parameter *c* abnormally reduced. The fact that the lattice parameter *c* value at 0 W of $P_{Sn\ DC}$ was close to the literature value can be regarded as the SnO lattice along the *c*-axis direction was in a fairly stable state. However, we should be considered that this result may not be true. Since the lattice parameter *a* at all $P_{Sn\ DC}$ is relatively smaller than the literature value, the lattice parameter *c* should be higher than one. The reason for this is that maintaining the constant unit cell volume is an important factor in terms of thermodynamics.

On the basis of this assumption, the SnO lattice at 40 W of $P_{Sn\ DC}$ can be considered as the relatively stable structures due to its lattice volume closer to the literature value, while the SnO lattice at 0 W of $P_{Sn\ DC}$ is far from the stable state due to its lattice parameter *c* similar to the literature value. From this point of view, the lattice volume of $P_{Sn\ DC}$ at 10 W is also far away from the literature value, and it suggested that the SnO crystal structure at 10 W case is also unstable.

The plotted shapes of lattice volume and tetragonality at different $P_{Sn\ DC}$ as shown in Fig. 3.9(c) and (d) are mirrored by the tendency of lattice parameter *c*. Since all values of lattice parameter *a* are lower than the reference value, the temporarily expanded lattice volume up to 10 W of $P_{Sn\ DC}$ can be approximated to the reference value by increasing the $P_{Sn\ DC}$. It can be expected that the co-sputtered SnO thin films based on the same thickness become denser with the relatively stable SnO crystal structure as increasing $P_{Sn\ DC}$.

Comparing the deviations of the lattice parameters *a* and *c* at different $P_{Sn\ DC}$ in Fig. 3.9(a) and (b), the lattice parameter *c* is more varied. The plot of the two lattice parameters *a* and *c* according to the $P_{Sn\ DC}$ in Fig. 3.9(a) and (b) are inversely proportional to each tendency of peak-position shift both SnO (101) and (110) in Fig. 3.3(a). In other words, the peak-position of the SnO diffraction peak is related to the lattice parameters of the SnO unit cell, respectively. Since there was not much shift in the peak-position of the SnO (110), the deviation of the lattice parameter *a* could be very small. However, the peak-position of the SnO (101) has relatively more shifted, and we confirmed that the deviation of the lattice parameter *c* had understandably to be high. It can be explained that the influence of increasing Sn ratio with the $P_{Sn\ DC}$ have affected the changes in the lattice parameter *c* along the *c*-axis. This result in Fig. 3.9 will be more discussed on later.

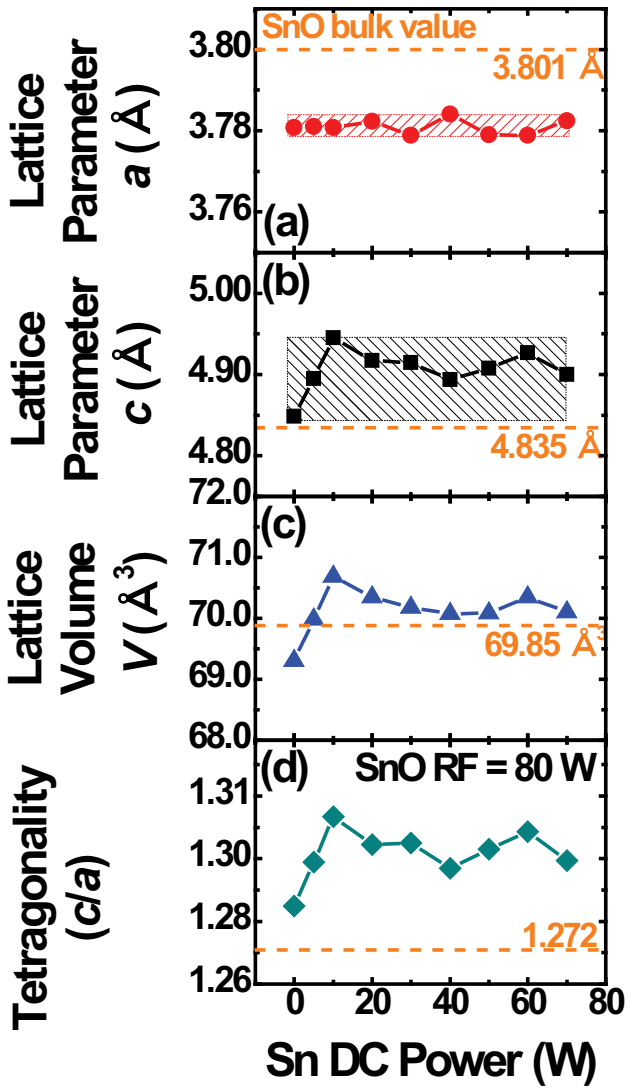

Figure 3.9. (a) Lattice parameter *a*, (b) lattice parameter *c*, (c) lattice volume (a^2c), and (d) tetragonality (c/a) as extracted from the peak-positions of SnO (101) and (110) from the Fig. 3.3(a) at different $P_{Sn\ DC}$ with the fixed $P_{SnO\ RF}$ at 80 W. The horizontal orange-colored dashed lines indicate the literature bulk p-type SnO values.

3.5. Physical properties

The effect of $P_{Sn\ DC}$ on the density of as-deposited and annealed films is investigated by XRR as shown in Fig. 3.10(a) and (b). The estimated thickness of each sample is included in the lower center of the Fig. 3.10 (a) and (b), which are about 30 nm thickness. The density of the films could be evaluated from the critical angle, where the intensity of the reflected X-ray beam is half of the maximum of that in the XRR spectra [59]. From the critical angles of the as-deposited and annealed XRR spectra in Fig. 3.10 (a) and (b), the film density gradually increased with increasing $P_{Sn\ DC}$. The variation of film densities in Fig. 3.10(a) and (b) are estimated and summarized in Fig. 3.10 (c) which are ranged from 5.29 to 6.40 g/cm^3 at as-deposited and from 5.86 to 6.38 g/cm^3 at annealed, respectively. The lowest film densities of both as-deposited and annealed cases are obtained at 0 W of $P_{Sn\ DC}$, and then the film densities are abruptly increased in the initial $P_{Sn\ DC}$ ranges. Up to 70 W of $P_{Sn\ DC}$, the film densities are slowly increased and approached the literature p-type SnO film density (6.45g/cm^3) which is marked with an orange-colored dashed line on the Fig. 3.10(c) [26]. It means that the annealed SnO films become denser by increasing the $P_{Sn\ DC}$ in Fig. 3.10(c), which is in accordance with the result in Fig. 3.9(c).

Figure 10(b) also contains the data for the 30nm-thick as-deposited and PDA samples grown on glass substrate. They show consistent data to the films on the Si substrate. The quantitative densities of the films on the Si and

glass substrates under the identical conditions are tabulated in Table 1.

Figure 3.10(d) depicts the Sn layer densities and Sn atom concentrations of the films at different $P_{Sn\ DC}$, and the Sn layer densities were measured by XRF, respectively. The Sn layer densities of two samples also increased under increasing the $P_{Sn\ DC}$, which ranged from 11.97 to 15.81 μg/cm^2 at as-deposited states and from 11.75 to 15.60 μg/cm^2 at annealed states. The Sn layer densities maintained a similar value for each $P_{Sn\ DC}$, irrespective of before and after the heat treatment. The Sn atom concentrations are extracted from combined the value Sn atomic mass unit (amu; = 118.71 amu = 1.971 × 10^{-22} g) with each film thickness as a function of $P_{Sn\ DC}$ in Fig. 3.10 (a) and (b). The Sn atom concentrations are ranged from 1.99 × 10^{22} to 2.63 × 10^{22} cm^{-3} at as-deposited and from 1.99 × 10^{22} to 2.62 × 10^{22} cm^{-3} at annealed states. Although the lattice volume values according to the $P_{Sn\ DC}$ are different from each other in Fig. 3.9(c), the tendency of Sn atom concentration shows in proportion to the tendency of Sn layer density in Fig. 3.10(d). It is shown that the increasing degree of Sn layer density gradually decreases with increasing $P_{Sn\ DC}$, indicating that the deposited Sn atoms in the films were reached as a certain level of saturation state.

Moreover, the results of XRR and XRF have a common tendency that the notable changes in the film density and the Sn layer density can be found at the earlier $P_{Sn\ DC}$. The film density and the Sn layer density increase rapidly in the initial $P_{Sn\ DC}$ region, and the degree of SnO density and the Sn layer

density increase sharply decrease as increasing $P_{Sn\ DC}$. From the proportional relationship between the SnO film density and Sn layer density in Fig. 3.10 (c) and (d), it can be expected that the amount of deposited Sn increasing with the $P_{Sn\ DC}$ is the dominant factor in the increase of film density.

As compared to the XRR results between as-deposited and annealed films, it showed the similar plot characteristics of the film densities before and after the heat treatment according to the $P_{Sn\ DC}$ in Fig. 3.10(c). It can be explained that the microstructure of the as-deposited films has a direct influence on the increasing tendency of densities for the annealed films due to the heavier Sn weight. The grains of the as-deposited film, which were mainly Sn atoms, oxidized to SnO by the atmospheric O during the heat treatment process to fill the void between the grains. It is consistent with the fact that the metallic Sn phases disappeared and most SnO phases were formed, which can be confirmed from the GIXRD results in Fig. 3.2(a) and (b). As shown in Fig. 3.10(c), the XRR result shows that the densities of the as-deposited films increased after the heat treatment in the initial $P_{Sn\ DC}$ regions. The degrees of increasing film densities are about 0.6 g/cm^3 at 0 W and 0.3 g/cm^3 at 10 W of $P_{Sn\ DC}$. Based on the SnO lattice volumes of the annealed films in Fig. 3.9(c), the contribution of one Sn and O atoms (O = 15.99 amu = 2.656×10^{-23} g) to the density of one SnO unit cell can be roughly calculated from the values of about 2.82 g/cm^3 and 0.38 g/cm^3. This result can be inferred that the O atoms is the most dominant factor when the

XRF results in Fig. 3.10(d) show the similar values to the Sn layer densities before and after the heat treatment.

However, the differences in film densities between before and after the heat treatment rapidly reduced and then disappeared with increasing the $P_{Sn\ DC}$. Considering that the weight of the atoms constituting the film is the most dominant factor on the film density, the amount of Sn atoms, which in mass is heavier about seven times than O, increased in proportion to the $P_{Sn\ DC}$ has the greatest influence on the film density. Although the number of O atoms introduced through the heat treatment increased, the contribution for the increase of the SnO film density by the O atoms was negligible. Because of this effect, since all as-deposited film densities were smaller than the theoretical SnO density, all annealed film densities were also to be smaller than the literature value, even though the amount of Sn atoms increased according to the $P_{Sn\ DC}$ and the densification in the film proceeded through the annealing process. Moreover, the fact that the external O atoms were difficult to penetrate into the film due to the increase of the protrusions can be considered as another reason.

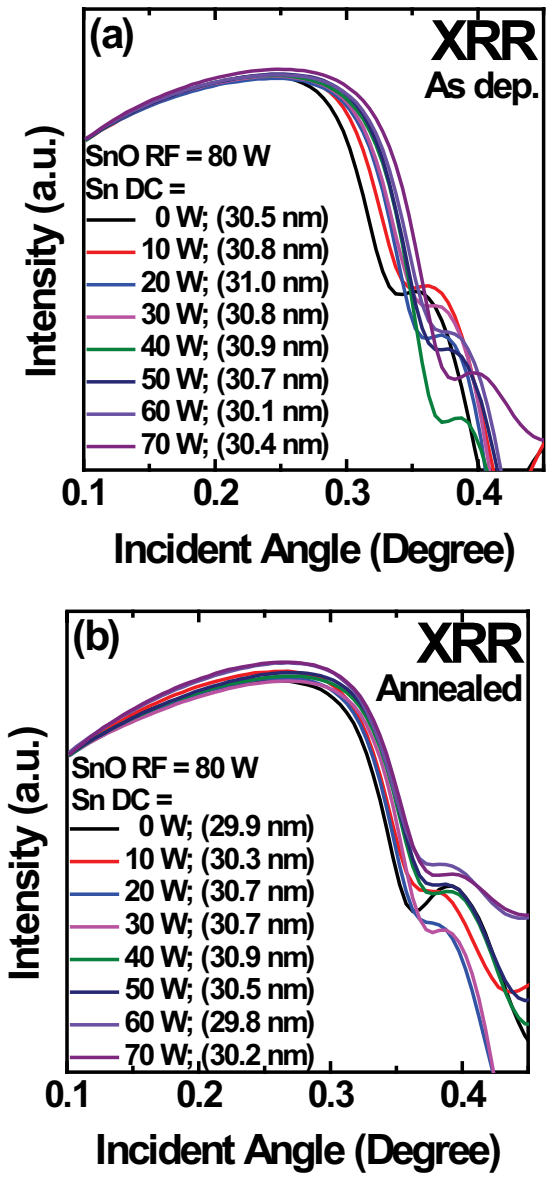

Figure 3.10. (a) As-deposited and (b) annealed XRR spectra under the different $P_{Sn\,DC}$ with the fixed $P_{SnO\,RF}$ at 80 W for the 30 nm-thick deposited films. The estimated thickness of each sample is included in the lower center of the Fig. 3.10(a) and (b).

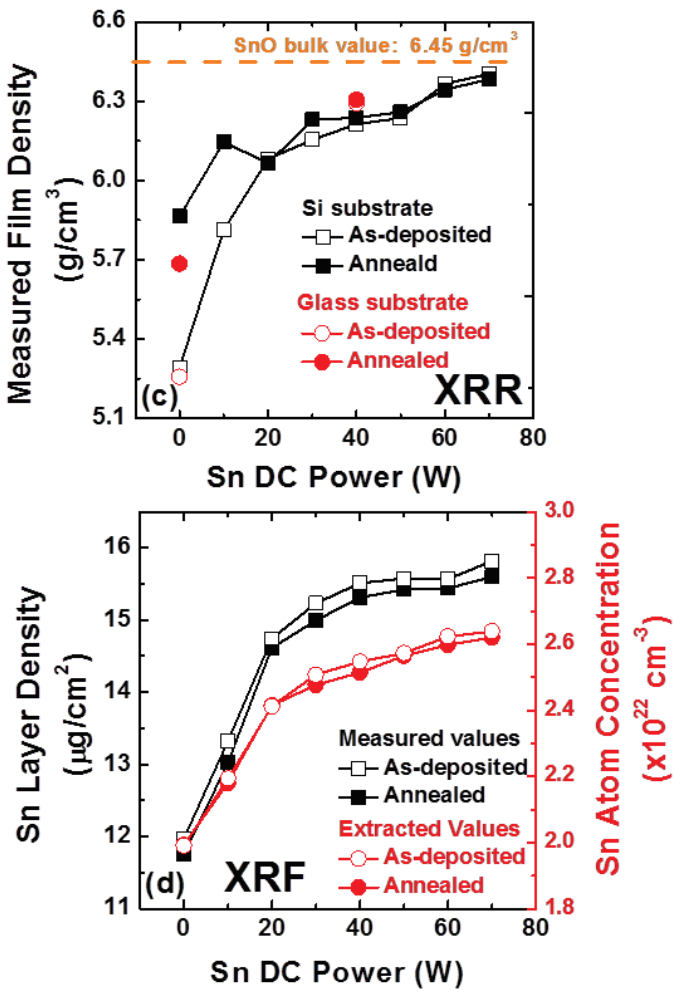

Figure 3.10. (c) Film densities by the XRR, and (d) Sn layer densities and its Sn atom concentrations by the XRF results of 30 nm-thick as-deposited and annealed films on the bare Si substrate according to the $P_{Sn\ DC}$ with the fixed $P_{SnO\ RF}$ at 80 W. The horizontal orange-colored dashed lines indicate the literature bulk p-type SnO values. The XRR results also include the film densities of both 30 nm-thick as-deposited and annealed films on the bare glass substrate.

Table 3.1. The film densities by the XRR at as-deposited and annealed films on the Si and glass substrates according to the $P_{Sn\ DC}$ at 0 W and 40 W with the fixed $P_{SnO\ RF}$ at 80 W.

$P_{SnO\ RF}$ = 80 W $P_{Sn\ DC}$ =	Si substrate		Glass substrate	
	As-deposited [g/cm^3]	Annealed [g/cm^3]	As-deposited [g/cm^3]	Annealed [g/cm^3]
0 W	5.293	5.864	5.258	5.685
40 W	6.213	6.237	6.293	6.305

3.6. SnO unit cell and its lattice vectors

As mentioned above in Fig. 3.3 and Fig. 3.9, the peak-position shift of SnO (101) diffraction peak was much larger than SnO (110), and the lattice parameter *c* also showed a larger change than *a*. We had concluded that this result originated from the increasing amount of Sn atoms and its interferences in the SnO lattice. Therefore, we have investigated the atomic structure of SnO with its lattice vectors. The excess Sn atoms by co-sputtering must be physically considered how many Sn atoms can be possibly entered and where it had positioned in the SnO unit cell with maintaining its structure. Figure 3.11 illustrates the atomic structures of unit cells of p-type SnO. The p-type tetragonal SnO with a layered crystal structure is comprised of four O atoms and one Sn atom, which are forming the adjacent square pyramid Sn-O layers with *ab* sheets by stacking combinations of each other along the *c*-axis direction in Fig. 3.11. The lattice constants and graphical information in Fig. 3.11 referred to the other group's papers, respectively [60-63]. Considering the oxidation state of p-type SnO lattice, the atomic bonding between one Sn atom and four O atoms are composed of two ionic bonding and two covalent bonding. As a result, it can be expected that the theoretical p-type SnO is difficult to construct with the pure ionic bonding.

As shown in Fig. 3.11, the green-colored arrowed lines are marked on the

p-type SnO structure. These lines are lattice vectors in the SnO unit cell representing the distance between the center and the center of each Sn and O atoms, and total nine sections identified. Table 3.2 summarizes the lattice vectors of p-type SnO for literature and 0 W of $P_{Sn\ DC}$ cases which are based on the ionic radii of Sn and O atoms as shown in Fig. 3.11. On the basis of the lattice vectors of the literature p-type SnO published by Allen group [60], the extracted lattice vectors of the p-type SnO at 0 W of $P_{Sn\ DC}$ was obtained. For the 0 W of $P_{Sn\ DC}$, lattice vectors are also considered as the distances between the edge and the edge of each Sn and O ion in order to directly identify the space into which the excess Sn ion can be entered. Considering the diameter of Sn and O in the ionic state and the lattice vectors in the ideal SnO atomic structure in Table 3.2 and Fig. 3.11, it can be expected that only one excess Sn atom can be possibly entered in the interlayer region of one SnO unit cell. It means the interspace between the upper and lower square pyramid Sn-O lone-pairs along the *c*-axis direction by the repulsive force between neighboring Sn atoms, namely the number of lattice vector 4 and 5 in Fig. 3.10. As previous studies providing the description of the bonding in SnO, this maintained interlayer is typically so-called the non-bonded van der Walls (vdW), or lone-pair region [48].

As the co-sputtering begins, each excess Sn atom which is physically unstable between the non-bonded regions is forcibly positioned, leading the temporary *c*-axis expansion up to 10 W of $P_{Sn\ DC}$ by reducing the V_{Sn} and

forming Sn_i (Sn interstitial) in the SnO lattice. From the presence of one excess Sn atom in one SnO unit cell as the Sn-rich SnO, the tetragonality of the SnO unit cell could be maintained in Fig. 3.9(d). If one SnO unit cell physically contains two or more excess Sn atoms, the inherent tetragonality in the SnO lattice will no longer be maintained as the *c*-axis continues to rise. Considering the above results, it can be inferred that the SnO structure does not accept the excess Sn atoms infinitely, but the number of excess Sn, which can enter the SnO unit cell, is limited. This is the reason why the lattice parameter *c* of SnO could not be increased even though the $P_{Sn\ DC}$ increased by more than 10 W with increasing the amount of Sn atoms. Due to the influence of the inserted excess Sn atoms in the non-bonded regions, all lattice parameter *c* in the $P_{Sn\ DC}$ ranging from 10 to 70 W are understandably higher than the reference value in Fig. 3.9(b). From the results in Fig. 3.3(a), Fig. 3.9, and Table 3.2, it can be expected that the inserted excess Sn atoms in the SnO lattice were one of the causes of the large shift of the peak-position for SnO (101). Moreover, the deposition environment of co-sputtering, in which Sn and O atoms densely arranged in the *ab* plane irrespective of the $P_{Sn\ DC}$, can be another reason for constant peak-position of the SnO (110) with increasing the $P_{Sn\ DC}$.

As mentioned above, the increase in lattice parameter *c* about 0.1 Å up to 10 W of $P_{Sn\ DC}$ could be understood from the lattice vectors and the insertion of partial excess Sn in the SnO lattice through the Sn ion diameter in Fig.

3.11 and Table 3.2. However, it is necessary to the reasonable assumption why the reduction of *c*-axis about 0.05 Å after the $P_{Sn\ DC}$ of 10 W abnormally happened, even though the amount of Sn atoms was increased. This structural phenomenon why the lattice parameter *c* was decreased with increasing the $P_{Sn\ DC}$ is expected to be related to the microstructure of the SnO film. At 10 W of $P_{Sn\ DC}$, the film is deposited with the relatively low portion of metallic Sn state. Most of the SnO grains are formed by heat treatment. Since they are rigid ceramics, the excess Sn is forced into the SnO lattice, leading the increasing lattice parameter *c*.

Considering the heat treatment in progress with increasing the $P_{Sn\ DC}$ by more than 10 W, in addition to the formation of SnO by oxidation, the excess metallic Sn atoms, which did not bond with O atoms, migrated to the surface of the film or gathered each other to inside the film, and then formed the soft metallic Sn states. This reason can be deduced from the FE-SEM image after heat treatment in Fig. 3.5, and the low melting point of Sn can also be considered as a cause. It can be inferred that these causes lead to the reduction of the lattice parameter *c* by preventing the small part of excess Sn atoms entering into the SnO and mitigating the stress effect of the film.

Moreover, as compared to the degree of increase in the lattice parameter *c* at the $P_{Sn\ DC}$ ranging from 0 to 10 W by the insertion of the excess Sn in SnO structures, the degree of decrease in the one at the $P_{Sn\ DC}$ ranging from 20 to 70 W is as small as about half in Fig. 3.9(b). This result inferred that the

excess Sn inserted in the SnO lattice does not partially escape and continues to exist. Summarizing the above results, excess Sn atoms are subjected to various behaviors through heat treatment process under different $P_{Sn\ DC}$. The part of them are (1) forming SnO structure through the bonding with O atom, (2) existed of Sni in the non-bonded region of the SnO lattice, (3) contributed to the formation of protrusions as the Sn inside the film rises to the surface, (4) forming the soft metallic Sn phase in the film separately from the SnO phase. It can be deduced the increasing and decreasing tendencies of the lattice parameter *c*.

However, since the Sn_i is known as an electron carrier source, it is difficult to consider in the p-type SnO thin film. Even if the Sn_i is inserted into the non-bonded region of the SnO unit cell, the Sn_i could be easily interconnected with the surround Sn atoms, and these Sn atoms would be precipitated. It can be concluded that the reduction of the *c*-axis by the formation of the soft metallic Sn phases in the annealed films after the heat treatment obtained through the FE-SEM results is insufficient. From this result, the hypothesis about the increasing and decreasing *c*-axis of the SnO crystal structure by insertion and precipitation of the excess Sn atoms is unreasonable, and we have considered another hypothesis.

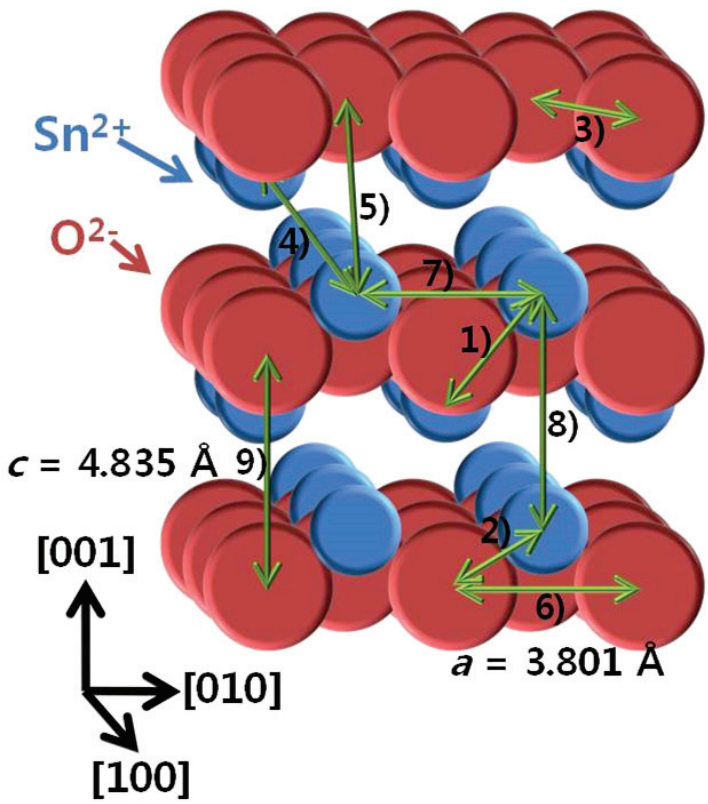

Figure 3.11. A conceptual atomic structure of the ideal unit cells of p-type SnO as referred from the literature based on the first principle calculation. The Sn and O ions are colored blue and red, and the light green-colored lines indicate the lattice vectors of each Sn and/or O atom in the bulk p-type SnO.

Table 3.2. Experimental lattice vectors and atomic bond lengths for p-type SnO with those calculated using the lattice parameters *a* and *c* as extracted from the GIXRD results. The r_{Sn} and r_O are ionic radii of Sn and O atoms, respectively.

Lattice vectors	Direction	Atomic distances in the bulk SnO structure (Å) Ion: r_{Sn} = 0.93 Å, r_O = 1.32 Å (Literature [63])		
		Center to center (Literature [48])	Center to center ($P_{Sn\ DC}$ = 0 W)	Edge to edge ($P_{Sn\ DC}$ = 0 W)
1) Sn – Sn (in-layer)	Diagonal	3.539	3.525	1.665
2) Sn – O (in-layer)		2.222	2.213	- 0.037 (Overlapped)
3) O – O (in-layer)		2.688	2.673	0.033
4) Sn – Sn (across layer) (= non-bonded region)		3.693	3.686	1.826
5) Sn – O (across layer)		4.145	4.150	1.900
6) O – O (across layer)	Horizontal	4.835 (= lattice parameter *c*)	4.848 (= lattice parameter *c*)	2.305
7) Sn – Sn (across layer)				3.085
8) O – O (in-layer)	Vertical	3.801 (=lattice parameter *a*)	3.780 (=lattice parameter *a*)	1.140
9) Sn – Sn (in-layer)				1.920

3.7. Residual stress measurements

We believe that the increase and decrease tendencies of the lattice parameter *c* as shown in Fig. 3.9(b) can be related to the film stress difference by an expansion or a contraction in the deposited films. To confirm the hypothesis, the residual stress measurements of the films were conducted. The stress was measured before and after heat treatment in all the $P_{Sn\ DC}$ ranges, the deposited films were all 30 nm-thick. The stress was obtained by varying the curvatures of the substrates before and after deposition of the films as shown in Fig. 3.12. The stress was then calculated from the Stoney equation as follows [64].

$$\sigma_f = \frac{E_s h_s^2}{6h_f(1-v_s)} \times \left(\frac{1}{R_f} - \frac{1}{R_0}\right) \qquad (6)$$

where E_s is the Young's modulus of the substrate, v_s is Poisson's ratio of the substrate, h_s is the substrate thickness, h_f is the film thickness, R_0 is the initial substrate radius of curvature measured before deposition and R_f is the radius of curvature when the film stress is measured. Since the thickness of the Si substrate is relatively thicker compared to the thickness of the deposited thin film, it is difficult to induce a change in the curvature of the Si substrate. For this reason, in order to maximize the variation of the Si substrate curvature, a thin Si substrate with a thickness of 100 μm was adopted. The stress measurement value for the thin Si substrate before deposition of the film is zero value, and a negative sign of the stress indicates compressive stress,

while a positive sign represents tensile stress. Compressive stress is generated by a force which is acting into or towards the center of an object which is trying to make the object smaller. Tensile stress is generated by a force which is acting away from an object which is trying to stretch the object or make the object bigger. As the films have a restoring force to return to the original state after the deposition process, the film with the tensile stress leads a attraction force between neighboring atoms tending to pull each other at a porous state, while the film with the compressive stress leads a repulsive force between neighboring atoms tending to push each other in opposite direction at a high-density state.

The stress tendency of the as-deposited films shows that the tensile to compressive stress characteristics change as the $P_{Sn\ DC}$ increases. It can be explained by the fact that more Sn atoms by increasing the deposition rates are deposited on the substrate and the densities of the films are increased. It also can be considered the increasing the effect on bombardment ions due to increasing the sputtering power. Stress tendency of annealed films shows all compressive properties irrespective of $P_{Sn\ DC}$. The highest compressive stress value was obtained at the $P_{Sn\ DC}$ of 0 W, and the lowest compressive stress value was reached at the $P_{Sn\ DC}$ of 10 W which means that the tensile characteristic is relatively larger than that of the annealed film under different $P_{Sn\ DC}$ conditions. After the $P_{Sn\ DC}$ of 10 W, the compressive stress value is gradually increasing.

The lowest as-deposited film density at 0 W of $P_{Sn\ DC}$ can be confirmed by the XRR results. As it is the microstructure of the most porous state, high O concentration penetrates into the film during heat treatment process, leading the highest compressive stress characteristic. As a result of the co-sputtering process with a still porous film property at 10 W of $P_{Sn\ DC}$, the non-uniformly deposited atoms on the substrate formed with a stable arrangement with the thermal or lattice relaxation after heat treatment, so that the stress inside the film mitigated and returned to the original state as the tensile characteristic. Based on these results, the stress states of the films at all $P_{Sn\ DC}$ conditions after 10W could be expected to be normally lower than that of the as-deposited films after the heat treatment. However, the compressive properties of annealed films after the $P_{Sn\ DC}$ of 20 W were abnormally stronger than that of as-deposited films. The degree of increasing amount of Sn deposited on the substrate sharply decreased with increasing the $P_{Sn\ DC}$, and it reached the constant saturation level as shown in Fig. 3.10(d). It can be explained that the as-deposited films in the $P_{Sn\ DC}$ latter region, which are relatively dense due to the increased amount of Sn, became denser again due to the excess O atoms penetrating during the heat treatment, leading the substantial oxidation of the incorporated Sn and the higher compressive properties than the as-deposited cases.

The stress tendency, in which the physical properties of annealed films temporarily become tensile characteristics and gradually change into

compressive characteristics with increasing the $P_{Sn\ DC}$, is similar that the tendency of the lattice parameter *c* and unit cell volume at different $P_{Sn\ DC}$ as shown in Fig. 3.9(b) and (c). From this result, it can be seen that the stress states of the annealed films after were reflected the tendency of lattice parameter *c* according to the $P_{Sn\ DC}$. In other words, the increase and decrease in *c*-axis of the SnO unit cell can be explained that the increasing amount of Sn atoms with the $P_{Sn\ DC}$ directly affects the change in the microstructures and properties of the annealed films through the heat treatment process. Moreover, considering the layered structure of SnO, where the atomic packing along the *a*-direction is higher than along the *c*-direction (at the non-bonded region), such structural variation according to the stress evolution can be also understood.

The stress value in the latter region of $P_{Sn\ DC}$ at annealed films about half of that at 0 W of $P_{Sn\ DC}$ as shown in Fig. 3.12, which can be explained as follows. As shown in the FE-SEM images at annealed films in Fig. 3.5, it confirmed that the part of increased Sn atoms induced the irregular protrusions on the film surface or formed soft metallic Sn inside the films. This precipitation process by the Sn atoms excessively existing in the film would induce a structural relaxation of the compressive stress level inside the annealed film.

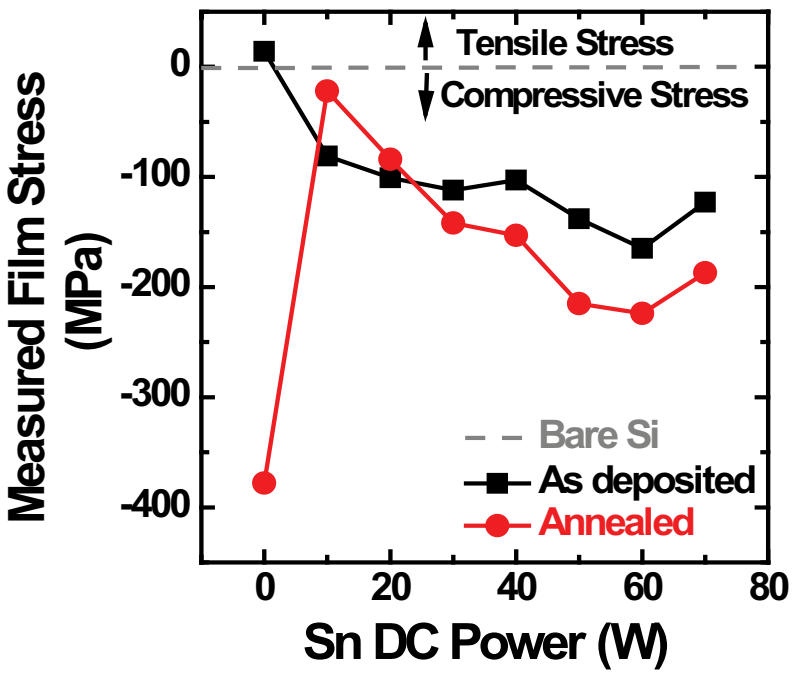

Figure 3.12. Measured film stress of 30 nm-thick as-deposited thin films and co-sputtered SnO thin films annealed at 180 °C dependence on the $P_{Sn\ DC}$ with the fixed $P_{SnO\ RF}$ at 80 W.

3.8. Chemical properties and atomic composition analyses

XPS measurements were performed to further confirm that the 30 nm-thick annealed films co-sputtered the desired p-type SnO stoichiometry and chemical compositions. High doses of Ar^+ ion were used to sputter away the outmost layer, which was shallowly etched about 2-3 nm, to get rid of the carbon contamination as well as the native oxide layer on the topmost of the films so as to obtain the actual composition of the annealed SnO films. The binding energy data were calibrated with respect to the C 1*s* signal of ambient carbon at 284.6 eV. Figure 3.13(a) shows the spin-orbit split Sn $3d_{5/2}$ and Sn $3d_{3/2}$ core-level of the dependence of the film on the $P_{Sn\ DC}$ at a deposition pressure of 1.5 mTorr. The Sn 3*d* spectra in all $P_{Sn\ DC}$ ranges include Sn $3d_{5/2}$ and Sn $3d_{3/2}$ peaks, which averagely located at ~486.2 eV (Sn $3d_{5/2}$) and ~494.6 eV (Sn $3d_{3/2}$), with two shoulders centered at ~484.7 eV (Sn $3d_{5/2}$) and ~493.1 eV (Sn $3d_{3/2}$). It indicated the oxidized states of Sn with two different oxidation numbers in Sn^0 and Sn^{2+}, respectively. This result is similar to those experimentally determined via the XPS data of Sn 3*d* core-level, which was published previously [28, 47, 65]. Moreover, The possible formation of SnO_2 was well suppressed under the entire process conditions due to the co-sputtering process environment.

As the $P_{Sn\ DC}$ increased, Sn^0 shoulder peaks as the metallic Sn, which were

very small at 0 W of $P_{Sn\ DC}$, began to grow and can be confirmed to be increasing in intensities as shown in Fig. 3.13(b). It confirmed that the influence of the increasing Sn atoms with the $P_{Sn\ DC}$ on the SnO film structure is increasing. The degree of Sn 3*d* peak shift at different $P_{Sn\ DC}$ is negligible. The interval between Sn^0 and Sn^{2+} peaks is approximately 1.5 eV, which is agreement with the results of the literature [23, 66]. Only two oxidized states of Sn both Sn^0 and Sn^{2+} are appeared by deconvolution of the Sn 3*d* peaks, and no other peaks are observed in Fig. 3.13(a).

It found that the sharpest increase in the portion of the Sn^0 shoulder peak at Sn 3*d* peak in Fig. 3.13(b) corresponds to the XRR and XRF results in Fig. 3.9(c) and (d), which has the same tendency in the initial $P_{Sn\ DC}$. The portion of the Sn^0 peaks between the $P_{Sn\ DC}$ ranges from 10 to 30 W show similar values in Fig. 3.13(b). This can be related to the microstructure of the protrusion of the FE-SEM image after heat treatment in Fig. 3.5(c)-(e). If there was no significant difference in total area of the annealed film between the three samples from 10 to 30 W of $P_{Sn\ DC}$, it can be inferred that the degrees of remaining metallic Sn were similar. Finally, the portion of Sn^0 peak grown larger as the number of metallic Sn increased at 40 W of $P_{Sn\ DC}$ in Fig. 3.13(b).

Figure 3.13(c) shows the O 1*s* core-level spectra of the dependence of the film on the $P_{Sn\ DC}$. The deconvoluted O 1*s* peaks at ~530.1 eV and ~531.8 eV are associated with oxygen in SnO (O^{2-}-Sn^{2+}) and chemisorbed oxygen

(O_{Chem}) containing species, respectively [21, 65, 66]. The interval between Sn^{2+} and $O^{2-}Sn^{2+}$ peaks is approximately 43.9 eV, which is agreement with the results of the literature [67]. The degree of O 1*s* peak shift at different $P_{Sn\ DC}$ is also negligible. The atomic percentages of Sn and O atoms for the annealed films are included on the left side of the Fig. 3.13(c). As increasing the amount of Sn atoms deposited on the films in Fig. 3.10(d), the composition ratio of Sn atoms relatively increased than that of O atoms with increasing the $P_{Sn\ DC}$, even though all samples have the same Ar^+ ion etching depth, which indicates the proportional relationship. In other words, the degree of excess Sn entering into the total SnO lattices increases as well as the $P_{Sn\ DC}$, indicating the phases of changing from SnO to Sn-rich SnO, which is consistent with the GIXRD results in Fig. 3.2(b).

Moreover, the Sn:O composition ratio of $P_{Sn\ DC}$ at 0 W shows that the composition ratio of O is relatively high compared to Sn, which can be considered to be related the residual stress result of the annealed film at the same condition. The sample at 0 W showed the largest changes in stress value with physical properties of the films before and after the heat treatment as shown in Fig. 3.10(c). When the as-deposited film at 0 W of $P_{Sn\ DC}$ showed the lowest film density due to their relatively higher porosity than other $P_{Sn\ DC}$ samples, it can be explained that the O atoms excessively penetrated into the voids in the film, inducing the high compressive characteristics to the surrounding SnO grains under heat treatment as shown

in Fig. 3.12. It can be expected that the compressive characteristics by the O atoms penetrating between SnO grains with sparsely formed in the annealed film at 0 W are higher than the one by the O atoms penetrating between the metallic Sn regions and SnO grains with densely formed in the annealed film at 40 W. Therefore, the lattice parameter of the SnO unit cell of 0 W samples showed the smallest *c*-axis value abnormally even though it was small *a*-axis compared to the literature value.

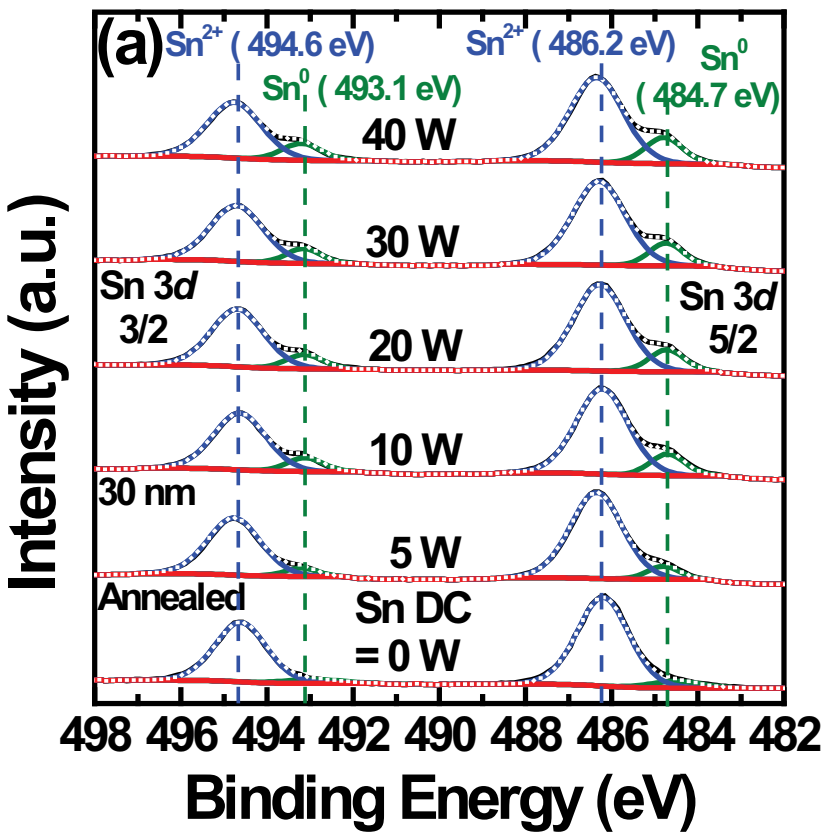

Figure 3.13. (a) The XPS spectra of Sn 3*d* for the 30 nm-thick co-sputtered p-type SnO thin films annealed at 180 °C dependence on the $P_{Sn\ DC}$ with the fixed $P_{SnO\ RF}$ at 80 W.

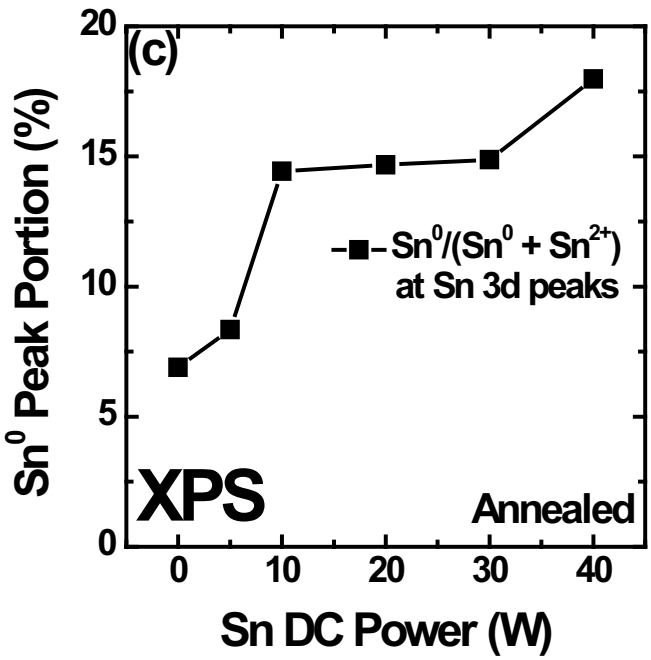

Figure 3.13. (b) The Sn^0 peak portion in total Sn 3*d* peaks from the XPS results in Fig. 3.13(a).

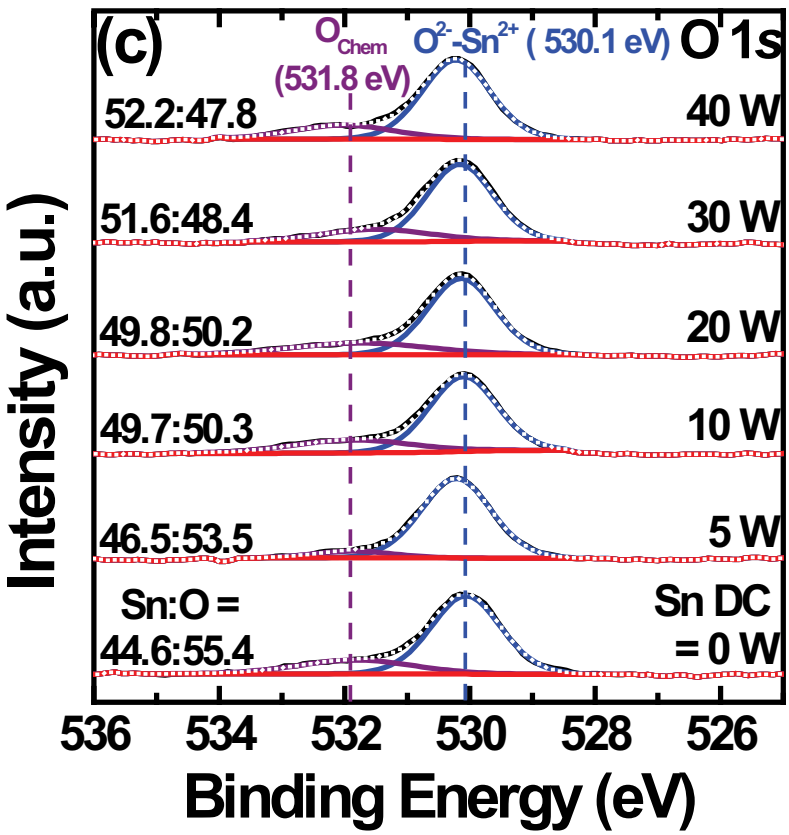

Figure 3.13. (c) The XPS spectra of O 1*s* for the 30 nm-thick co-sputtered p-type SnO thin films annealed at 180 °C dependence on the $P_{Sn\ DC}$ with the fixed $P_{SnO\ RF}$ at 80 W. The atomic percentages of Sn and O atoms for the annealed films are included on the left side of the Fig. 3.13(c).

The further chemical properties of the films were examined. Figure 3.14 shows AES depth profiles of the 30 nm-thick films on a bare Si substrate under the different $P_{Sn\ DC}$ at 0 W with (a) as-deposited and (b) annealed, and at 40 W with (c) as-deposited and (d) annealed. All the films exhibited negligible carbon content. Comparing two as-deposited films in Fig. 3.14 (a) and (c), it confirmed that the relatively high Sn atomic concentration at the $P_{Sn\ DC}$ of 40 W, which was attributed to the co-sputtering condition, and it is coincident with the XRF result in Fig. 3.10(d). The surface of the films at the initial $P_{Sn\ DC}$ region has similar composition ratio levels of both Sn and O atoms. In the interfaces between Si and SnO in Fig. 3.14(a) and (c), the atomic composition ratio of O is relatively higher than that of Sn at 0 W of $P_{Sn\ DC}$. The reason can be explained that a large amount of sputtered Sn atoms from both SnO and Sn targets was more deposited on the Si substrate than O in Fig. 3.14(c), while the O atoms adsorbed to the outmost SnO target sputtered and more deposited on the substrate than Sn in Fig. 3.14(a), as the single sputtering started.

Comparing two annealed films in Fig. 3.14 (b) and (d), the atomic concentrations of Sn and O are about 55: 45 which showed allsmost identical depth profiles across the entire thickness for both samples. As considered the XRF results which showed the similar amount of Sn irrespective of heat treatment in Fig. 3.10(d), the amount of O in the atmosphere also proportionally increased as the amount of Sn increased with increasing the

$P_{Sn\ DC}$ after the heat treatment, leading the similar chemical composition ratio of Sn:O in Fig. 3.14(d). In both samples, it can be expected that the atmospheric O atoms penetrated more into the deposited films at a relative rate during the annealing process. This result corresponds to the GIXRD result in Fig. 3.2(d), which showed that the Sn-rich SnO phase appeared even though the amount of Sn increased as the thickness of the deposited film increased. In the atomic concentration ratio of Sn:O = 55:45 which is the main region in Fig. 3.14(b) and (d), the region at 40 W of $P_{Sn\ DC}$ is longer than that of 0 W. It means that the film at 40 W of $P_{Sn\ DC}$ in Fig. 3.14(d) takes more etching time based on the same thickness of the films, indicating that the film at 40 W of $P_{Sn\ DC}$ became denser with more Sn-O bonding than the 0 W case in Fig. 3.14(b). However, it did not show the difference between SnO and Sn-rich SnO as confirmed from the previous results. Because the area with a diameter of several tens of μm can be probed using the AES, this result cannot discriminate the chemical composition of the uniform region and protruded regions in Fig. 3.14(d).

As considered the as-deposited films in Fig. 3.14(a) and (c), the sputtering time of the Si signal which started to appear at 40 W of $P_{Sn\ DC}$ is faster than that of 0 W of $P_{Sn\ DC}$. It also found that the curve characteristic of the Si has a lower slope in Fig. 3.14(c), while the slope of the Si curve is steeped after the heat treatment in Fig. 3.14(d). The Sn and O atoms seemed to be diffused on the surface of the Si substrate in Fig. 3.14(c), which means that the

surrounding SnO islands are detected at the same time as the Si begins to be detected. This phenomenon can be explained by the fact that both Sn and O atoms are deposited non-uniformly on the Si substrate due to the high deposition rate as dependence on the $P_{Sn\ DC}$ as well as the co-sputtering deposition environment. Considering two as-deposited films as shown in Fig. 3.14(a) and (c), the atomic concentrations of Sn and O atoms at the 0 W case showed the flat depth profile lines and uniformly detected. On the other hand, the deviation of the atomic concentration level at the 40 W case is severe, leading that the Si component in Fig. 3.14(c) could be detected earlier than that of the 0 W of $P_{Sn\ DC}$ in Fig. 3.14(a). In the case of 40 W sample, the unevenly deposited Sn and O atoms were densely rearranged forming the SnO crystal structures after the heat treatment, and the slope of Si curve changed relatively steep compared to that at the as-deposited film as shown in Fig. 3.14(c) and (d). Nevertheless, the Si curves of 40 W samples after heat treatment does not relatively steep compared to those of 0 W samples as shown in Fig. 3.14(b) and (d). Therefore, another reason for the long tailing of the Sn and O profiles into the Si substrate region at 40 W sample can be assumed that the film consists of regions with different etching properties randomly mixed both the small portion of metallic Sn and the mostly SnO regions. It can be also attributed to the above AES depth profile results, and this assumption can be deduced from the HRTEM results in Fig. 3.6(b).

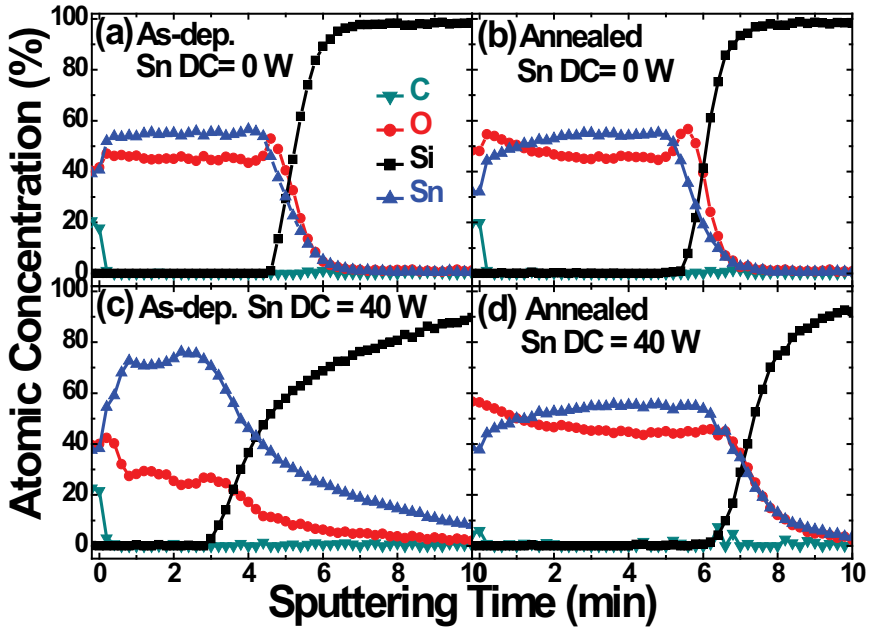

Figure 3.14. AES depth profiles of the 30 nm-thick films on a bare Si substrate under the $P_{Sn\ DC}$ at 0 W with the fixed $P_{SnO\ RF}$ at 80 W at (a) as-deposited and (b) annealed films, and the $P_{Sn\ DC}$ at 40 W with the fixed $P_{SnO\ RF}$ at 80 W at (c) as-deposited and (d) annealed films.

Table 3.3 shows the variations in the atomic ratio (Sn:O) of the films deposited under the different Sn DC power conditions at the as-deposited and annealed states. These data could be achieved using XRF, which could only detect the Sn atomic layer density, and AES, which could detect oxygen as well as the Sn, and interpolation between the different conditions.

To achieve the Sn:O ratio from the XRF and AES, we took the Sn DC power 40W sample as-deposited and after PDA as the representative one. And we achieved Sn layer densities from the XRF and Sn:O ratios from AES of the samples. Then, we can estimate how high the layer densities of oxygen were for the as-deposited and PDA samples by comparing the two data. We did the same thing for the Sn DC power 0W samples and calculated the layer densities of oxygen for the as-deposited and PDA samples. Then, we can estimate the layer densities of oxygen of all the samples, even without their AES data, by the interpolation, which could be easily converted to the atomic ratio from their respective layer density values.

In fact, such a method for estimating the Sn:O ratio is based on the assumption that the sputtered material from the SnO target is SnO molecules, and sputtered material from the Sn target is Sn atoms, which do not mutually interfere. It also assumes that the oxygen concentration increase during PDA is mostly due to the oxidation of Sn. The good coincidence of the calculation based on this method and chemical analysis by AES and XPS reveal that these are reasonable assumptions.

Table 3.3. The Sn:O atomic composition ratios at as-deposited and annealed films dependence on the $P_{Sn\ DC}$ ranging from 0 to 70 W with the fixed $P_{SnO\ RF}$ at 80 W. It calculated from the XRF results with the AES results based on 40 W of $P_{Sn\ DC}$ at as-deposited and annealed films.

SnO RF = 80 W Sn DC =	As-deposited Sn:O	Annealed Sn:O
0 W	56:44	44:56
10 W	61:39	48:52
20 W	67:33	53:47
30 W	70:30	54:46
40 W	71:29	55:45
50 W	72:28	56:44
60 W	73:27	57:43
70 W	74:26	57:43

3.9. Electrical properties

Figure 3.15(a) shows the dependency of carrier concentration, Hall mobility, and electrical resistivity on different $P_{Sn\ DC}$ to investigate the electrical evolution of the films. The Hall measurements of the 100 nm-thick co-sputtered SnO films annealed at 180 °C evaluated at RT. The 60 nm-thick Au contact electrode deposited on the films.

As the previous experiment, which was not shown in data, when the Hall measurements were performed under 100nm-thick co-sputtered SnO films (note that the film thickness used as followed experiments was at 10, 15, 30, 50, and 70 nm on every $P_{Sn\ DC}$), the resistivity showed a very high value. The sign of two cross hall coefficients was also inconsistent which could not be defined the conductivity types of the films. It concluded that the Hall measurement was failed due to the implausible results of both the resistivity and the sign of the coefficient every measurement on the same sample. In order to find this reason, we measured the resistance of the films as previously made for the measurements. As expected, the resistance showed values ranging from several mega to tens of mega-Ohms for each film with different $P_{Sn\ DC}$. Because of the very high resistance value of the films, the Hall measurement results were not reliable and reasonable. A reliable Hall measurement criterion is that the resistivity value should be constantly measured when measured continuously on the same sample.

To obtain the reliable results, the film thickness increased from 30 to 100 nm. Finally, the resistivity of each 100 nm-thick sample measured constantly and repeatedly on every $P_{Sn\ DC}$. As previously reported by J. A. Caraveo-Frescas *et al*., they conducted the Hall measurements of the 150 nm-thick deposited SnO films by Sn DC reactive sputtering [68]. It is the similar case of the film thickness for the Hall measurements. In addition, these Hall measurements have been performed out five to ten times on the same sample in a Greek-cross patterned for each $P_{Sn\ DC}$ condition to obtain the reliable and precise results. Error bar was marked in all carrier transport data of the annealed films on every $P_{Sn\ DC}$ condition. The average values are plotted in Fig. 3.15(a), which are summarized in Table 3.4, respectively.

The Hall measurement results of 100 nm-thick co-sputtered SnO thin films can be roughly divided into two regions with (1) and (2), based on the carrier concentration and its polarity in Fig. 3.15(a). (1) 0 W $\leq P_{Sn\ DC} \leq$ 40 W, in which the co-sputtered SnO thin films indicate the p-type semiconducting behavior dominated by the p-type SnO phase with well-controlled metallic Sn amounts in the film. In this region, the hole carrier concentration, which polarity was plus, is slightly changed which has abnormal trend from 2.8 × 10^{17} to 5.4 × 10^{18} cm^{-3}. The Hall mobility shows an increasing trend from 1.5 to 8.8 $cm^2/V{\cdot}s$. The electrical resistivity decreases from 0.1 to 8.4 Ohm·cm, which is inversely proportional to the carrier concentration, respectively. The maximum Hall mobility of 8.8 $cm^2/V{\cdot}s$ is obtained at 40 W of $P_{Sn\ DC}$ which

accidentally does correspond to the Sn diffraction peaks first appeared at 40 W of $P_{Sn\ DC}$ as indicated the Sn-rich SnO phase in Fig. 3.2(b). This result means that the well-controlled amount of metallic Sn in SnO structure would enhance the Hall mobility, which was coincident with the published results [18].

As mentioned above, the hole carrier concentration decreased once, and then increased gradually in Fig. 3.15(a), which indicated the inverse relation with the plot tendency of SnO unit cell volume in Fig. 3.9(c). Considering the result in Fig. 3.9(c) based on the constant film thickness irrespective of $P_{Sn\ DC}$, it can be expected that the increase(decrease) in the volume of SnO unit cell means the decrease(increase) in the number of SnO unit cells per unit volume of the film. The reason why the hole carrier concentration decreased from 0 to 10 W of $P_{Sn\ DC}$ is due to the decrease in the number of SnO unit cells in Fig. 3.9(c) and the increase in the amount of Sn atoms in Fig. 3.10(d) in the same $P_{Sn\ DC}$ region. As the V_{Sn} positions inside the SnO lattice were partially filled by the increased Sn atoms, it can be expected that the amount of ionized V_{Sn} as the hole carrier source was reduced. Therefore, it can be understood that the Hall mobility increased due to decreased hole concentration at 10 W of $P_{Sn\ DC}$, while the Hall mobility at 0 W of $P_{Sn\ DC}$ was low due to the relatively high hole concentration and poor SnO crystallinity.

Although the amount of Sn atom is still increased after 10 W of $P_{Sn\ DC}$, however, the hole carrier concentration shows an abnormal characteristic as

if the ionized V_{Sn} increases in Fig. 3.15(a). This trend of the hole carrier concentration in the range from 10 to 40 W of $P_{Sn\ DC}$ in Fig. 3.15(a) can be explained to be related the result of residual stress measurements at annealed films as shown in Fig. 3.12. As considered both tendencies between the hole carrier concentration and the residual stress results based on the $P_{Sn\ DC}$ at 10 W, the compressive stress value increased with increasing the hole carrier concentration, which exhibited the proportional relationship. It can be confirmed that the lattice parameter *c* started to decrease from the $P_{Sn\ DC}$ at 10 W even though the lattice parameter *a* was constant in all $P_{Sn\ DC}$ ranges. It means that the applied compressive stress of the annealed films leads the decreasing the volume of the SnO unit cell. It was induced by the incorporation of oxygen into the Sn-excessive film during the heat treatment. The intake of oxygen can increase the internal volume of the material changed from the metallic Sn at the as-deposited state to the SnO at the annealed state, leading the compressive stress. This compressive property, which affected the neighboring SnO structures, leads to increasing the V_{Sn} inside the SnO unit cell due to forcibly coming out the excess Sn from the SnO to form the protrusions. Moreover, it can be expected that the increasing protrusions induced the partially formed disordered SnO structure inside the annealed film due to the escaped Sn. This assumption described in detail in fig. 3.15(b).

For another reason, it is necessary to consider the optical analyses as previous results. As mentioned above, the part of the increased Sn atoms according to the $P_{Sn\ DC}$ formed protrusions on the annealed films as shown in the FE-SEM images in Fig. 3.5(c)-(f). The uniform bulk region of the annealed film revealed that the small portion of the isolated metallic Sn region was as shown in the HRTEM image in Fig. 3.6(b). Form these results, it can be deduced that the reason why the metallic Sn could be remained was that the penetration of external O into the bulk region of the film was largely suppressed by the protrusion formation. Therefore, the partial Sn, which does not form a lattice, could not penetrate into the SnO lattice in the uniform bulk region and the amount of ionized V_{Sn} defects could be increased in proportion to the increase in the number of SnO unit cell with increasing the $P_{Sn\ DC}$ ranging from 10 to 40 W. It shows that the tendency in the hole carrier concentration is inversely related to the unit cell volume of SnO.

In the region (1), the Hall mobility and $P_{Sn\ DC}$ showed the proportional relationship, which indicated that the Hall mobility of Sn-rich SnO phase was higher than that of SnO phase. It also showed that the Hall mobility is gradually increased irrespective of the hole carrier concentration. It can be explained to the combination effect on the decreasing the lattice parameter *c* accompanied by increasing the film density as well as the trap-mediated hopping conduction. However, the reason why the Hall mobility increases,

even though the hole carrier concentration increases, can be assumed that the hole carrier conduction mechanisms of the samples between before and after 10 W of $P_{Sn\ DC}$ are different. The tendencies between the Hall mobility and hole carrier concentration shows the inverse relationship in the $P_{Sn\ DC}$ ranges from 0 to 10 W, which means the hole conduction in the valence band, which can be confirmed by the polycrystalline structure. On the other hand, the one shows the proportional relationship in the $P_{Sn\ DC}$ ranges from 10 to 40 W, which means the hopping conduction at the valence band edge, which can be confirmed by the n-type amorphous or disordered structures for the percolation hopping conduction [3, 5, 69, 70]. It can be explained that the higher carrier concentration leads the higher probability of filling the deep trap sites in the valence band. This implies that the carriers in the shallow trap sites in the valence band, where the carrier has relatively lower energy barriers, can be moved more easily, leading the increasing the Hall mobility. This hopping conduction may be induced by the existence of disordered semiconductor regions in the microstructure of the annealed films in the $P_{Sn\ DC}$ ranges from 10 to 40 W.

Moreover, considering the degrees of increasing Hall mobility according to each $P_{Sn\ DC}$ ranges in Table 3.4, it was about 1.4 $cm^2/V{\cdot}s$ from 0 to 10 W and about 2.2, 1.8, and 2.0 from 10 to 40 W. It showed that the increase rate of the Hall mobility for each section had been larger after 10 W of $P_{Sn\ DC}$. In 2017, V. Ha *et al.* reported that the Sn-O-Sn angles should be as close as

possible to 180° to maximize the overlap between Sn-s and O-p orbitals and to minimize the hole effective mass for obtaining the high Hall mobility [71]. This report obtained from the first-principle calculation, respectively. When combined with the literature and the lattice parameters *a* and *c* in Fig. 3.9(a) and (b), it can be expected that increasing(decreasing) the *c*-axis according to the $P_{Sn\ DC}$ means decreasing(increasing) the bonding angle of the Sn-O-Sn due to the constant *a*-axis of Sn or O atoms arranged on the *ab* plane. This result is in good agreement with the above literature.

In the region (2) 45 W ≤ $P_{Sn\ DC}$ ≤ 70 W, the films exhibit metallic behavior due to the formation of the percolation path of the metallic Sn clusters in the film with an influence of the excessively increasing Sn as well as the film thickness. In this region, the carrier concentration, which polarity was a minus, is significantly higher ranged from about 10^{21} to 10^{23} cm^{-3}. The resistivity is lowered by about 4 orders of magnitude relative to those of the region (1) which decreased from 1.3 × 10^{-3} to 1.0 × 10^{-4} Ohm·cm. As considered these resistivity values, it is not indicated the pure metallic Sn properties. Note that the resistivity of tungsten is 5.6 × 10^{-6} Ohm·cm at 20 °C [72]. The Hall mobility significantly decreases from 3.2 to 0.5 $cm^2/V{\cdot}s$, which is very lower than the Hall mobility at 0 W ≤ $P_{Sn\ DC}$ ≤ 40 W.

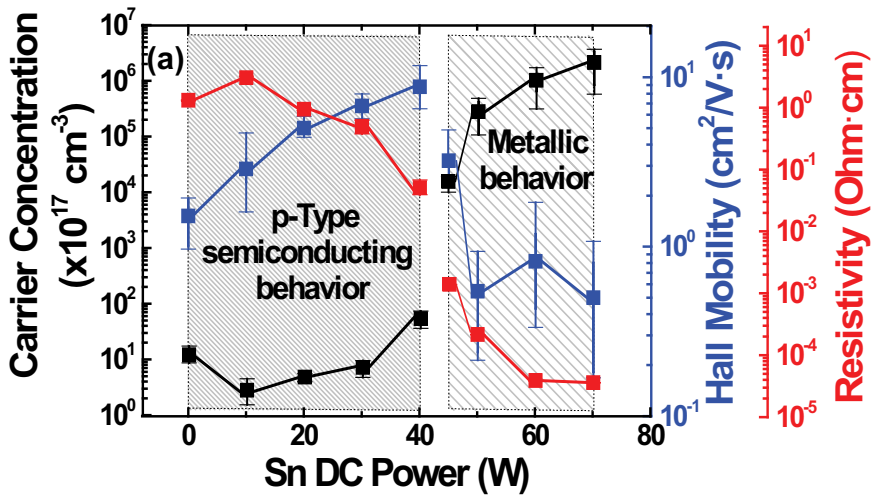

Figure 3.15. (a). The plot of carrier transport data of the 100 nm-thick annealed films at 180 °C in the $P_{Sn\ DC}$ ranging from 0 to 70 W with the fixed $P_{SnO\ RF}$ at 80 W.

Table 3.4. Carrier concentration, Hall mobility, resistivity as extracted from Hall effect measurements dependence on the $P_{Sn\ DC}$ ranging from 0 to 70 W with the fixed $P_{SnO\ RF}$ at 80 W. (Note that the reported values are the average of 5-10 valid results which obtained from the Hall measurements of several tens of times performed on the given sample of every condition).

Annealed at 180℃	p-Type semiconducting behavior					Metallic behavior			
$P_{Sn\ DC}$ [W] ($P_{SnO\ RF}$ = 80 W)	0	10	20	30	40	45	50	60	70
Mobility [cm^2/Vs]	1.5	2.8	5.0	6.7	8.8	3.2	0.5	0.8	0.5
Carrier conc. [cm^{-3}]	1.2×10^{18}	2.8×10^{17}	4.8×10^{17}	7.1×10^{17}	5.4×10^{18}	-1.5×10^{21}	-2.8×10^{22}	-1.1×10^{23}	-2.1×10^{23}
Resistivity [Ohm·cm]	3.7	8.4	2.6	1.5	1.3×10^{-1}	1.3×10^{-3}	6.0×10^{-4}	1.1×10^{-4}	1.0×10^{-4}

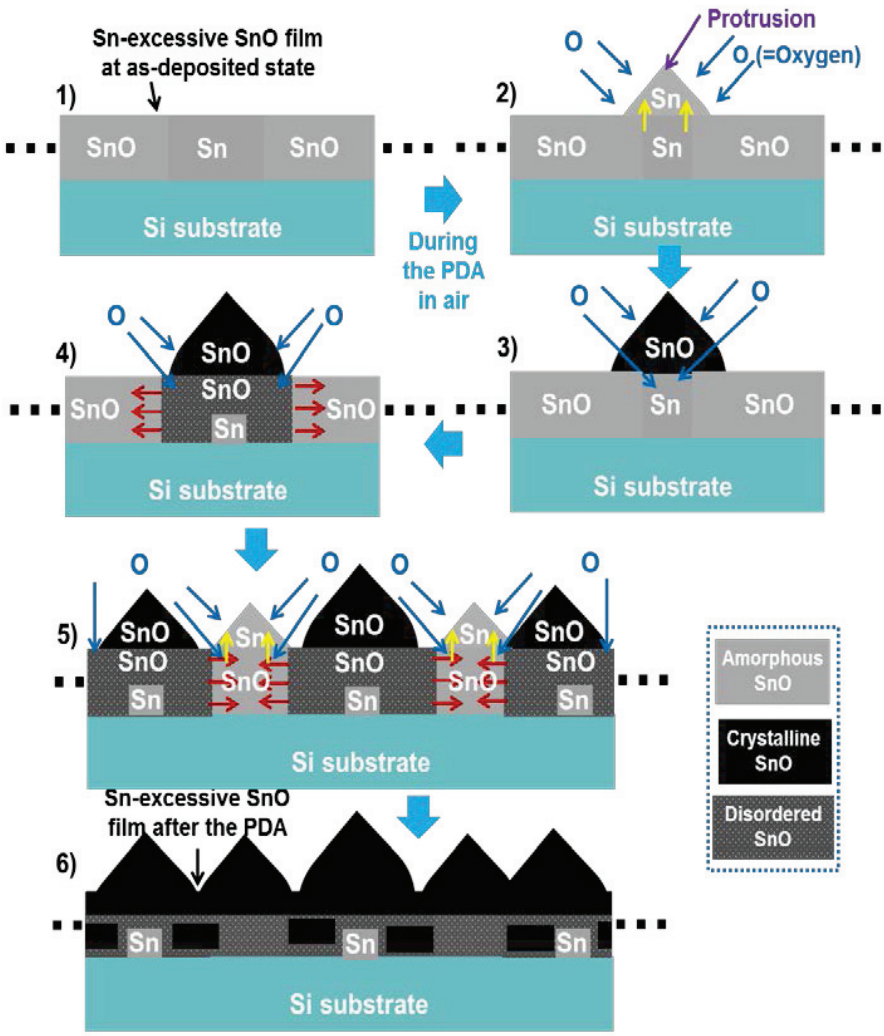

Figure 3.15. (b). The schematic diagrams of the 40 W of $P_{Sn\ DC}$ film explaining the increasing V_{Sn} due to the compressive stress during the heat treatment in air.

In the region (1) of Fig. 3.15(a), the phenomenon of increasing Hall mobility irrespective of the tendency of the hole carrier concentration can be explained to the hypothesis. It means that the hole carrier conduction mechanisms between the single sputtered SnO film at 0 W and the co-sputtered SnO film at 40 W of $P_{Sn\ DC}$ were different due to the difference of in microstructure states inside the annealed films. To obtain the further analysis, the Hall measurement was performed according to the annealing temperature. For comparative analysis of the results, two samples for specific $P_{Sn\ DC}$ conditions selected with the 0 W representing the SnO phase as a reference and 40 W representing the Sn-rich SnO phase showing the highest mobility. The thickness both SnO film and Au electrode were adopted the same conditions in Fig. 3.15(a), and the parameters are the annealing temperatures applied to the thin film, ranging from RT to 400 °C.

Figure 3.16(a) shows the Hall measurement result according to the annealing temperatures at 0 W of $P_{Sn\ DC}$. The p-type semiconducting characteristic was only obtained by the annealing temperatures ranging from 180 to 250 °C. The measurement result in the other annealing temperature ranges could not be obtained due to the extremely higher resistivity values about the mega unit level (note that the film was not sufficiently crystallized and no carriers were generated under 150°C, and too high annealing temperature may induce too much oxidation and no carriers can be also generated above 300 °C). The average values are plotted in Fig. 3.16(a),

which are summarized in Table 3.5, respectively. In the region showing p-type semiconducting behavior, the degree of increase in Hall mobility is relatively small compared to the degree of decrease in hole carrier concentration, which showed the inverse relationship. This is due to the fact that the resistivity is highly increased, indicating that the Hall mobility does not simply increase in inverse proportion as much as decreasing the hole carrier concentration. It can be explained that more external O may penetrate into the SnO film as increasing the annealing temperature, thereby reducing the hole mobility while filling the V_{Sn} position and leading the increase of the resistivity. This tendency can be confirmed by the case at 40 W of $P_{Sn\ DC}$ in Fig. 3.16(b).

Figure 3.16(b) shows the Hall measurement result according to the annealing temperatures at 40 W of $P_{Sn\ DC}$, which can be roughly divided into three regions based on the carrier concentration, its polarity and resistivity, such as metallic, p-type semiconducting, and higher resistivity behavior. As the annealing temperature increases, the overall tendency of the carrier concentration decreases from about 10^{22} to 10^{16} cm^{-3} and that of the resistivity increases from about 10^{-4} to 10^{3} Ohm·cm (note that the metallic behavior was due to the formation of the percolation of the Sn clusters under 150 °C). In the case of Hall mobility, the value was proportionally increased with increasing the annealing temperature up to 180 °C, which showed the highest value, and the mobility inversely decreased thereafter. The average

values are plotted in Fig. 3.16(b), which are summarized in Table 3.6, respectively. In the polarity of carrier concentration, the metallic characteristic region is a minus, the p-type semiconductor region is a plus, and the higher resistivity region is difficult to define the polarity (note that the resistive behavior induced by the excessive oxidation). Since the sign of two cross hall coefficients of the films was abnormally inconsistent, it was marked with plus and minus simultaneously (±) on Table 3.6. In the metallic behavior region below 150 °C of the annealing temperature in Fig. 3.16(b), it can be seen that the metallic Sn phase is more dominant than the SnO phase because the sufficient amount of O atoms does not react with the Sn atoms due to insufficient thermal energy during the heat treatment process. It can also be seen that the mobility increases in inverse proportion to the decrease in the carrier concentration as the resistivity value is a similar level of approximately 10^{-4}.

In the p-type semiconducting behavior region at the annealing temperature ranging from 180 to 250 °C in Fig. 3.16(b), which is the same region in Fig. 3.16(a), the relatively increased thermal energy and more combined O and Sn atoms in the films resulted in a significant increase in the resistivity. However, as opposed to the Fig. 3.16(a), it can be seen that the Hall mobility was significantly decreased as the hole carrier concentration decreases, which showed the proportional relationship in Fig. 3.16(b). From these results, as shown in Fig. 3.16, the relationships between the Hall mobility

and hole carrier concentration at 0 W and 40 W of $P_{Sn\ DC}$ samples in the annealing temperature ranges from 180 to 250 °C are coincident with the tendency as confirmed the Hall measurement result in the region (1) in Fig. 3.15(a).

As mentioned above, the reason why the Hall mobility can be increased steadily with increasing the $P_{Sn\ DC}$ deduced the increase in hopping conduction effect. It may be originated from the partially formed disordered semiconductor structures as close to the Sn-rich SnO film. In other words, this film contains a high density of traps near the VB edge, making the film rather disordered p-type SnO semiconductor induced by the compressive stress property and the irregular protrusions as explained for the schematic diagram in Fig. 3.15(b). In addition, the thermal energy during the heat treatment process would be not enough to completely form the crystalline SnO structures, even though the amount Sn atoms is excessively increased. From these results, it can be considered that the characteristics and microstructure of the film were changed from 10 W of Sn DC power at which the co-sputtering began with increasing the amount of Sn and the characteristics and microstructure of the Sn DC power 0 and 40 W films were different. Moreover, It can be considered that the crystallinity of the SnO formed at 40 W of Sn DC power sample compared to the 0 W sample may be relatively poor due to the increase in the thickness of the thin film deposited from 30 to 100 nm for the hole measurement sample.

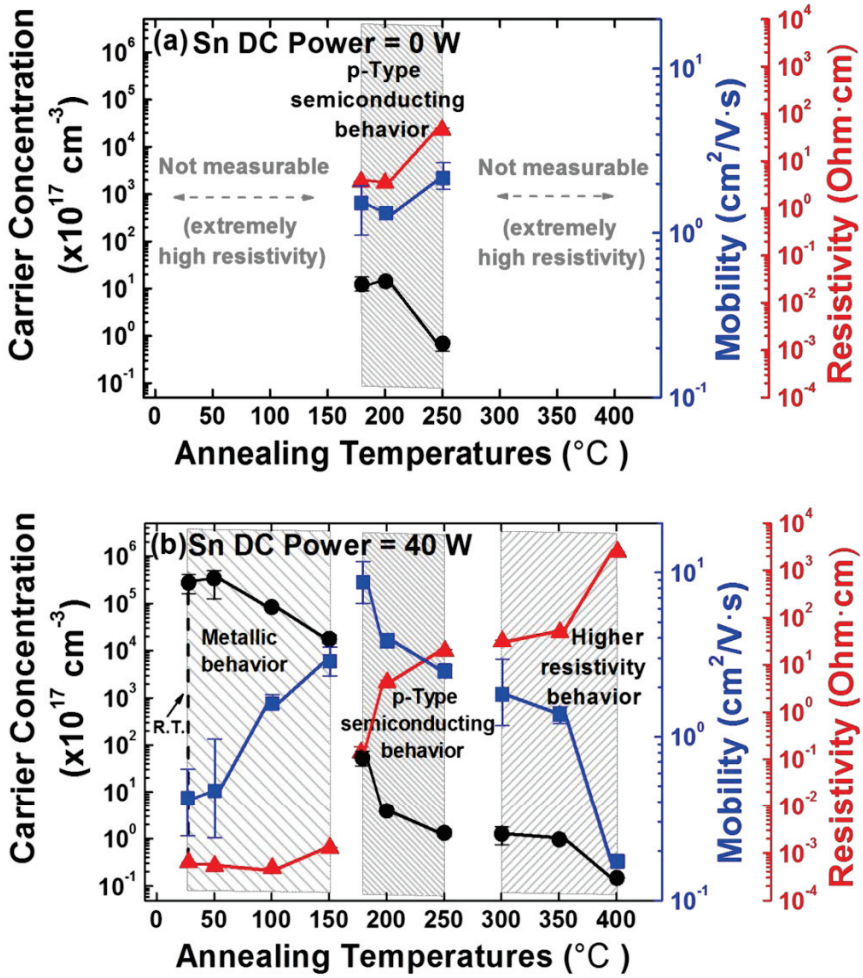

Figure 3.16. The plot of carrier transport data of the 100 nm-thick annealed films in the annealed temperatures ranging from RT to 400 °C at the $P_{Sn\,DC}$ of (a) 0 W and (b) 40 W with the fixed $P_{SnO\,RF}$ at 80 W.

Table 3.5 Carrier concentration, Hall mobility, resistivity as extracted from Hall effect measurements at the $P_{Sn\ DC}$ of 0 W with the fixed $P_{SnO\ RF}$ at 80 W dependence on the annealed temperatures ranging from RT to 400 ˚C. (Note that the reported values are the average of 5-10 valid results which obtained from the Hall measurements of several tens of times performed on the given sample of every condition).

Sn DC 0 W SnO RF 80 W	**Not measurable (extremely high resistivity)**				**p-Type semiconducting behavior**			**Not measurable (extremely high resistivity)**		
Annealed temp. [℃]	**27 (=RT)**	**50**	**100**	**150**	**180**	**200**	**250**	**300**	**350**	**400**
Mobility [cm^2/Vs]	-	-	-	-	**1.5**	**1.3**	**2.1**	-	-	-
Carrier conc. [cm^{-3}]	-	-	-	-	**1.2×10^{18}**	**1.4×10^{18}**	**6.7×10^{16}**	-	-	-
Resistivity [Ohm·cm]	**6.9×10^{6}**	**4.3×10^{6}**	**6.9×10^{6}**	**5.6×10^{6}**	**3.7**	**3.4**	**4.5×10**	**4.2×10^{5}**	**5.6×10^{5}**	**3.742×10^{6}**

Table 3.6 Carrier concentration, Hall mobility, resistivity as extracted from Hall effect measurements at the $P_{Sn\ DC}$ of 40 W with the fixed $P_{SnO\ RF}$ at 80 W dependence on the annealed temperatures ranging from RT to 400 ˚C. (Note that the reported values are the average of 5-10 valid results which obtained from the Hall measurements of several tens of times performed on the given sample of every condition).

Sn DC 40 W SnO RF 80 W	Metallic behavior				p-Type semiconducting behavior			Higher resistivity behavior (Unknown polarity)		
Annealed temp. [℃]	27 (=RT)	50	100	150	180	200	250	300	350	400
Mobility [cm^2/Vs]	0.4	0.5	1.6	2.9	8.8	3.9	2.5	1.8	1.4	0.2
Carrier conc. [cm^{-3}]	-2.8×10^{22}	-3.3×10^{22}	-8.2×10^{21}	-1.7×10^{21}	5.4×10^{18}	3.8×10^{17}	1.3×10^{17}	1.2×10^{17}	9.3×10^{16}	1.4×10^{16}
Resistivity [Ohm·cm]	6.1×10^{-4}	5.4×10^{-4}	4.8×10^{-4}	1.3×10^{-3}	1.3×10^{-1}	4.3	1.9×10	3.2×10	4.9×10	2.5×10^{3}

To estimate the possible correlation between the disparate electrical behaviors of the two types of films with their stress, the stress evolution of the two films as a function of annealing temperature was estimated. In this case, thicker 100 nm-thick films were sputtered under the 0 W and 40 W $P_{Sn\ DC}$ conditions on 100 μm-thick Si wafer to achieve even more accurate results and see thickness effects. The results are summarized in Fig. 3.17 for the films after the annealing at temperatures ranging from 180 to 250 ^{o}C for 25 min in an air atmosphere. Apart from the results in Fig. 3.12, all the films are under the tensile stress condition, suggesting that the thicker films were more effectively influenced by the porous microstructure effect (0 W of $P_{Sn\ DC}$ condition), i.e., the open region between the crystallized grains attracts the grains to each other (zipping stress) [73-75]. However, even under this circumstance, the film with 40 W of $P_{Sn\ DC}$ condition has lower tensile stress, which must be due to the compensation effect by the possible compressive stress effect induced by the oxidation of excess Sn during the heat treatment. This means that the SnO grain itself could be under the influence of more compressive stress in this film, which may induce higher disorder or defects within the semiconducting SnO region. These effects, in turn, induce more disordered structure compared with the other film, and trap-mediated hopping conduction behavior dominates the overall electrical conduction property.

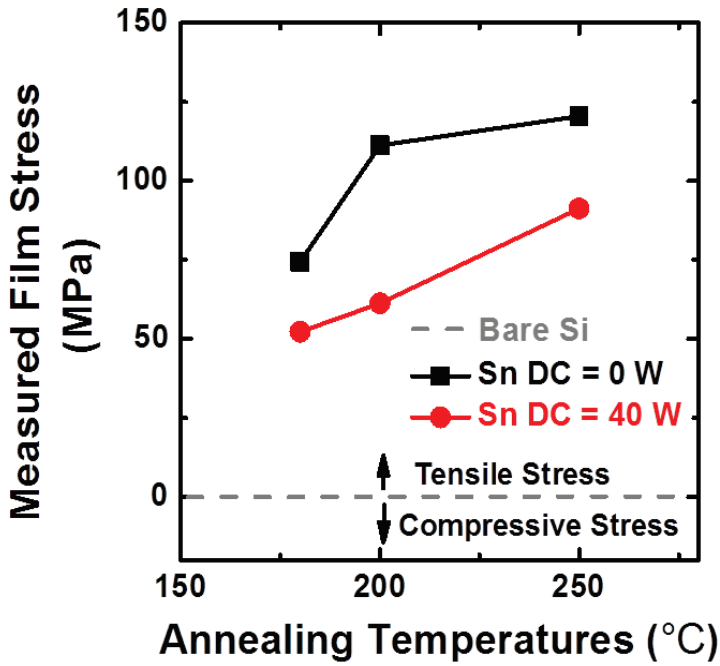

Figure 3.17. Measured film stress of 100 nm-thick films in the annealing temperatures ranging from 180 to 250 °C at the $P_{Sn\ DC}$ of 0 W and 40 W with the fixed $P_{SnO\ RF}$ at 80 W.

The relationship between the carrier concentration and the Hall mobility at the $P_{Sn\ DC}$ 0 W and 40 W samples was different according to the annealing temperature as well as the $P_{Sn\ DC}$ as shown in Fig. 3.15(a) and Fig. 3.16. To further confirm if the hypothesis of the difference in hole conduction mechanism assumed above is correct, this time, we measured the Hall at the $P_{Sn\ DC}$ of 0 W and 40 W for two samples according to the measured temperature. Figures 3.18(a) and (b) show the results of the Hall test from the two samples in Fig. 3.15(a) after the heat treatment at 180 ^{o}C, when the test was performed at temperatures from room temperature to 300 ^{o}C and these results are summarized in Table 3.7 and 3.8, respectively. The measurement was performed under the air ambient with increasing the Hall measurement temperature, and the entire test sequence requires more than 4 hours per sample. Therefore, the risk of oxidizing the film cannot be disregarded, and the transition of both films into the n-type semiconductor at temperatures higher than 180 ^{o}C indeed indicates that the significant oxidation of the films has occurred during the Hall measurements. Therefore, the data in the high-temperature region should not be taken to have the significance regarding the purpose of this work. At lower temperature regions, the two films show consistent behaviors to the data shown above. For the film grown with the 0 W of $P_{Sn\ DC}$, the carrier concentration decreases with the increasing temperature, which is inconsistent with the usual band conducting semiconductor. Therefore, the oxidation of the film to

the SnO_2 phase (at least on the film surface) still plays a role to produce traps or to decrease carrier concentration, which is consistent with the absence of excessive Sn. The increasing Hall mobility, however, with the decreasing hole concentration clearly reveal that this is a typical band conduction semiconductor.

For the case of the film grown with the 40 W of $P_{Sn\ DC}$ shows an opposite trend in carrier concentration with the increasing Hall measurement temperature, i.e., it increases with the increasing temperature up to 180 ^{o}C. While the possible oxidation of the film into the undesired SnO_2 might be suppressed by the absorption of oxygen into the remaining Sn metallic phase, the thermal activation of the carriers from the deep trap state to shallower traps or even to the valence band induced the abrupt carrier concentration increase. This is accompanied by the slight increase in the Hall mobility up to 100 ^{o}C, which is consistent with the hopping conduction mechanism near the mobility edge. An interesting finding could be made in the measurement temperature range from 120 to 180 ^{o}C, where the Hall mobility decreases with increasing the hole carrier concentration, which is consistent with the band conduction behavior. This appears a reasonable consequence of the carrier excitation from the deep level to the valence band at such high-temperature region, i.e., when the carrier concentration reaches to a level ~5 x 10^{19} cm^{-3}, the shallow traps are fully saturated with the thermally excited carriers, and further generated carriers move into the valence band and

conduct electricity via the band conduction mechanism.

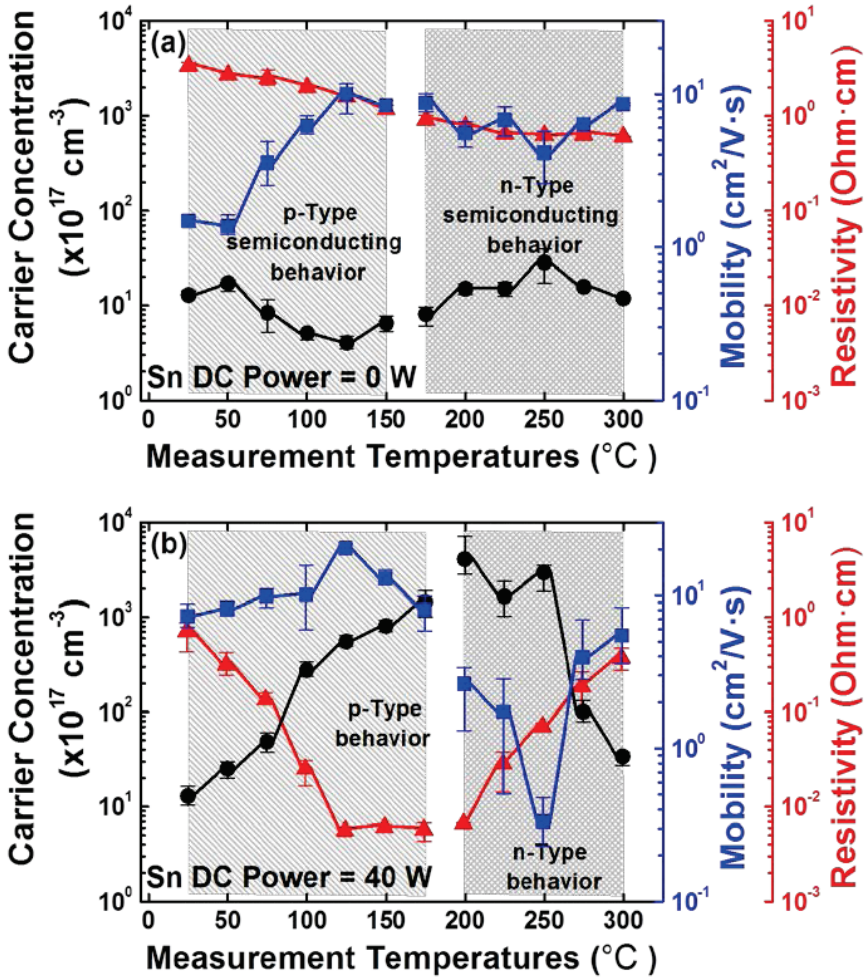

Figure 3.18. The plot of carrier transport data of the 100 nm-thick annealed films at 180 °C in the measurement temperatures ranging from RT to 300 °C at the $P_{Sn\ DC}$ of (a) 0 W and (b) 40 W with the fixed $P_{SnO\ RF}$ at 80 W.

Table 3.7 Carrier concentration, Hall mobility, resistivity as extracted from Hall effect measurements at the $P_{Sn\ DC}$ of 0 W with the fixed $P_{SnO\ RF}$ at 80 W dependence on the measurement temperatures ranging from RT to 300 °C. (Note that the reported values are the average of 5-10 valid results which obtained from the Hall measurements of several tens of times performed on the given sample of every condition).

Sn DC 0 W SnO RF 80 W	p-Type semiconducting behavior						n-Type semiconducting behavior					
Measurement temp. [℃]	27 (=RT)	50	75	100	125	150	175	200	225	250	275	300
Mobility [cm^2/Vs]	1.5	1.4	3.5	6.2	9.9	8.4	8.7	5.5	6.7	4.1	6.3	8.6
Carrier conc. [cm^{-3}]	1.3×10^{18}	1.7×10^{18}	8.3×10^{17}	5.1×10^{17}	4.0×10^{17}	6.5×10^{17}	-8.1×10^{17}	-1.5×10^{18}	-1.5×10^{18}	-2.8×10^{18}	-1.6×10^{18}	-1.2×10^{18}
Resistivity [Ohm·cm]	3.4	2.7	2.6	2.0	1.6	1.2	9×10^{-1}	8×10^{-1}	6×10^{-1}	6×10^{-1}	6×10^{-1}	6×10^{-1}

Table 3.8 Carrier concentration, Hall mobility, resistivity as extracted from Hall effect measurements at the $P_{Sn\ DC}$ of 40 W with the fixed $P_{SnO\ RF}$ at 80 W dependence on the measurement temperatures ranging from RT to 300 °C. (Note that the reported values are the average of 5-10 valid results which obtained from the Hall measurements of several tens of times performed on the given sample of every condition).

Sn DC 40 W SnO RF 80 W	p-Type behavior							n-Type behavior				
Measurement temp. [℃]	27 (=RT)	50	75	100	125	150	175	200	225	250	275	300
Mobility [cm^2/Vs]	7.3	8.2	9.9	10.1	20.3	12.9	8.1	2.6	1.7	0.3	3.9	5.5
Carrier conc. [cm^{-3}]	1.3×10^{18}	2.5×10^{18}	4.9×10^{18}	2.8×10^{19}	5.5×10^{19}	8.1×10^{19}	1.4×10^{20}	-4.1×10^{20}	-1.7×10^{20}	-3.0×10^{20}	-1.0×10^{19}	-3.4×10^{18}
Resistivity [Ohm·cm]	7.1×10^{-1}	3.1×10^{-1}	1.3×10^{-1}	2.5×10^{-2}	5.6×10^{-3}	6.1×10^{-3}	5.7×10^{-3}	6.7×10^{-3}	2.9×10^{-2}	7.0×10^{-2}	1.9×10^{-1}	3.7×10^{-1}

3.10. Co-sputtered SnO TFT analyses

From the Hall measurement results, we have decided that the optimum $P_{Sn\ DC}$ condition for application to SnO TFTs is at 40 W, and then the SnO TFT was fabricated by the conventional photolithography and its electrical characteristics were evaluated. Figure 3.19. The conceptual design of the co-sputtered SnO TFT is depicted in Fig. 3.19(a), whereas Fig. 3.19(b) and (c) show the output and transfer characteristics of the co-sputtered SnO TFT at 40 W of $P_{Sn\ DC}$, annealed at 160 ºC, 25 min. The output characteristic of SnO TFT in Fig. 3.19(b) shows that the negative drain current increases as the drain bias (V_{DS}) decrease from 0 to -25 V, and the negative gate bias (V_{GS}) was applied from 0 to -20 V at -5 V intervals. The negative drain current increases with increasing the negative V_{GS}, whereas the channel careers deplete with decreasing the negative V_{GS}, indicating the p-type behavior. The clear linear region can be observed, and the absence crowding at low V_{DS} region indicates an ohmic contact of Au with SnO. The transfer characteristic of SnO TFT in Fig. 3.19(c) measured with a low V_{DS} = -1 V as the V_{GS} ranging from -20 to 20 V, indicating that the on/off current ratio is ~3.3×10^3. The threshold voltage (V_{th}), calculated from the $I_{DS}^{1/2}$ vs V_{GS} plot, was -0.8 V. These data mean that the SnO TFT operates in the p-type enhancement mode since the holes are generated at negative V_{GS}. The slightly large off current, which is about 10^{-11} A level, are probably due to the

large hole carrier concentration, > 10^{18} cm^{-3}, as shown in Fig. 3.19(c). Note that the SnO channel thickness was reduced from 30 to 13 nm to improve the switching characteristic. The gate leakage current in the on the state was measured in the nA range, but this current level is slightly higher than the off current level, indicating poor insulating properties or damages of the dielectric layer by SnO deposition with high co-sputtering power. Optimization of the semiconductor-dielectric interface has been shown to play a crucial role in the improvement of the TFT device performance. Linear region field effect mobility (μ_{lin}) and subthreshold swing (SS) were evaluated with the conventional metal-oxide-semiconductor field effect transistor model described in Eq. (7) and (8) as follows [76]:

$$I_{DS} = \frac{W}{L}\mu_{lin}C_{ox}\left[\left(V_{GS} - V_{th}\right)V_{DS} - \frac{V_{DS}{}^{2}}{2}\right] \quad \text{for } V_{DS} < V_{GS} - V_{th} \quad (7)$$

$$SS = \frac{dV_{GS}}{d(\log I_{GS})} \approx \ln 10 \frac{kT}{q}\left[1 + \frac{qC_{dep}}{C_{ox}}\right] \quad (8)$$

where I_{DS} is the drain current, L and W is the device's channel length and width, which were fixed 5 and 20 μm, V_{GS} is the gate voltage, C_{ox} is the capacitance per unit area of the gate insulator and measured to be 60 $nFcm^{-2}$ and an extracted dielectric constant of about 14. The μ_{lin} is about 0.3 $cm^2/V{\cdot}s$, and the SS is -7.917 V/decade. The SnO TFT mobility is highly smaller than the Hall mobility at the same 40 W of $P_{Sn\ DC}$ condition, which indicates that the former is deteriorated by hole traps existing in the bandgap near the

VBM or at the interface of the gate insulator and the channel. However, it is still not clear why the large difference mobilities between TFT and Hall measurements happened. From this result, the unoptimized fabrication conditions should be considered further to improve the electrical performance of p-type SnO TFTs.

Consequently, it can be confirmed that the carefully controlled amount of metallic Sn atoms in SnO crystal as the Sn-rich SnO structure can enhance the Hall mobility and it was a coincidence with the previously published result [18]. This result can be explained to the hopping conduction mechanism due to the proportional relationship between the Hall mobility and the hole carrier concentration. The substantial oxidation of the incorporated Sn induced the in-plane compressive stress and the disordered SnO structures along with the formation of protrusions in the film, leading the improvement of Hall mobility with increasing the $P_{Sn\ DC}$. However, further increase of Sn atoms in the films leads to the formation of the percolation path of the metallic Sn clusters in the film, showing the metallic behavior of the films at 45 W $\leq P_{Sn\,DC} \leq$ 70 W in Fig. 3.15(a). It should be noted that it is essential to obtain the Sn-rich SnO phase as the p-type semiconducting behavior, until just before the change to the metallic behavior, for improvement of electrical characteristics of the films. The further research is needed to obtain the optimized TFT process conditions for reducing the difference between the Hall mobility and field effect mobility.

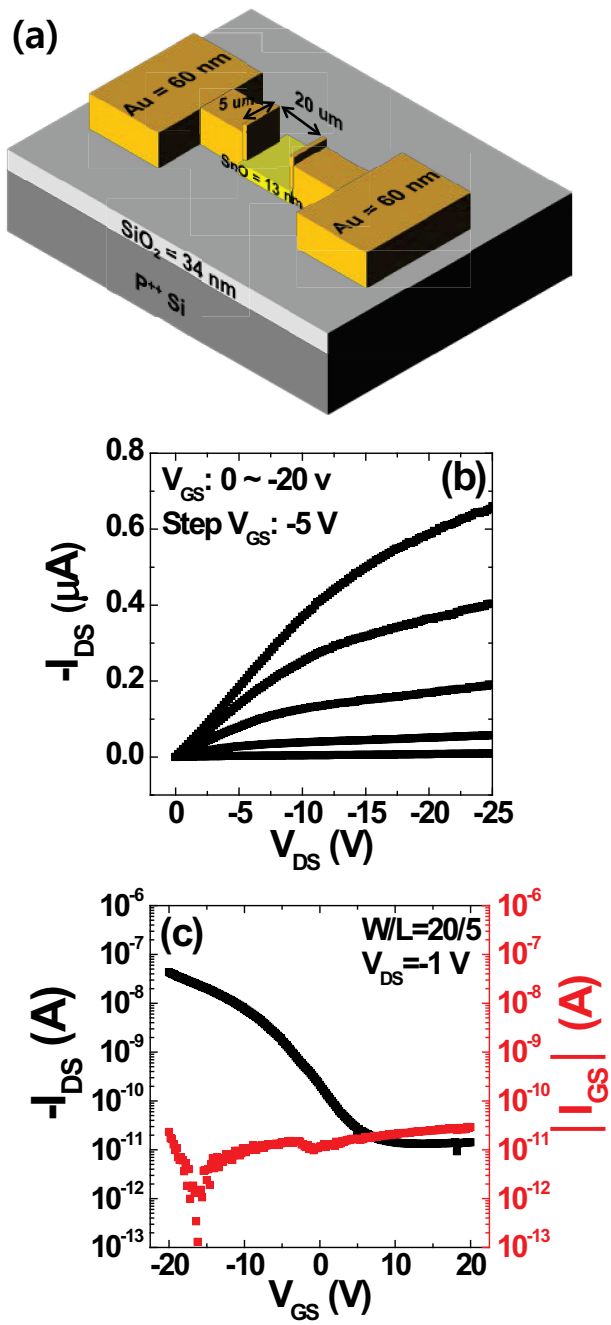

Figure 3.19. (a) The conceptual design of the co-sputtered SnO TFT, and its (b) output and (c) transfer characteristics at the $P_{Sn\ DC}$ of 40 W with the fixed $P_{SnO\ RF}$ at 80 W.

4. Conclusion

The SnO thin films were fabricated by the co-sputtering deposition technique with pure SnO and Sn targets followed by the low-temperature annealing at 180 °C in air, and the influence of $P_{Sn\ DC}$ on the various properties of the as-deposited and annealed films was systematically investigated. The GIXRD results showed that the as-deposited films showed a metallic Sn phase, and then it changed the p-type SnO phase after the heat treatment. The structural evolution of the annealed films showed the polycrystalline p-type SnO phase at 0 W $\leq P_{Sn\ DC} \leq$ 30 W, and both metallic Sn and p-type SnO phases as the Sn-rich SnO crystal structure at 40 W $\leq P_{Sn\ DC} \leq$ 70 W, which phase transition was described to the dependence on the presence of Sn amounts by co-sputtering. The FE-SEM images showed the discernible ellipsoidal grains along the *c*-axis direction at the as-deposited film and the irregular protrusions with the tiny and indistinct hemispherical swellings at the surface of the annealed film with increasing the $P_{Sn\ DC}$. The HRTEM images showed the metallic Sn phase at the as-deposited film, and the SnO phase in the protruded region and the metallic Sn phase in the uniform bulk region at the annealed film, which were coincident with the GIXRD results.

The lattice parameters *a* and *c* of the annealed films obtained from the GIXRD results that the unit cell volume (a^2c) was decreased as reaching to

the bulk SnO value under increasing the $P_{Sn\ DC}$. From the XRR and XRF results, both SnO density and Sn layer density of the films were increased with increasing the $P_{Sn\ DC}$ as closer to the Sn-rich conditions. The residual stress tendency of the as-deposited films shows that the tensile to compressive stress characteristics change as the $P_{Sn\ DC}$ increases. The residual stress of the annealed films indicated all compressive properties irrespective of $P_{Sn\ DC}$ and its tendency was a similar trend of the lattice parameter *c* with increasing the $P_{Sn\ DC}$. It means that the increase and decrease of the *c*-axis of SnO lattice have a direct effect on the physical state of the annealed film. Moreover, as the amount of Sn in SnO increased, the SnO structures became thermodynamically stable by the moderate compressive stress level. The atomic concentration of Sn relatively increased than that of O with increasing the $P_{Sn\ DC}$ in the XPS results, indicating the phases of changing from SnO to Sn-rich SnO, which is also consistent with the GIXRD results.

Moreover, the Hall measurement results of the annealed films can be roughly divided into two $P_{Sn\ DC}$ regions as follows: (1) 0 W $\leq P_{Sn\ DC} \leq$ 40 W, in which the films showed p-type semiconducting behavior dominated by the polycrystalline p-type SnO phase with well-controlled metallic Sn amounts. (2) 45 W $\leq P_{Sn\ DC} \leq$ 70 W, the films showed metallic behavior due to the formation of the percolation path of the metallic Sn clusters in the film with an influence of the excessively increasing Sn. The maximum Hall mobility of 8.8 $cm^2/V{\cdot}s$ obtained at 40 W of $P_{Sn\ DC}$. This result induced by the well-

controlled amount of metallic Sn in SnO structure, which was a coincidence with the previously published result. Despite the p-type disordered SnO semiconductor, it can be explained to the combination effect on the decreasing the lattice parameter *c* accompanied by increasing the film density as well as the trap-mediated hopping conduction, leading the increasing Hall mobility.

The Hall measurement results at various annealing and measurement temperatures for two samples with specific $P_{Sn\ DC}$ conditions at 0 W representing the SnO phase as a reference and 40 W representing the Sn-rich SnO phase showing the highest mobility indicated that the hole carrier conduction mechanisms of two samples could be different. Because it can be considered that the characteristics and microstructure of the film were changed from 10 W of Sn DC power at which the co-sputtering began and the characteristics and microstructure of the Sn DC power 0 and 40 W films were different. In other words, as the Sn increased, the ordered Sn-deficient SnO became the relatively disordered Sn-excessive SnO due to the changes of the film density, the in-plane compressive stress and the unit cell volume with increasing the formation of protrusions. All results supply the comprehensive investigation of the co-sputtered p-type SnO which would contribute to the exploration and development of the p-type SnO.

Bibliography

1. J. F. Wager, Transparent Electronics, *Science*, 2003, 300 (5623), 1245-1246

2. R. Martins, A. Nathan, R. Barros, L. Pereira, P. Barquinha, N. Correia, R. Costa, A. Ahnood, I. Ferreira, and E. Fortunato, Complementary Metal Oxide Semiconductor Technology With and On Paper, *Adv. Mater.*, 2011, 23 (39), 4491-4496

3. T. Kamiya and H. Hosono, Material Characteristics and Applications of Transparent Amorphous Oxide Semiconductors, *NPG Asia Mater.*, 2010, 2 (1) 15–22

4. E. Fortunato, P. Barquinha, A. Pimentel, A. Gonçalves, A. Marques, L. Pereira, and R. Martins, Fully Transparent ZnO Thin-Film Transistor Produced at Room Temperature, *Adv. Mater.*, 2005, 17 (5), 590-594

5. K. Nomura, H. Ohta, A. Takagi, T. Kamiya, M. Hirano, and H. Hosono, Room-Temperature Fabrication of Transparent Flexible Thin-Film Transistors Using Amorphous Oxide Semiconductors, *Nature*, 2004, 432, 488-492

6. E. Fortunato, P. Barquinha, and R. Martins, Oxide Semiconductor

Thin-Film Transistors: A Review of Recent Advances, *Adv. Mater.*, 2012, 24 (22), 2945-2986

7. Z. Wang, P. K. Nayak, J. A. Caraveo-Frescas, and H. N. Alshareef, Recent Developments in p-Type Oxide Semiconductor Materials and Devices, *Adv. Mater.*, 2016, 28 (20), 3831-3892

8. H. Luo, L. Y. Liang, Q. Liu, and H. T. Cao, Magnetron-Sputtered SnO Thin Films for p-Type and Ambipolar TFT Applications, *ECS J. Solid State Sci. Technol.*, 2014, 3 (9), Q3091-Q3094

9. S. Y. Kim, C. H. Ahn, J. H. Lee, Y. H. Kwon, S. Hwang, J. Y. Lee, and H. K. Cho, p-Channel Oxide Thin Film Transistors Using Solution-Processed Copper Oxide, *ACS Appl. Mater. Interfaces*, 2013, 5 (7), 2417-2421

10. P. Pattanasattayavong, S. Thomas, G. Adamopoulos, M. A. McLachlan, and T. D. Anthopoulos, p-Channel Thin-Film Transistors Based on Spray-Coated Cu_2O Films, *Appl. Phys. Lett.*, 2013, 102 (16), 163505 (1-4)

11. J. A. Caraveo-Frescas and H. N. Alshareef, Transparent p-Type SnO Nanowires with Unprecedented Hole Mobility among Oxide Semiconductors, *Appl. Phys. Lett.*, 2013, 103 (22), 222103 (1-5)

12. P. K. Nayak, J. A. Caraveo-Frescas, Z. Wang, M. N. Hedhili, Q. X.

Wang, and H. N. Alshareef, Thin Film Complementary Metal Oxide Semiconductor (CMOS) Device Using a Single-Step Deposition of the Channel Layer, *Sci. Rep.*, 2014, 4 (4672), 1-7

13. F. Shan, A. Liu, H. Zhu, W. Kong, J. Liu, B. Shin, E. Fortunato, R. Martinse and G. Liu, High-Mobility p-Type NiO_x Thin-Film Transistors Processed at Low Temperatures with Al_2O_3 High-*k* Dielectric, *J. Mater. Chem. C*, 2016, 4 (40), 9438-9444

14. J. Jiang, X. Wang, Q. Zhang, J. Li, and X. X. Zhang, Thermal Oxidation of Ni Films for p-Type Thin-Film Transistors, *Phys. Chem. Chem. Phys.*, 2013,15 (18), 6875-6878

15. Y. Ogo, H. Hiramatsu, K. Nomura, H. Yanagi, T. Kamiya, M. Hirano, and H. Hosono, p-Channel Thin-Film Transistor Using p-Type Oxide Semiconductor, SnO, *Appl. Phys. Lett.*, 2008, 93 (3), 032113 (1-3)

16. Y. Ogo, H. Hiramatsu, K. Nomura, H. Yanagi, T. Kamiya, M. Kimura, M. Hirano, and H. Hosono, Tin Monoxide as an s-Orbital-Based p-Type Oxide Semiconductor: Electronic Structures and TFT Application, *Phys. Status Solidi A*, 2009, 206 (9), 2187–2191

17. H. Luo, L. Y. Liang, H. T. Cao, Z. M. Liu, and F. Zhuge, Structural, Chemical, Optical, and Electrical Evolution of SnO_x Films

Deposited by Reactive RF Magnetron Sputtering, *ACS Appl. Mater. Interfaces*, 2012, 4 (10), 5673-5677

18. J. A. Caraveo-Frescas, P. K. Nayak, H. A. Al-Jawhari, D. B. Granato, U. Schwingenschlögl, and H. N. Alshareef, Record Mobility in Transparent p‑Type Tin Monoxide Films and Devices by Phase Engineering, *ACS Nano*, 2013, 7 (6), 5160–5167

19. M. Becker, A. Polity, P. J. Klar, and B. K. Meyer, Synthesis of Tin Oxides SnO_{2-x} in the Entire Composition Range (x = 0 to 1) by Ion-Beam Sputter-Deposition, *Phys. Status Solidi RRL*, 2015, 9 (5), 326-330

20. H. Yabuta, N. Kaji, R. Hayashi, H. Kumomi, K. Nomura, T. Kamiya, M. Hirano, and H. Hosono, Sputtering Formation of p-Type SnO Thin-Film Transistors on Glass Toward Oxide Complimentary Circuits, *Appl. Phys. Lett.*, 2010, 97 (7), 072111 (1-3)

21. K. J. Saji, K. Tian, M. Snure, and A. Tiwari, 2D Tin Monoxide—An Unexplored p-Type van der Waals Semiconductor: Material Characteristics and Field Effect Transistors, *Adv. Electron. Mater.*, 2016, 2 (4), 1500453 (1-9)

22. H.-N. Lee, H.-J. Kim, and C.-K. Kim, p-Channel Tin Monoxide

Thin Film Transistor Fabricated by Vacuum Thermal Evaporation, *Jpn. J. Appl. Phys.*, 2010, 49 (2), 020202 (1-3)

23. P.-C. Hsu, C.-J. Hsu, C.-H. Chang, S.-P. Tsai, W.-C. Chen, H.-H. Hsieh, and C.-C. Wu, Sputtering Deposition of p-Type SnO Films with SnO_2 Target in Hydrogen-Containing Atmosphere, *ACS Appl. Mater. Interfaces*, 2014, 6 (16), 13724-13729

24. Q. Liu, L. Liang, H. Cao, H. Luo, H. Zhang, J. Li, X. Li and F. Deng, Tunable Crystallographic Grain Orientation and Raman Fingerprints of Polycrystalline SnO Thin Films, *J. Mater. Chem. C*, 2015, 3 (5), 1077-1081

25. K. Okamura, B. Nasr, R. A. Brand and H. Hahn, Solution-Processed Oxide Semiconductor SnO in p-Channel Thin-Film Transistors, *J. Mater. Chem.*, 2012, 22 (11), 4607-4610

26. J. H. Han, Y. J. Chung, B. K. Park, S. K. Kim, H.-S. Kim, C. G. Kim, and T.-M. Chung, Growth of p‑Type Tin(II) Monoxide Thin Films by Atomic Layer Deposition from Bis(1-dimethylamino-2-methyl-2propoxy)Tin and H_2O, *Chem. Mater.*, 2014, 26 (21), 6088-6091

27. T. Toyama, Y. Seo, T. Konishi, H. Okamoto, and Y. Tsutsumi, Physical Properties of p-Type Tin Monoxide Films Deposited at

Low Temperature by Radio Frequency Magnetron Sputtering, *Appl. Phys. Express*, 2011, 4 (7), 071101 (1-3)

28. Y.-H. Jiang, I-C. Chiu, P.-K. Kao, J.-C. He, Y.-H. Wu, Y.-J. Yang, C.-C. Hsu, I-C. Cheng, and J.-Z. Chen, Influence of Rapid-Thermal-Annealing Temperature on Properties of RF-Sputtered SnO_x Thin Films, *Appl. Surf. Sci.*, 2015, 327, 358-363

29. DisplayBank, 2011

30. E. Fortunato, P. Barquinha, and R. Martins, Oxide Semiconductor Thin-Film Transistors: A Review of Recent Advances, *Adv. Mater.*, 2012, 24 (22), 2945-2986

31. T. Kamiya, K. Nomura, and H. Hosono, Present Status of Amorphous In-Ga-Zn-O Thin-Film Transistors, *Sci. Technol. Adv. Mater.*, 2010, 11 (4), 044305 (1-23)

32. H. Hosono, Y. Ogo, H. Yanagi, and T. Kamiya, Bipolar Conduction in SnO Thin Films, *Electrochem. Solid-State Lett.*, 2011, 14 (1), H13-H16

33. E. Fortunato, V. Figueiredo, P. Barquinha, E. Elamurugu, R. Barros, G. Goncalves, S. H. K. Park, C. S. Hwang, and R. Martins, Thin-Film Transistors based on p-Type Cu_2O Thin Films Produced at Room Temperature, *Appl. Phys. Lett.*, 2010, 96 (19), 192102 (1-3)

34. U. K. Barik, S. Srinivasan, C. L. Nagendra, and A. Subrahmanyam, Electrical and Optical Properties of Reactive DC Magnetron Sputtered Silver Oxide Thin Films: Role of Oxygen, *Thin Solid Films*, 2003, 429 (1-2), 129-134

35. H. Mizoguchi, H. Kawazoe, and H. Hosono, Enhancement of Electrical Conductivity of Polycrystalline β-PbO by Exposure to Ozone Gas at Room Temperature, *Chem. Mater.*, 1996, 8 (12), 2769-2773

36. H. Hiramatsu, H. Yanagi, T. Kamiya, K. Ueda, M. Hirano, and H. Hosono, Crystal Structures, Optoelectronic Properties, and Electronic Structures of Layered Oxychalcogenides *M*CuO*Ch* (*M* = Bi, La; *Ch* = S, Se, Te): Effects of Electronic Configurations of M^{3+} Ions, *Chem. Mater.*, 2008, 20 (1), 326–334

37. D. B. Granato, J. A. Caraveo-Frescas, H. N. Alshareef, and U. Schwingenschlögl, Enhancement of p-Type Mobility in Tin Monoxide by Native Defects, *Appl. Phys. Lett.*, 2013, 102 (21), 212105 (1-4)

38. A. Togo, F. Oba, I. Tanaka, and K. Tatsumi, First-Principles Calculations of Native Defects in Tin Monoxide, *Phys. Rev. B*, 2006, 74 (19), 195128 (1-8)

39. E. Fortunato, R. Barros, P. Barquinha, V. Figueiredo, S.-H. K. Park, C.-S. Hwang, and R. Martins, Transparent p-Type SnOx Thin Film Transistors Produced by Reactive RF Magnetron Sputtering Followed by Low Temperature Annealing, Appl. Phys. Lett., 2010, 97 (5), 052105 (1-3)

40. M. Batzill, and U. Diebold, The Surface and Materials Science of Tin Oxide, *Prog. Surf. Sci.*, 2005, 79 (2-4), 47-154

41. H. Giefers, F. Porsch, G. Wortmann, Kinetics of the Disproportionation of SnO, *Solid State Ion.*, 2005, 176 (1-2), 199-207

42. W. H. Doh, W. Jeong, H. Lee, J. Park, and J. Y. Park, Work Function Engineering of SnO Single Crystal Microplates with Thermal Annealing, *Nanotechnology*, 2016, 27 (33), 335603 (1-7)

43. J. Zhang, X. Kong, J. Yang, Y. Li, J. Wilson, J. Liu, Q. Xin, Q. Wang, and A. Song, Analysis of Carrier Transport and Band Tail States in p-Type Tin Monoxide Thin-Film Transistors by Temperature Dependent Characteristics, *Appl. Phys. Lett.*, 2016, 108 (26), 263503 (1-4)

44. L. Y. Liang, Z. M. Liu, H. T. Cao, Z. Yu, Y. Y. Shi, A. H. Chen, H. Z. Zhang, Y. Q. Fang, and X. L. Sun, Phase and Optical

Characterizations of Annealed SnO Thin Films and Their p-Type TFT Application, *J. Electrochem. Soc.*, 2010, 157 (6), H598-H602

45. J. Geurts, S. Rau, W. Richter, and F. J. Schmitte, SnO Films and Their Oxidation to SnO2: Raman Scattering, IR Reflectivity and X-Ray Diffraction Studies, *Thin Solid Films*, 1984, 121 (3), 217-225

46. M. S. Moreno, R. C. Mercader, and A. G. Bibiloni, Study of Intermediate Oxides in SnO Thermal Decomposition, *J. Phys.: Condens. Mater.*, 1992, 4 (2), 351

47. Y. Pei, W. Liu, J. Shi, Z. Chen, and G. Wang, Fabrication and Characterization of p-Type SnO Thin Film with High c-Axis Preferred Orientation, *J. Electron. Mater.*, 2016, 45 (11), 5967-5973

48. J. P. Allen, D. O. Scanlon, S. C. Parker, and G. W. Watson, Tin Monoxide: Structural Prediction from First Principles Calculations with van der Waals Corrections, *J. Phys. Chem. C*, 2011, 115 (40), 19916-19924

49. M. S. Moreno, G. Punte, G. Rigotti, R. C. Mercader, A. D. Weisz, and M. A. Blesa, Kinetic Study of the Disproportionation of Tin Monoxide, *Solid State Ion.*, 2001, 144 (1-2), 81-86

50. A. G. Sabnis, Two-Step Process for Thin Films of Tin Dioxide, *J. Vac. Sci. Technol.*, 1978, 15 (4), 1565-1567

51. M. Kanayama, T. Oku, T. Akiyama, Y. Kanamori, S. Seo, J. Takami, Y. Ohnishi, Y. Ohtani, and M. Murozono, Microstructure Analysis and Properties of Anti-Reflection Thin Films for Spherical Silicon Solar Cells, *Energy and Power Engineering*, 2013, 5 (2A), 18-22

52. A. Guinier, X-Ray Diffraction in Crystals, Imperfect Crystals and Amorphous Bodies, 1994, p. 83, (Dover, New York)

53. J. Ni, X. Zhao, and J. Zhao, p-Type Transparent Conducting SnO_2:Zn Film Derived from Thermal Diffusion of Zn/SnO_2/Zn Multilayer Thin Films, *Surf. Coat. Tech.*, 2012, 206 (21), 4356-4361

54. T. Toyama, Y. Seo, T. Konish, H. Okamoto, R. Morimoto, Y. Nishikawa, and Y. Tsutsumi, Optical Absorption Spectra of p-Type Tin Monoxide thin Films around Their Indirect Fundamental Gaps Determined Using Photothermal Deflection Spectroscopy, *Thin Solid Films*, 2014, 555 (31), 148-152

55. W. J. Moore, and L. Pauling, The Crystal Structures of the Tetragonal Monoxides of Lead, Tin, Palladium, and Platinum, *J. Am. Chem. Soc.*, 1941, 63 (5), 1392-1394

56. J. Pannetier, and G. Denes, Tin(II) oxide: structure refinement and thermal expansion, *Acta Crystallogr. B Struct. Crystallogr. Cryst.*

Chem., 1980, 36 (11), 2763-2765

57. K. Govaerts, R. Saniz, B. Partoens, and D. Lamoen, van der Waals Bonding and the Quasiparticle Band Structure of SnO from First Principles, *Phys. Rev. B*, 2013, 87 (23), 235210 (1-7)

58. E. L. P. Blancá, A. Svane, N. E. Christensen, C. O. Rodríguez and O. M. Cappannini, and M. S. Moreno, Calculated Static and Dynamic Properties of β-Sn and Sn-O Compounds, *Phys. Rev. B*, 1993, 48 (21), 15712-15718

59. M.-J. Choi, C. J. Cho, K.-C. Kim, J. J. Pyeon, H.-H. Park, H.-S. Kim, J. H. Han, C. G. Kim, T.-M. Chung, T. J. Park, B. Kwon, D. S. Jeong, S.-H. Baek, C.-Y. Kang, J.-S. Kim, and S. K. Kim, SnO_2 Thin Films Grown by Atomic Layer Deposition Using a Novel Sn Precursor, *Appl. Surf. Sci.*, 2014, 320, 188-194

60. J. P. Allen, D. O. Scanlon, L. F. J. Piper and G. W. Watson, Understanding the Defect Chemistry of Tin Monoxide, *J. Mater. Chem. C*, 2013, 1 (48), 8194-8208

61. K. Nomura, T. Kamiya, and H. Hosono, Ambipolar Oxide Thin-Film Transistor, *Adv. Mater.*, 2011, 23 (30), 3431-3434

62. L. Liang, Y. Sun, F. Lei, S. Gao and Y. Xie, Free-Floating Ultrathin Tin Monoxide Sheets for Solar-Driven Photoelectrochemical Water

Splitting, *J. Mater. Chem. A*, 2014, 2 (27), 10647-10653

63. H. Giefers, S. Koval, G. Wortmann, W. Sturhahn, E. E. Alp, and M. Y. Hu, Phonon Density of States of Sn in Textured SnO under High Pressure: Comparison of Nuclear Inelastic X-ray Scattering Spectra to a Shell Model, *Phys. Rev. B*, 2006, 74 (9), 094303 (1-12)

64. D. Guan, A. R. Bruccoleri, R. K. Heilmann and M. L. Schattenburg, Stress Control of Plasma Enhanced Chemical Vapor Deposited Silicon Oxide Film from Tetraethoxysilane, *J. Micromech. Microeng.*, 2014, 24 (2) 027001 (1-6)

65. M. J. Wahila, K. T. Butler, Z. W. Lebens-Higgins, C. H. Hendon, A. S. Nandur, R. E. Treharne, N. F. Quackenbush, S. Sallis, K. Mason, H. Paik, D. G. Schlom, J. C. Woicik, J. Guo, D. A. Arena, B. E. White Jr., G. W. Watson, A. Walsh, and L. F. J. Piper, Lone-Pair Stabilization in Transparent Amorphous Tin Oxides: A Potential Route to p‑Type Conduction Pathways, *Chem. Mater.*, 2016, 28 (13), 4706-4713

66. S. J. Han, S. Kim, J. Ahn, J. K. Jeong, H. Yang, and H. J. Kim, Composition-Dependent Structural and Electrical Properties of p-Type SnOx Thin Films Prepared by Reactive DC Magnetron Sputtering: Effects of Oxygen Pressure and Heat Treatment, *RSC Adv.*, 2016, 6 (75), 71757-71766

67. S. Hwang, Y. Y. Kim, J. H. Lee, D. K. Seo, J. Y. Lee, and H. K. Cho, Irregular Electrical Conduction Types in Tin Oxide Thin Films Induced by Nanoscale Phase Separation, *J. Am. Ceram. Soc.*, 2012, 95 (1), 324–327

68. J. A. Caraveo-Frescas, M. A. Khan, and H. N. Alshareef, Polymer Ferroelectric Field-Effect Memory Device with SnO Channel Layer Exhibits Record Hole Mobility, *Sci. Rep.*, 2014, 4 (5243), 1-7

69. S. L. Moffitt, Q. Zhu, Q. Ma, A. F. Falduto, D. B. Buchholz, R. P. H. Chang, T. O. Mason, J. E. Medvedeva, T. J. Marks, and M. J. Bedzyk, Probing the Unique Role of Gallium in Amorphous Oxide Semiconductors through Structure–Property Relationships. *Adv. Electron. Mater.* 2017, 3 (10), 1700189

70. N.-E. Sung, H.-K. Lee, K. H. Chae, J. P. Singh, and I.-J. Lee, Correlation of Oxygen Vacancies to Various Properties of Amorphous Zinc Tin Oxide Films, *Appl. Phys. Lett.* 2017, 122 (8), 085304

71. V. Ha, F. Ricci, G.-M. Rignanese, and G. Hautier, Structural Design Principles for Low Hole Effective Mass s-Orbital-Based p-Type Oxides, *J. Mater. Chem. C*, 2017, 5 (23), 5772-5779

72. R.A. Serway, Principles of Physics (2nd ed.). 1998, 602, (Fort

Worth, Texas; London: Saunders College Pub.)

73. W. D. Nix, and B. M. Clemens, Crystallite coalescence: A Mechanism for Intrinsic Tensile Stresses in Thin Films, *J. Mater. Res.,* 1999, 14 (8), 3467-3473

74. D. J. Quinn, B. Wardle, and S. M. Spearing, Residual Stress and Microstructure of As-deposited and Annealed, Sputtered Yttria-Stabilized Zirconia Thin Films, *J. Mater. Res.,* 2008, 23 (3), 609-618

75. M. S. Carroll, J. C. Verley, J. J. Sheng, and J. Banks, Roughening Transition in Nanoporous Hydrogenated Amorphous Germanium: Roughness Correlation to Film Stress, *J. Appl. Phys.,* 2007, 101 (6), 063540

76. J. F. Wager, Transfer-Curve Assessment of Oxide Thin-Film Transistors, *J. Soc. Inf. Disp.*, 2010, 18 (10), 749-752

Abstract (in Korean)

본 논문은 SnO 산화물 타겟과 Sn 금속 타겟을 동시에 스퍼터링하는 공정 (co-sputtering technique)을 통해 제조된 SnO 박막의 특성을 연구한 내용이다. p형 SnO 특성은 공기 중에서 180도의 열처리 온도를 가하여 얻어낼 수 있었으며, 증착된 박막의 특성은 열처리 전과 후의 특성 비교를 통해 보다 체계적으로 설명하였다. 본 실험의 변수는 금속 Sn 타겟에 인가되는 직류 (DC) 전압의 세기로서, SnO 산화물 타겟에 인가하는 라디오 주파수 (RF) 전압은 고정한 상태에서 박막을 제조하였다. 먼저 GIXRD 분석 결과를 통해 열처리 전의 증착된 박막은 금속성 Sn 상태를 보여 주었으나, 열처리 이후로는 인가되는 Sn DC 전압의 세기에 따라서 SnO와 더불어, SnO와 금속성 Sn이 모두 공존하는 특성을 나타내었다. 열처리 후의 박막 특성은 변수에 관계없이 모두 p형 특성을 보여주었으며, SnO 인가 전압 80 W 대비 Sn의 인가하는 전압이 40 W되는 지점에서부터 위와 같이 박막의 상 전이 (phase transition)가 발생하였다.

초고해상도 FE-SEM 사진의 결과를 살펴보면, 열처리 후 박막의 경우 표면에서의 비규칙적인 돌출부가 발생하였음을 알 수 있었다. 이는 초고해상도 TEM 분석을 통해, 돌출부는 SnO, 돌출부 아래 영역은 금속 Sn 특성이 나타남을 확인하였다. GIXRD 분석을 통해 유도해낸 SnO의 격자 상수 값 *a*와 *c*를 살펴보면, SnO 단위 격자 부피가 Sn 인가 전압 증가에 반비례하는 결과를 보여 주었다. 또한, 열처리한 박막의 밀도와 금속 Sn의 면 밀도를 측정해본 결과, 역시 Sn 인가 전압 증가에 비례하는 결과를 보여주었다. 열처리 전 박막의 잔류 응력 (residual stress)를 측정한 결과 모두 압축 응력 특성 (compressive stress)을 나타내고 있으며, 이에 대한 경향성은 SnO의 격자 상수 c축의 경향성과 일치함을 보였다. XPS 분석을 통

해 확인해 본 결과, Sn 인가 전압이 증가함에 따라 비례하여 증가하는 금속 Sn 성분이 나타남을 확인할 수 있었으며, 이는 p형 특성은 유지하되, SnO 박막에서 금속 Sn 성분이 과다한 SnO 박막 특성으로 상 변이 현상을 확인할 수 있었다.

본 열처리 박막의 홀측정을 진행한 결과, GIXRD 결과와 마찬가지로 Sn DC 40 W가 되는 지점을 기준으로 반도체 특성과 금속 특성으로 나뉘어 짐을 확인할 수 있었다. 반도체 특성을 나타내는 영역에서 살펴볼 경우, Sn의 양이 증가할수록, 열처리된 박막의 홀 이동도 값이 증가하는 특성을 보였다. 본 실험에 기준 조건인 Sn DC 0 W와 더불어, 가장 홀 이동도가 높고 상대적으로 Sn이 과다한 SnO 특성을 보여주는 Sn DC 40 W, 이 두 박막에 대해 열처리 온도에 따른 홀측정을 진행한 결과, 정공 이동도와 농도의 관계를 통해, 두 박막의 정공 전도 현상의 원리가 다를 수 있음을 예상해 볼 수 있었다. 기존 p형 SnO 특성에 비해, 금속 Sn 원자량이 미세하게 조절되어 첨가된 SnO의 박막 특성이 보다 향상된 결과임을 확인해 보았을 때, p형 박막 트랜지스터 소자의 전기적 특성 향상 및 발전에 기여할 수 있을 것으로 예상된다.

주요어: p형 주석 산화물 (SnO), 금속성 Sn이 과다한 SnO, 동시 스퍼터링, SnO 격자 상수, 잔류 응력, 홀측정

학번: 2013-30765

이 승 준